Department of Chemistry

University College London

Theoretical and Experimental Investigations of Graphitic and Crystalline Carbon Nitrides

A thesis submitted for the degree of Doctor

of Philosophy by

Aisha Syeda Rahman

February 2014

Declaration

I, Miss Aisha Syeda Rahman, confirm that the work presented in this PhD thesis is my own. Where information has been derived from other sources, I confirm that this has clearly been indicated.

Aisha Syeda Rahman

Friday 14th February 2014

Abstract

Solid-state carbon nitride materials are useful in a number of areas in industry, ranging from heat retardation, photocatalysis, electrochemistry, as well as the potential to form a new super hard material to rival diamond. The flexible nature of the chemical bonding and environment of C and N atoms in a carbon nitride system gives rise to wide structural diversity, which present challenges in characterisation of the material. Theoretical modeling for such a versatile system is an essential part of scientific research.

Quantum mechanical computational methods are employed to study carbon nitride materials in dense sp^3 bonded and planar polymeric graphitic phases. The computer codes used for this study are CRYSTAL and CASTEP, both based on DFT. Synthesis of dense and graphitic carbon nitride materials, using ionothermal and thermal methods were also conducted towards part of this research. The results from each theoretically calculated investigation in this thesis are compared with experimental data, to guide the understanding of the experimental results for the system under study.

Experimentally synthesised and recovered carbon nitride material, with defective wurtzite structure and C_2N_3H stoichiometry, was investigated for its stability over a range of pressures. Three possible C_2N_3H phases arising from different proton arrangements were modeled to determine the most stable arrangement. A metastable C_2N_3H phase was detected experimentally; an *ab initio* structure

prediction method was employed, which identified a structure that complied with experimental observations.

CASTEP was tested and used to calculate NMR chemical shifts for ^{13}C and ^{15}N atoms for a number of carbon nitride materials. Predictions were focused on determining the atom connectivity and structural topology for thermal synthetic methods that yielded dense and graphitic carbon nitride solid-state materials. Calculated NMR chemical shifts were also employed in a collaborative study to guide the understanding of planetary tholins, formed in Titan's atmosphere.

Acknowledgements

I begin with heartfelt thanks to my principal supervisor, Professor Paul F McMillan, for a place in his research group and providing the opportunity to work on such an interesting project. The whole PhD experience and carbon nitride project would've certainly been lackluster had I been supervised by anyone else. A big thank you and recognition to my secondary supervisor, Dr Furio Corà, for his guidance and excellent discussions surrounding the theoretical aspects, and most of all his help with the revisions to complete the final product – his support made all the difference.

Thank you to Professor Chris Pickard who was a real inspiration to work with. I would like to also thank members of his research group for being available for the all-important discussions and for their advice, especially for hints and tips on using the AIRSS method. Drs Andrew Morris, Maria Baias and Miguel Martinez – the coffee mornings and discussions in the Physics Building will always be remembered as fond memories.

I would also like to thank Dr Abil Aliev for his excellent support and guidance on the NMR aspects of this thesis, and the opportunity to contribute to the Glycine NMR study. I learnt so much from working with Abil in such a short space of time; he was a valuable guide and always had good advice to impart at every meeting.

Professor Andrea Sella, was an excellent example of how to get things done in the lab. Another important collaboration, in the final months of the research, where I can safely say I learnt from a master of synthetic techniques.

A big mention to five very important people in the Department of Chemistry at UCL, whose help and support certainly made facilitating the research a lot easier. Thank you from the very depths of my heart to Dave Knapp, Joe Nolan, Crosby Medely, Jörg Saßmannshausen and Charles Willoughby, for always being so efficient and helpful.

I must also mention a massive acknowledgement to a number of my friends, who have all been an important part of this process, many of whom I met during the course of the PhD. So in no particular order, as you are all important to me in one way or another, Drs Luis Gomez-Hortiguela, Antonio Torrisi, Sara Balesaria, Vesna Middelkoop, Dominik Daeisenberger, Janne Hagen, Misbah Sarwar, Mark Michel, Alastair Smith, Phil Catton, Lorna Anguilano, Tiffany (Hsin-Yi Chen) and Stella Vallejos. Soon to be Drs Aminah Farah, , Eleni Androulaki, Charmian Dawson, and Lamya Al-Haj. Those friends whose companionship I appreciated over the years; Penny Grigoriou, Amandeep Sandhu, Monica Dolan, April Lloyd, Hadil al-Etabi, Katrin Klink, Geraldine Warrington and Janet Jones. You can all be sure that the distracted 'I'm focusing on my thesis' mode is over ☺

Leaving the most dear to my heart to the end; my wonderful sisters, Maria and Juwaria, have both provided their ears and many hours of patience while I've

discussed 'the' project, at length with each of them. The hours of laughing and joking together, at times of stress were a much-needed relief. My fantastic brother Samaan, who I'm fortunate and blessed to be related, he is a true inspiration and a real genius. I thank him for his excellent understanding at times when I needed it most. He was always there at just the right time, to always say the right thing and impart perfect advice. I hope, my dear family, that after the years of hearing about the carbon nitride project and all it entailed, you are proud.

This journey has been an excellent challenge. Would I do it all again? Yes. Without a doubt, I most definitely would.

Dedication

This thesis is dedicated to the most important and beloved people in my life, my parents.

My father, Syed Muhammed Abdur Rahman, for always having believed in my ability to do anything I set my mind to; his words of unyielding support echoed in my ears, throughout times of difficulty, and provided the motivation to continue. He truly was the best father and teacher I ever could have wished for.

My mother, Nashira Khatoon Rahman, has always been a wonderful role model to me, teaching me that determination and dedication are two important characteristics to succeed. She is the most amazing person I know and I am fortunate to call her my mother. Both my parents have been an important inspiration throughout my life, at every stage, and certainly during the years of the PhD research.

List of Publications

A. Belen Jorge, David James Martin, Mandeep T. S. Dhanoa, <u>Aisha S. Rahman</u>, Neel Makwana, Junwang Tang, Andrea Sella, Furio Corà, Steven Firth, Jawwad A. Darr, Paul F. McMillan, *H_2 and O_2 Evolution from Water Half-Splitting Reactions by Graphitic Carbon Nitride Materials*, Journal of Physical Chemistry C, **117**, 7178, (2013)

Sylvie Derenne, C Coelho, C Anquetil, Cyril Szopa, <u>Aisha S Rahman</u>, Paul F McMillan, Furio Corà, Chris J Pickard, Eric Quirico, C Bonhomme, *New insights in the structure and chemistry of Titan's tholins via 13C and 15N solid state nuclear magnetic resonance spectroscopy,* Icarus, **221**, 844, (2012)

Abil E Aliev, Sam E Mann, <u>Aisha S Rahman</u>, Paul F McMillan, Furio Corà, Dinu Iuga, Colan E Hughes, Kenneth DM Harris, *High-Resolution Solid-State 2H NMR Spectroscopy of Polymorphs of Glycine,* Journal of Physical Chemistry A, **115**, 12201, (2011)

Ashkan Salamat, Katherine Woodhead, Paul F McMillan, Raul Quesada Cabrara, <u>Aisha Rahman</u>, Davy Adriaens, Furio Corà, *Tetrahedrally bonded dense C_2N_3H with a defective wurtzite structure: X-ray diffraction and Raman scattering results at high pressure and ambient conditions,* Physical Review B, **80**, 104106, (2009)

Table of Contents

List of Figures

List of Tables

Chapter 1

Introduction

1.1 Carbon Nitrides and Theoretical Predictions

Polymeric solids with high nitrogen to carbon ratios (N:C >1) have been produced and described from thermolysis condensation/elimination reactions among N-rich precursor molecules since pioneering studies by Berzelius, Liebig and Gmelin who were among the first to report on carbon nitride (C-N) materials, as early as the 1830s [1, 2]. These early discoveries have led to a large variety of useful properties that are discussed in this chapter. The interesting and useful properties of these materials that span the organic and inorganic domain of Chemistry along with speculations about their structure led to research by key scientists, such as Franklin and Pauling [3, 4].

Intense renewed interest began in N-rich C-N materials with first empirical and the computational theoretical predictions suggested that a high-density sp^3 bonded form of C_3N_4 might have a low compressibility and extremely high hardness comparable with that of diamond [5]. That work sparked high-pressure high temperature and vapor deposition synthesis experiments, and further theoretical investigations that continues to the present day.

The classification of C-N material includes purely binary C-N arrangements, as well as those that contain a small amount of hydrogen, to give $C_xN_yH_z$ formulae. While most of the interest has focused on experimental efforts to synthesise C-Ns, there has been steady increase in the theoretical investigations over the last two decades. In this thesis contribution to C-N research focuses mainly on theoretical exploration of the properties of C-N materials, using density functional theory (DFT). The theoretical predictions are complimented by experimental investigations and results, also carried out as part of this PhD thesis.

C-N materials are extremely versatile in their applications within materials science and hold the potential for further uses that have not yet been discovered. Currently it is known that incorporation of C-N into polymers provides heat and flame retardation as only N_2 (g) tends to be released when such materials are burned [6]. C-N materials are also used in the production of explosives, due to the high energy density present in these materials [7, 8]. C-N nanomaterials have been reported to exhibit fluorescence and optoelectronic properties [9]. Another commercial use for C-N material is as a thermally stable semi conductor, where the stability for graphitic C-N to oxidation is up to temperatures of 500°C [10]. The stability at such high temperatures, against oxidation of graphitic C-N is remarkable when compared with organic materials that show stability up to approximately 150°C [11]. In the area of catalysis, C-Ns have been reported to play an important role in a number of reactions [12, 13]. In recent years the discovery as a non-metallic photocatalytic material has opened new avenues for this multi-

functional class of material [14]. Recently, graphitic C-N has demonstrated the promise as a sustainable photocathode, by biopolymer activation [15].

The propulsion to gain better understanding of the structural arrangement and properties of dense C-N materials was reignited in 1985, when a theoretical paper calculated the bulk moduli for a number of hypothetical covalently bonded systems. The key postulations from the paper were C-Ns may be harder than diamond, which has a reported bulk modulus of 443 GPa [16]. When investigating the properties of any given material a number of factors need to be considered, such as the bulk modulus, covalency, bond length and so on. The bulk modulus is used as a measure of resistance of a material against plastic and elastic deformation, therefore the higher the value of the bulk modulus, the harder the material is expected to be. Bond length is an important consideration as this factor affects the strength and compressibility; shorter and stronger bonds result when a high level of covalency is present within a system. Materials that contain light elements such as C and N, have the potential to form super-hard diamond like materials, and in 1989 theoretical calculations using empirical methods predicted that a dense form of binary C-N material with C_3N_4 stoichiometry would have a higher bulk modulus than diamond; the hardest known naturally occurring material [5, 17]. This prediction acted as a springboard for further scientific interest and paved the way for numerous investigations both experimentally (to try and synthesise the ultra-hard C-N material), and theoretically (to understand the favoured bonding arrangement). Despite nearly 30 years of attempts and

thousands of publications, no unambiguous reports of a successful C_3N_4 synthetic methods is available in the literature.

In 1996 a theoretical study by Teter *et al* employing DFT offered further insights into potential phases for dense C_3N_4. The paper suggested five low energy C_3N_4 polymorphs [18]. The bonding arrangement of the atoms were based on the assumption that a dense low energy C-N structure would arise with C bonded to four N atoms and N to three C atoms. The five reported C_3N_4 polymorphs were predicted to have high bulk moduli, ranging from 425 – 496 GPa. The highest bulk modulus at 496 GPa belonged to the cubic β-C_3N_4 arrangement, clearly exceeding the bulk modulus of diamond at 443 GPa. Thermodynamic analysis suggested that the most likely conditions for the synthesis for β-C_3N_4 would be temperatures and pressures in excess of 1300 K and 50 GPa respectively [19].

1.2 Early Synthesis of Carbon Nitrides and Starting Materials

Berzelius was the first to report the synthesis of an amorphous C-N material, which was later found to have the chemical composition $C_6N_9H_3$; initially this material was known as poly(aminoimino)heptazine, later named by Liebig as 'melon' [1, 3]. The synthesis of melon makes use of melamine as a starting material, which is heated to 630°C, under the pressure of ammonia gas. At the time it was not possible to determine the structural arrangement of the material, which led to a number of proposed structures for 'melon' over the years.

It was not until very recently, in 2007 that Lotsch *et al* reported the actual characterisation of the structure for Liebig's melon. A number of analytical techniques were used to elucidate the structure, including solid state nuclear magnetic resonance spectroscopy (ss-NMR) and theoretical calculations; the formula for melon has been reported to be $[C_6N_7(NH_2)(NH)]_n$ [20]. The proposed structural image for melon reported in the paper, is represented in Figure 1.

The 1D repeating unit within melon is formed of melem monomers, also known as heptazine units, circled in red [21]. In melon the individual heptazine units are linked by N-bridges. The strands adopt a zigzag shape, held tightly in place by hydrogen bonding between the strands. Hydrogen bonding takes place due to the presence of NH_2 groups that are present on heptazine units when the N is not involved in forming the 1D strand, circled green.

Figure view restricted.

Please see reference 20 for image.
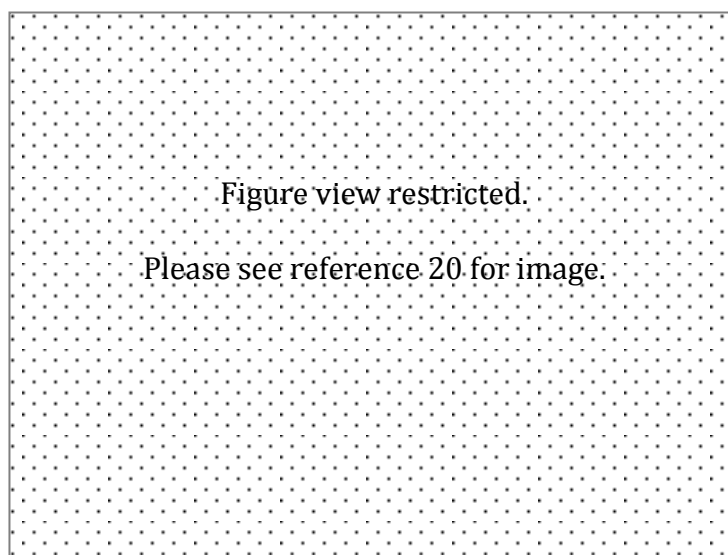
Figure 1: Structure of Liebig's Melon. H atoms omitted, C is black, N is grey. Red circle contains a single heptazine unit. Green circle highlights NH_2 groups responsible for H bonding [20]

The building blocks for melon are from a class of related C-N materials that have become well known and used in this area of Chemistry and will now be classified further in this introduction.

A number of C-N starting materials have structures that are based on oligomeric planar units, formed by the condensation of C_3N_3 rings, known as triazines. Triazine is the basis of well known and commonly used heterocyclic starting materials for C-N synthesis, examples are 1,3,5-triazine ($C_3N_3H_3$) and melamine (2,4,6-triamine-1,3,5-triazine: $C_3N_6H_6$) [20-24], the structural images are represented in Figure 2. Cyanuric chloride ($C_3N_3Cl_3$) is another widely used starting material for C-N synthesis, the structure is analogous to 1,3,5-triazine, the difference arises as Cl atoms substitute H atoms.

Triazine   Melamine   Heptazine
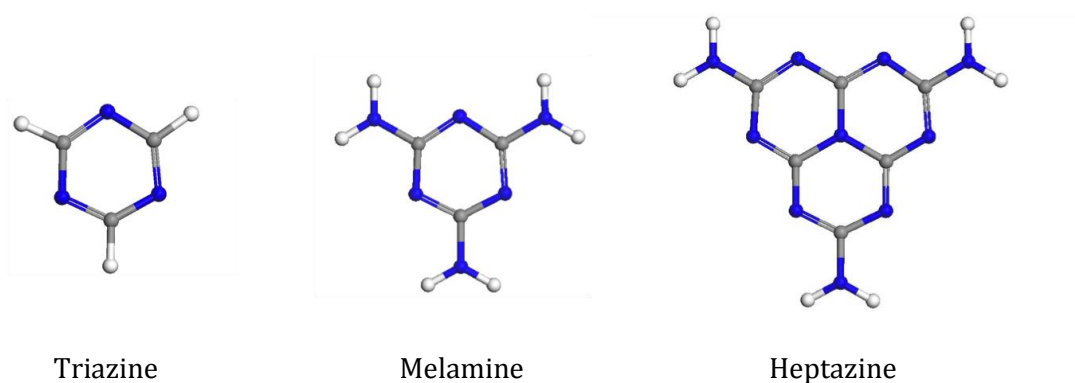
Figure 2: Structures of triazine based C-N starting materials; 1,3,5-Triazine (or commonly known as Triazine), Melamine and Heptazine. H is white, C is grey and N is blue

The melamine structure has proven to be a key starting material in the formation of a number of C-N materials and can be prepared by the condensation of another

widely used C-N starting material; dicyandiamide (DCDA). Further heating of melamine results in condensation taking place again and melamine forms a melem monomer (heptazine). Heptazine is best described as three conjoined triazine units, all linked by a central N atom, each triazine unit hosts a NH_2 group on the outer edges of the structure.

Figure 3 represents the full condensation pathway, with cyanamide as the initial starting material. A summary of the thermal condensation processes that take place at certain key temperatures is listed in Table 1.

Figure view restricted.

Please see reference 25 for image.
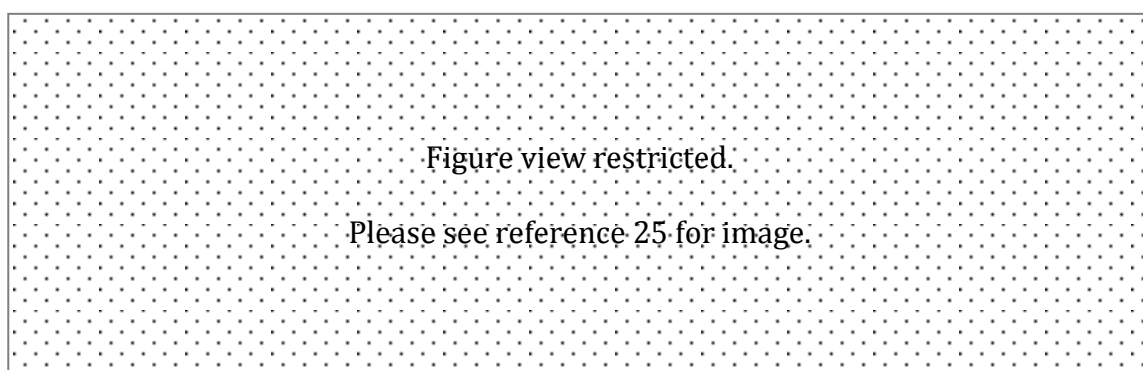
Figure 3: Scheme representing the triazine based structures, formed by thermal polycondensation of cyanamide [25]

Figure view restricted.

Please see reference 25 for image.
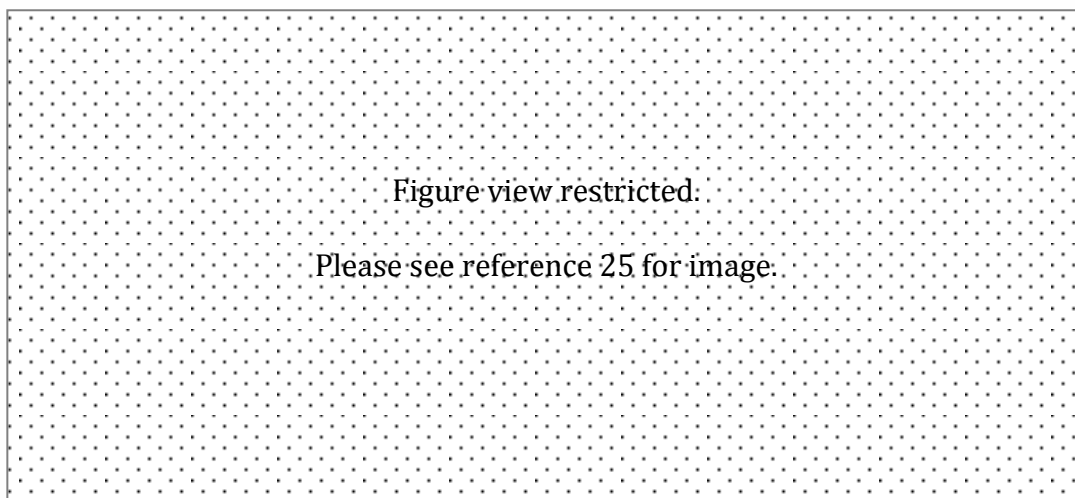
Table 1: Thermal analysis of the polycondensation of cyanamide and related processes [25]

It has generally been concluded that heptazine based structures are more stable than triazine based materials, and much of present day C-N research has been focused around these structures [26, 27]. Since both these materials have formed the basis of a number of proposed C-N structures, we have investigated the local atom environment using solid state-NMR (ss-NMR) techniques for materials we have synthesised during our research. The research surrounding the use of ss-NMR has been both computational and experimental, and the results are presented in Chapter 5 and Chapter 6.

1.3 Present Day Synthesis of Carbon Nitrides

The synthetic attempts to produce highly ordered C-N materials have resulted broadly in the crystalline or graphitic forms, giving rise to a wide variety of

structures with varying degrees of order. The different synthetic attempts and procedures are discussed in the following sections.

1.3.1 Crystalline Carbon Nitrides

Early synthetic techniques used chemical vapour deposition (CVD), where various gaseous mixtures with C, N and H were reported to have yielded amorphous C-N-H materials and crystalline forms of both α and β- C_3N_4 [28-30]. Another synthetic attempt was the pyrolysis of N rich organic precursors, for example triazine based materials, which resulted in graphitic C-N materials with a varying number of C and N atoms within the layers. The sought after C_3N_4 composition has so far managed to elude these synthetic methods and attempts [31].

One approach that reported a stoichiometry close to C_3N_4 involved the reaction of cyanuric chloride with calcium cyanamide at temperatures of ~500 °C [32]. A C_2N material with tetrahedral geometry was formed using dynamic shock wave experiments, allowing for high pressures and temperatures, using a graphitic C_3N_2 precursor, the synthesised material was reported to potentially be harder than diamond [33]. Another dynamic shock wave experiment that made use of the starting material and organic precursor dicyandiamide (DCDA) resulted in two C-N phases, importantly β-C_3N_4 was reported as one of the phases [34].

Investigations using static high-pressure (HP) studies also were used in the attempt to synthesise a dense binary C-N material, by loading graphite, amorphous

carbon in N rich environment into a diamond anvil cell (DAC). [35] A number of organic precursors have had the DAC treatment with the addition of laser heating as well, to form high pressure – high temperature (HPHT or HPT) conditions, this particular method has reported formations of sp^2-hybridised C-N material [36].

There have been a number of review articles about C-N materials, focusing on the dense form [37-39]. An extremely useful review analysed the XRD patterns for experimental data from articles that claimed to have synthesised β-C_3N_4; the ultimate conclusion stated that there was no convincing evidence that a robust method had been identified to produce β-C_3N_4, [40], leaving the solid-state chemistry of C-N materials as one of the open ground challenges of science, which can be greatly contributed towards.

In 2007 there was development made in the search for a dense crystalline C-N material, resulting from collaboration between UCL Department of Chemistry and a several German Groups. A C-N material with C_2N_3H stoichiometry was synthesised under HPT conditions, using the DAC [41]. This was the first report of a well crystallized carbon nitride that had a defective wurtzite structure, with N:C ratio of 3:2. The bonding between the elements satisfied the desired connectivity, where the C atoms were all tetrahedrally coordinated and bonded to a N atom. This discovery was critical for a number of reasons, the analogous $Si_2N_2(NH)$ is a known precursor to β-Si_3N_4, therefore it was and is hoped that a further reaction of C_2N_3H will lead to the first demonstrated synthetic path to β-C_3N_4. Unfortunately,

XRD data could not be obtained for this first synthesis of C_2N_3H, which would have provided final confirmation of the structure.

In 2009 Salamat *et al* repeated the synthesis of C_2N_3H, this time obtaining the XRD patterns at both high pressure and at ambient conditions [42]. The repeated experiment provided conclusive evidence that the crystalline C_2N_3H material did in fact have a defective wurtzite structure, which was recoverable to (and stable at) ambient conditions. As part of the initial contribution to the C-N materials in this PhD thesis, theoretical modeling of the proton ordering within the C_2N_3H defective wurtzite structure was investigated to determine the most stable arrangement [42]. The results from the study are presented in Chapter 3.

During the interpretation of the experimentally obtained XRD pattern for the C_2N_3H defective wurtzite structure it was noted that there was possibly another C-N phase present. This observation led to the search for another low energy structure with the same C_2N_3H stoichiometry. We investigated C-N arrangements using advanced theoretical structure searching techniques, the exploration of the energy landscape was conducted at a range of pressures, which allowed for identification of stable phases as well as for prediction of new candidate C-N materials. The results are presented in Chapter 4.

1.3.2 Graphitic Carbon Nitrides

There are a number of reported techniques for synthesising graphitic C-N materials, which is useful if one wants to exploit the potential of using the graphitic

form of the material, as the precursor to the dense C-N crystalline form. The use of the graphitic C-N to obtain the crystalline material is analogous to the transformation of graphite into diamond at high pressure.

The treatment of triazine-based precursors (melamine and cyanuric chloride) under HPT conditions (1 -5 GPa and 400 – 550 °C), has been reported to produce well crystallized graphitic C-N materials. A group in Bordeaux first reported the synthesis of the graphitic material in 1998 [43], a group in Arizona further expanded on the reported method in 2001, where the degree of crystallinity of the material was improved and bulk composition of the material was reported as $C_6N_9H_3$.HCl [44]. The framework for the structure was determined to be planar, with ordered $C_{12}N_{12}$ voids filled with Cl$^-$ ions (represented in Figure 4). In the diagram the equivalent numbers of N atoms on the framework have been protonated to balance the charge. The $C_6N_9H_3$.HCl structure differs from the proposed graphitic C_3N_4 structure, Figure 5, due to the presence of larger voids in the graphene plane, occupied by Cl$^-$ ions. The $C_6N_9H_3$.HCl framework is planar with alternating C and N atoms, interconnected by bridging imido groups (circled red), each imido group bridges two triazine rings contrary to the structure in Figure 5, where nitrodo groups (circled blue) bridge three triazine rings.

Figure view restricted.

Please see reference 44 for image.
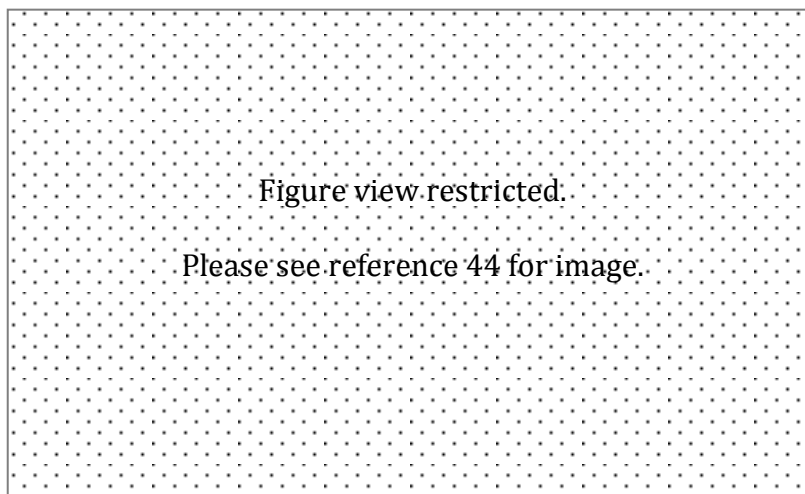
Figure 4: Proposed structural model for $C_6N_9H_3.HCl$, C is grey, N is black, H is white and Cl is the large grey ion in centre of void [44]

Figure view restricted.

Please see reference 44 for image.
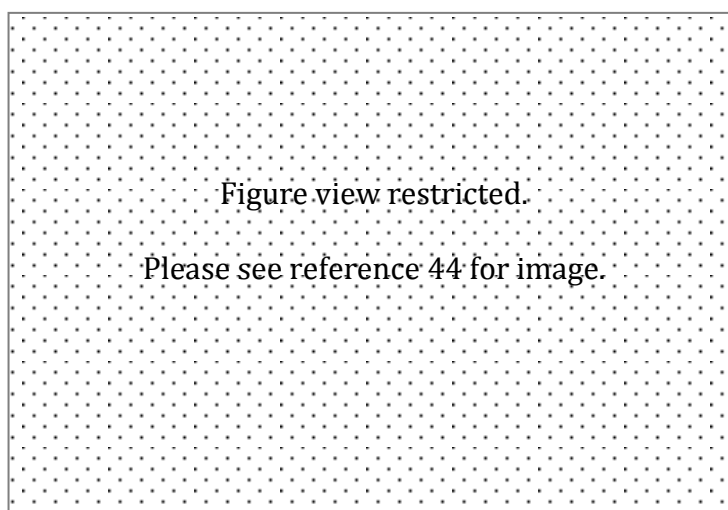
Figure 5: Proposed binary C_3N_4 graphitic phase C is grey, N is black [44]

In 2001 preliminary studies on $C_6N_9H_3.HCl$ with ABA stacking suggested that a decrease in the interlayer distance could lead to sp^3 bonding upon pressurization [45]. This led to further studies in subsequent years, in 2007 the structural

changes and behaviour upon compression was investigated for $C_6N_9H_3$ and $C_6N_9H_3.HCl$ layered structure, using theoretical modeling techniques [46]. The results showed, at $\sim$50 GPa the individual layers buckled, due to the bending of the N-H groups. The C_3N_3 triazine rings were unaffected by the initial increased pressure, remaining almost planar. Further compression of the structure (85 – 100 GPa) allowed for the interlayer bonding between C and N atoms, resulting in a new solid phase for $C_6N_9H_3.HCl$. The stability of the new phase was dependent on the content of the HCl within the material. Experimentally it was found that the HCl content was not uniform throughout the material, and compression led to a disordered solid, due to random interlayer connectivity.

In 2008 a new synthetic method was reported; employing DCDA as a starting material, this compound was polymerized in a eutectic mixture of Li/KCl molten salt under inert conditions. The final product that resulted was a highly crystalline graphitic C-N phase and the proposed structure was based on sheets of hexagonally arranged heptazine units held together by covalent C-N bonds [47]. This was generally the accepted structure for the ionothermal synthetic method until recently; in 2011 a group in Germany repeated the synthesis and reported the material to be triazine based and suggested the structure was related to $C_6N_9H_3.HCl$ as represented in Figure 6. This report was contrary to the graphitic heptazine structure previously reported. The newly characterized material was named poly(triazine imide) with intercalated Li^+ and Cl^- ions, or PTI/Li^+Cl^-. The study was supported by a number of experimental characterisation techniques; the most crucial was ss-NMR chemical shift spectra for N and C [48].

Figure view restricted.

Please see reference 48 for image.
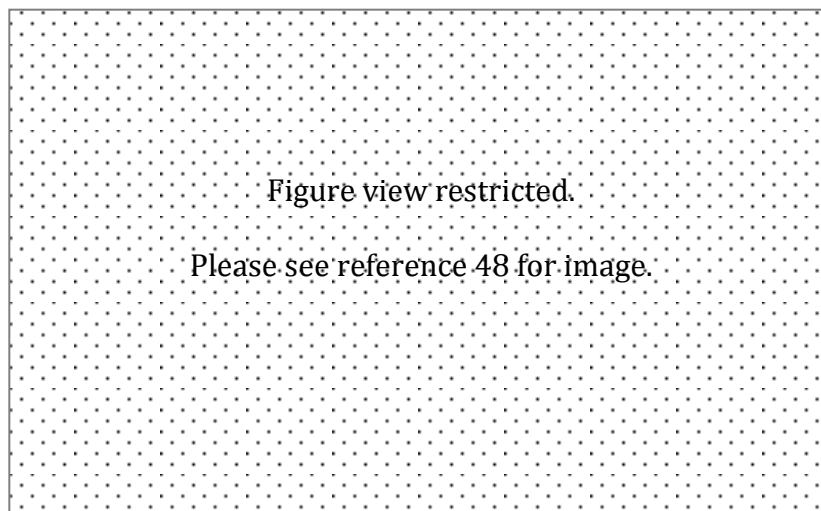
Figure 6: Proposed structure for PTI/Li+Cl- [48]

There is still some disagreement within the solid state C-N community about the actual structural composition for the finished product from the ionothermal synthetic method. In this PhD thesis we have investigated the ss-NMR chemical shifts both experimentally and theoretically for a number of C-N materials. We specifically investigated the triazine and heptazine based structures in molecular and graphitic environments. We propose that we have determined additional information regarding the finished products for the ionothermal synthetic method, and our findings are presented here for the first time. The results are presented in Chapter 6.

A number of theoretical and experimental studies have identified various graphitic C-N polymorphs that possess useful catalytic properties [13, 49-52]. These reports are most likely to have been spearheaded by a major advancement in the applications of this group of materials and the discovery in 2009 that graphitic

based C-N materials formed the basis of a new family of water-splitting photocatalysts, which results in the evolution of H_2 $_{(g)}$ from water upon visible light radiation [14]. C-N materials are particularly ideal for this due to stability of the material and ease of synthesis, both in terms of the short timeframe required and the recovery of the finished product. The layered motifs are thought to comprise of either heptazine or triazine units, linked by imido (N-H) bridging groups, however due to the nanocrystalline nature of the materials, further characterisation is difficult. As part of this PhD thesis we investigated the structure of a number of materials synthesised by this thermal method. The starting materials used for the experimental synthesis were 1,3,5-triazine, cyanuric chloride and melamine. Our specific analytical method of choice was ss-NMR that allowed an insight into the chemical bonding environment. Our NMR investigations are both theoretical and experimental, and the full set of results is presented in Chapter 6.

1.4 Summary of Research

We hope to have demonstrated the importance of C-N materials within the area of solid-state materials and the versatile and complex nature of these solids. We have dedicated part of this thesis to investigating the crystalline form of dense C_2N_3H with a defective wurtzite structure. The proton ordering has been studied within the system, with the aim of understanding how altering the arrangement affects the stability of the material (Chapter 3). In the experimental results for C_2N_3H synthesis, it appeared that there was potentially a metastable phase or polymorph

present at high pressures, this led us to enter into a collaborative project with Professor Chris Pickard, Department of Physics and Astronomy at UCL, to employ a structure searching method developed by him, to determine the possibility of another C_2N_3H structural arrangement. Our findings from the structure search are reported in full in this thesis, where the candidate structures have been compared with the experimental data available, and we propose the identification of the unknown C_2N_3H phase, which is presented in full (Chapter 4).

In a large part of our research we have used advanced theoretical methods to predict ss-NMR chemical shifts to investigate a number of C-N structural arrangements, both in molecular and crystalline form. To aid our understanding of atom connectivity we have simulated NMR chemical shifts that have been tested and scaled so that they can be compared directly with experimental results; our overall aim has been to guide our understanding of the materials synthesised experimentally (Chapter 5). We have applied our calibrated NMR prediction method to understand and interpret experimentally obtained NMR spectra, for a number of C-N materials that were synthesised using ionothermal and thermal methods (Chapter 6).

Lastly, as part of a collaborative effort with Dr Sylvie Derenne (Biogéochimie et Ecologie des Milieux Continentaux, France), we have investigated another C-N species in the form of Titan's Tholins, using ss-NMR. A full introduction into the nature of Tholins, their importance and the reason for scientific interest are presented in Chapter 7, along with the results.

Chapter 2

Methods

2.1 Theoretical Background

Computational chemistry techniques are applied widely to investigate the absolute and relative stability of materials in different phases, predict their structures and physical properties, and calculate spectra including NMR, Raman, IR etc that can used to interpret experimentally obtained data. Here DFT methods are used to investigate the structures and relative energetics of sp^2- and sp^3-bonded carbon nitride solids.

The specific areas where computational methods are employed in this thesis are :

1. Investigation of the structures and relative energetics of known versus predicted dense C-N-H polymorphs (Chapter 3);

2. Prediction of new C_2N_3H arrangements using a new ab initio structure searching technique (Chapter 4);

3. Calibration of calculated ^{13}C and ^{15}N NMR parameters for structural characterisation of graphitic C-N materials (Chapter 5);

4. Application of theoretically predicted NMR parameters to interpret the structure of layered C-N-H materials (Chapter 6)[*];

5. Theoretical NMR predictions employed to understand organic C-N molecular species, specifically tholins (Chapter 7)[±]

The computer codes used in this research make use of DFT; a practical formulation of quantum mechanics (QM) that describes the electronic structure of the system under investigation, which is a mathematical way of describing individual electrons. An alternative set of computational methods is based on interatomic potentials that describe energy as a function of bond distances and angles, without considering individual electrons. Interatomic potential methods were not employed during the research in this thesis, as empirical parameters must be known for reliable results. The complex nature of C-N polymerisation and nature of our study, limited the availability of empirical data in order to apply this method to the range of different C-N structures under study.

DFT is the current method of choice for electronic structure calculations of solids. Results collected in this thesis demonstrate and confirm that DFT is a suitably accurate method to study and explore C-N solid-state materials, supported by experimental evidence. Our work on Titan's tholins also suggests that DFT is a method to be considered when predicting NMR properties of organic C-N

---

[*] The graphitic C-N material was synthesised as part of research towards this thesis, and the experimental details are described in Appendix 1

[±] This study was additional to the main focus of C-N solids, but due to the planetary importance for understanding Titan's atmosphere, the study is presented in Chapter 7 of this thesis

structures.   As DFT is a widely used method in computational studies, our discussion will be kept brief, for further details there are a number of readily available text books, particularly recommended is Richard Martin's book titled 'Electronic Structure: Basic Theory and Practical Methods' [53].

In QM the electronic and structural properties of a given material (with M nuclei and N electrons) can be calculated by solving the Schrödinger equation, expressed in equation 2.1. The wavefunction (Ψ) is linked to the probability ($|\Psi|^2$) of finding N electrons in space.

$$\hat{H}\,\Psi = E\,\Psi$$

(2.1)

The wavefunction is dependent on all degrees of freedom i.e. electronic and nuclear coordinates, E is the associated energy and $\hat{H}$ is the Hamiltonian operator (a differential operator representing the total energy of the system).

For one-electron systems like the H atom or H_2^+, the Schrödinger equation can be solved and hence describe the properties exactly. Systems with 2 or more electrons require the introduction of approximations. The Born-Oppenheimer approximation [54] states the electronic excitations can be decoupled from nuclear motions. The nucleus is considered heavier than the electrons and does not respond as rapidly to perturbations; thus electronic excitations are considered as decoupled from nuclear motions. When mapping the structure of a molecule

against the energy, it is sufficient to do this as a function of nuclear coordinates (as the nucleus is 'stationary' in relation to electrons).

If the electrons are considered in a field of fixed nuclei, the Schrödinger equation can be expressed as equation 2.2.

$$\hat{H}_e(R)\Psi_e(r,R) = E^{eff}(R)\Psi_e(r,R)$$

(2.2)

The electronic Hamiltonian operator ($\hat{H}_e$) includes kinetic energy of the electrons and potential energy contributions (that include electrostatic attraction forces between electron and nuclei, electron-electron repulsion and nuclear-nuclear repulsion, and electron-electron exchange forces).

Solving equation 2.2 for the electronic wavefunction produces the effective nuclear potential ($E^{eff}(R)$), this forms part of the Hamiltonian that is used for studying nuclear motion. The various states of nuclear motion can then be described (rotational, transitional, vibrational) as well as the energy for the different atomic arrangements. Polymorphs that exist for the same stoichiometry will result in a new set of nuclear positions that will lead to a new electronic wavefunction, thus a new total energy that can be used to determine the lowest energy solution.

In our computational calculations, only the electronic ground state is considered, which is the lowest energy solution. The set of electronic energies calculated as a function of different nuclear coordinates constitutes the potential energy surface

(PES) for the system. An example of a hypothetical 2D PES is represented in Figure 7 with the local minima, global minimum and transition states indicated in the diagram.
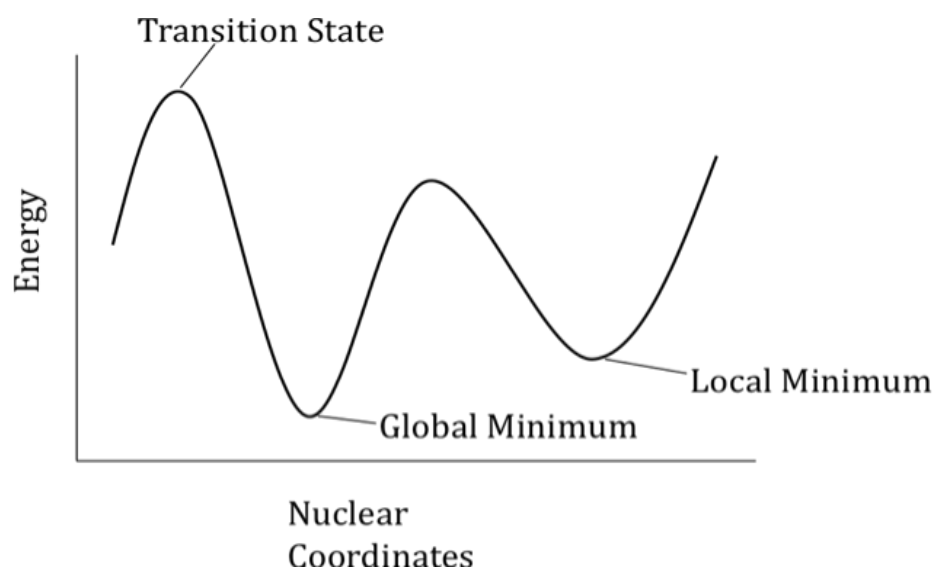
Figure 7: A hypothetical 2D potential energy surface

A number of methods have been developed to solve Schrödinger's equation. The Hartree-Fock (HF) theory uses the original many-electron wavefunction (represented in equation 2.2) and factorises the many-electron wavefunction into a set of one-electron wavefunctions calculated in the mean field generated by all the other electrons. Similar to the Schrödinger equation the HF theory seeks to solve an eigenvalue problem, the differences in the methods arise in the operator used. HF equations make use of the Fock operator [55] whose main limitation is the absence of correlation between electrons; the motion of one electron is described in the average field created by all other electrons in the system, neglecting direct correlation between electrons. Post HF-methods take into account the missing

correlation effects, examples are Configuration Interaction (CI) and the Møller-Plesset (MP) schemes [56].

DFT is an alternative method developed to solve Schrödinger's equation; it is based on two theorems proposed by Hohenberg and Kohn [57] and Kohn and Sham [58]. DFT differs to the Schrödinger equation, as instead of calculating the wavefunction of electrons, the electron density is used to derive the energy of a system [59].

In 1964, the Hohenberg-Kohn theorem stated that all properties (e.g. the energy, E) for the ground electronic state of a system can be calculated, if the ground state electron density function is known; $\rho_0(x,y,z) \Rightarrow E_0$. The ground state energy of a molecule is a functional of the ground state electron density; unfortunately the exact functional linking the two is not known. Kohn-Sham's theorem further demonstrated that the electron density for a system could be calculated using a variational method; the theorem states that a trial electron density function will give a higher energy compared with the true ground state energy. Using the variational approach the DFT energy solution can be obtained with an eigenvalue problem, similar to the Schrödinger equation, whose solution yields one electron Kohn-Sham orbitals. The Hohenberg-Kohn theory is exact, although approximations need to be introduced as the exact functional that links electron density to the energy is unknown.

DFT has an advantage over wavefunction methods, as the density is a function of the electron position in space and only has three variables (*x, y, z*). Whereas a

wavefunction method for a system with n electrons is a function of $4n$ variables, as every electron requires three spatial and one spin coordinate per electron. The complexity of wavefunction methods increases with the size of the system, whereas for DFT the electron density is always a function of only three variables. As in HF, also in DFT, energy is derived as a sum of terms, including the kinetic energy of the electrons and the Coulomb and exchange interactions between electrons and nuclei. As mentioned earlier, the exact functional for the energy is unknown, but the unknown terms are relatively small compared with the others, so a large error here will not mean a large error in the overall energy. The electron density is approximated initially to obtain the Kohn-Sham (KS) orbitals, which are then refined using a self-consistent method and the final orbitals are used to calculate the electron density.

Various approximations have been devised to correlate the electron density with the ground state energy. A hierarchy of functionals increasing in accuracy and complexity is now available. The simplest is the local density approximation (LDA), which assumes the energy contribution in each point of space, r, with density $\rho(r)$, to be identical to a uniform electron gas of the same density [60]. LDA is effective for systems with homogeneous electron density e.g. delocalised electrons in metals. For systems with localised electrons (molecules or insulating solids) LDA is less effective; bond lengths are often too short and binding energies are overestimated [61, 62].

Subsequent functionals employ a Taylor expansion of the density in r and introduce a dependence of the energy on first derivatives of ρ in (r), known as generalised gradient approximations (GGA). A number of GGA exchange correlation functionals are available: Becke-Lee-Yang-Parr (B-LYP) [63, 64], Perdew-Wang (PWGGA) [65, 66], Perdew-Burke-Ernzerhof (PBE) [67], Perdew 86 (P86) [68]. By employing GGA for the exchange correlation, a better and more flexible description of the electronic distribution is achieved; therefore an improvement on bond lengths and binding energies is obtained when compared with LDA. The GGA exchange correlation is further improved by consideration of the second derivative of the density, to yield the family of functionals called meta-GGA [69-71].

The LDA, GGA and meta-GGA methods only use the total electron density, ρ. The most accurate functionals include orbital dependent terms, which account for contributions from individual electrons; hybrid functionals are one example and include terms calculated from HF theory. Hybrid-functionals were employed as the exchange correlation functionals for the DFT calculations in this PhD thesis, and are specified in the methods section of each results chapter.

2.2 Computational Codes

The two computational codes employed for this thesis are DFT based, CRYSTAL [72] and CASTEP [73]. The main difference between the codes is the description of basis sets, which are combinations of functions used to represent the wavefunction and the electron density. CRYSTAL uses atom centered functions, expressed as

Gaussian type orbitals [74, 75], while CASTEP uses plane waves and pseudopotentials [76].

In advanced electronic structure calculations split valence basis sets are often used to describe the atomic orbitals, this is true for the CRYSTAL calculations. These are usually designated in the form X-YZ(n*), where X is the number of Gaussian functions used to describe the core orbitals, and Y and Z are the number of Gaussian functions used to describe the valence orbitals, split into two subsets (or more) for greater flexibility. The * or ** designation refers to polarization functions introduced to provide additional flexibility to the orbital functions. When beginning the study of the C-N system using CRYSTAL, a variety of basis sets were tried and tested in order to determine the one that provided the best low energy solution.

For the CASTEP calculations the basis functions used are plane waves (e^{ikr}). These are developed based on Bloch's theorem for systems described under periodic boundary conditions (PBC) [77], which states the periodic potential must be in the form shown in equation 2.3, where the electronic wavefunction can be written as the product of a lattice periodic part, $u_k(r)$, and a wavelike part, e^{ikr}.

$$\Psi_k(r) = u_k(r)\, e^{ikr}$$

(2.3)

Plane waves do not describe individual atomic orbitals and are not associated with individual atoms, rather they are delocalized over the whole unit cell. The accuracy

of the results improves with the number of plane waves used, which is dependent on the cut off energy specified. The bonding properties are mainly dependent on the valence electrons.

Core orbitals are never represented using plane waves. As the core electrons sit close to the nucleus and are not directly involved in bonding they can be approximated by the use of pseudopotential (also known as effective core potential). The approximation removes the core electrons and strong nuclear potential and replaces it with a weaker pseudopotential, as shown in Figure 8, which in turn act on pseudo wavefunctions. Plane waves used in combination with pseudopotentials provide a computationally efficient and inexpensive way to carry out electronic structure calculations for solids.
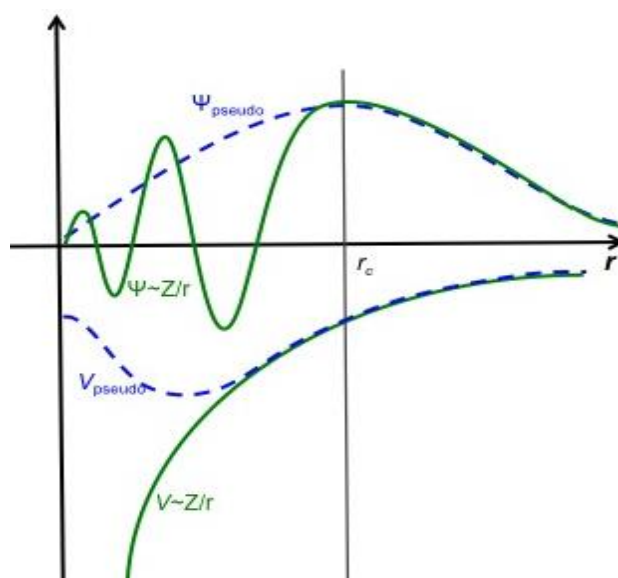
Figure 8: Electronic wavefunction (Ψ) and electronic potential (V), solid green line, against the distance from the atomic nucleus (r). The dashed blue line represents the pseudo wavefunction and pseudo potential. Outside a given radius, r_c, the pseudo and actual values are the same

The cost of QM methods increases with system size; DFT based techniques can currently be applied routinely for predicting properties of materials with up to sizes of a few hundred atoms. An alternative approach to model complex structures in the field of computational science, is by the use of interatomic potentials, also known as semi-classical methods.

In semi-classical methods the total energy of the system is expressed as a function of the nuclear co-ordinates, while the electrons are not treated explicitly. The bond distances and bond angles are used to determine the total energy of the system, either by numerical or analytical techniques. Interatomic potentials are used to describe the forces between the atoms. This method has been successful for a range of solid-state materials as well as large organic molecules [78, 79]. Depending on the material under investigation, the construction of the interatomic potential varies, due to the nature of the bonding within the system. Semi-classical methods rely on empirical data to derive the interatomic potential parameters that are adjusted iteratively in order to achieve the lowest energy solution [80].

One of the objectives of this thesis is to establish the behaviour of C-N solids under a range of conditions, from ambient to extreme conditions of high pressure and temperature and to define the structural and spectroscopic behaviour of different polymorphs. There are two main components that need to be considered, firstly to refine properties of structures already identified experimentally and secondly to predict new plausible C-N structures by exploration of the PES. In this work, the code CRYSTAL has been employed for the former problem and CASTEP for the

latter. Since the chemistry of C-N systems is unknown at high temperature and pressure, conditions and could involve sp^2/sp^3 hybridisations that are difficult to reproduce in the parametric forms with interatomic potentials, the work carried out is at the QM level, specifically employing DFT. Carbon-nitride structures have been studied with both CRYSTAL and CASTEP codes; however for the larger systems, spectroscopic properties and calculations associated with structure prediction, CASTEP was better suited in terms of time and capability. The area of work related to structure prediction, requires sampling of the PES, not only in the close neighbourhood of a pre-identified minimum (equilibrium structure), but globally. Techniques for such a global investigation of the PES in solids are still in their infancy, and in general more complex than energy minimisation. They require a statistical sampling of the global PES, and often thousands of starting geometries need to be considered.

Only recent advances in computer resources have made structure prediction methods applicable to solids of real chemical interest, such as the C-N systems studied here. In our work we used a recent development in the area of structure prediction, ab initio random structure searching (AIRSS), which is discussed in section 2.3 and Chapter 4 [81].

2.3 Structure Prediction

Predicting the structure of molecules and materials at an atomic level is a continued area of interest in a number of scientific fields, not least Chemistry. A number of methods have been devised using computational techniques to accurately model

known structures; however predicting thermodynamically stable structures using only the chemical composition is a continued challenge. Given the topical interest there area a number of recent reviews and special issues of journals dedicated to this problem, for instance the review article in 2010 by Catlow *et al.*, in PCCP [82]. Employing purely empirical methods such as data mining, relies of comparison and extrapolation from known structures [83]. The majority of approaches, define a cost function (a measure of the quality of structure), a concept that is based on global optimisation; a search is conducted on the specified atomic composition to identify regions enclosing minima in the cost function [82].

A number of structure prediction methods are available; these include simulated annealing, genetic algorithms and threshold algorithms. These methods are often formed on the basis that one starts at a local minimum and from that point explores the energy landscape, either close to the original starting point or quite far (known as basin hopping). In using traditional structure prediction techniques such as simulated annealing [84, 85] there are high energy barriers that must be overcome in order to break bonds, to allow restructuring/reforming, before a new structure can be made. In genetic algorithms bond breaking and reforming is part of the process; two selected parent structures are used to form 'off-spring' where the 'child' has characteristics of both parent structures [86]. Evolutionary algorithms is another method that draws parallels with nature in which competition to survive and procreate is simulated, from a population created by number of starting configurations at random stationary points in the energy landscape. The probability of survival is based on the defined cost function, hence an evolution of

the sought after low energy structures occurs [87]. A molecular packing approach is often employed for crystals, where the modes of packing are systematically investigated after energy minimization [88, 89].

Due to the strong C-N bonds in carbon nitrides, and the complex nature of the PES formed by many deep narrow minima, an exhaustive exploration of the PES to identify stable structures is very challenging.

In our work we applied the AIRSS method [81], which allows unbiased exploration of the PES without introducing bias into the system, as well as overcoming the problem of very strong carbon-nitride bonds, which can either be single, double or triple; adding a further dimension of complexity to the problem that we are trying to solve. This method is not based on starting at local minima and then forcing a way over the energy barrier into the next local minima (as they are likely to be surrounded by high energy barriers), before the metastable structures for the C-N system can be found. In AIRSS one begins with randomly assembled non-bonded atomic ensembles and this does not require the cleavage of strong C-N bonds from the initial structure.

The AIRSS method of structure searching is simple yet effective at generating new structures. Once the chemical composition is specified, the atoms are randomly located within the unit cell and geometry optimization is applied; information regarding the system after optimization is gathered and compared against the other structures generated, i.e the energy, space group, volume etc. This process is

repeated a number of times, to sample the entire energy landscape of the system. Figure 9 represents the basis of the method.
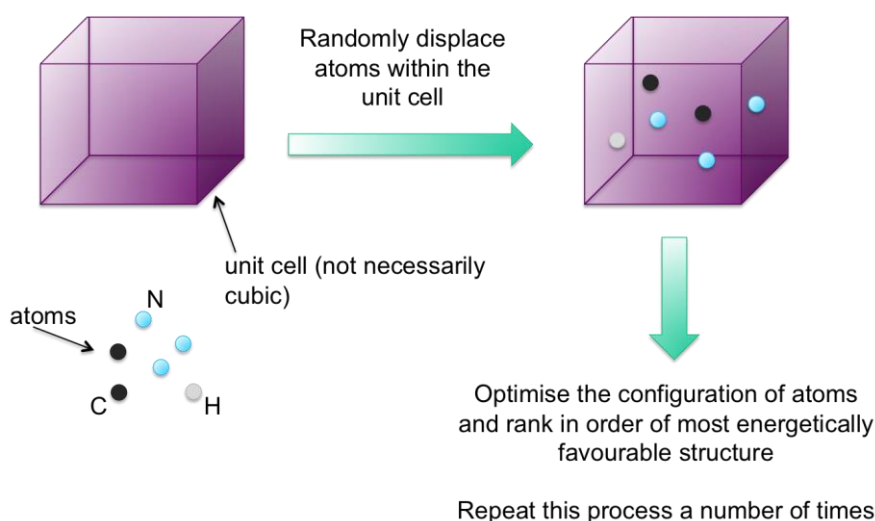
Figure 9: A diagram representing the process of the AIRSS method for structure prediction

The structure search can have a number of constraints applied to the system; these constraints include atoms that are set at a predefined distance apart, dimers or molecules are used instead of atoms, specified co-ordination for certain atoms in the system can be displaced in the unit cell to guide the connectivity. The pressure can also be specified for each of the searches, which is useful considering the nature of the experimental technique used within the research group, for the synthesis of C-N materials. The specific constraints applied for the investigations using AIRSS to explore the C_2N_3H stoichiometry, are discussed in further detail in Chapter 4.

We focused our AIRSS searches to materials with C_2N_3H stoichiometry. As mentioned in the introduction, a proposed dense material with a defective wurtzite structure was reported with this composition [41]. The same C_2N_3H stoichiometry is common to the graphitic C-N material with known structure [44]. Exploring the PES for C_2N_3H materials is important to the understanding polymorphism in carbon nitrides, as the existence of the known materials in the structure search can be used to judge their success. One of the goals of this research is to identify a new phase observed in high pressure XRD patterns that cannot be solved using experimental observations alone. The starting precursors i.e. DCDA, contain C-N and N-H, but not C-C, C-H and N-N bonds; the latter bonds are not expected to appear in the synthesised materials. A useful feature of AIRSS is the structures generated are independent of one another; this prevents the structure prediction work from being 'stuck' in a well on the PES surrounded with high-energy barriers. Due to the strong covalent bonds in C-Ns, we expect alternative approaches that use structure evolution to be of limited success and slow.

The particular advantage of the AIRSS method is the approach is completely unbiased (unless a user defined constraint is applied), therefore in searching the energy landscape, one is able to obtain structures where the connectivity within the system has not evolved from a previous structure. This increases the likelihood of finding new novel structures. The high-energy barriers that exist within the PES would act as a limitation when using other methods, hence affecting the chances of success. However, it should be mentioned that a limitation to the AIRSS method is the number of atoms used within a unit cell is restricted to approximately 12, as the

geometry optimization step per structure of this size becomes time consuming (approx. 1 day) for the method to still be considered efficient. Although with the rapid and continuing advancement in computational power even this limitation will most likely be overcome in the near future.

2.4 Nuclear Magnetic Resonance Background

In this thesis Chapters 5 to 7 employed NMR methods to understand the C-N materials and the local atom environment; the following pages will look at the background of this method.

Due to the nanocrystalline nature of the synthesised C-N materials (Chapter 5 and 6) and the nature of Tholins (Chapter 7), NMR was the method of choice to understand the local atomic connectivity of these materials. NMR exploits the magnetic properties of the nuclei as a probe to determine the atomic environment, from which chemical bonding can be determined. NMR can be used to study the structural environment of molecules and crystals, in the liquid or solid phase, the material under investigation can be fully recovered at the end of NMR treatment.

NMR was simultaneously discovered by two research groups; both publishing the first NMR spectra in 1946 [90, 91]. The chemical shift, the most important effect of NMR, was first observed for ^{14}N and ^{31}P [92-94]. We now know for an element to be 'NMR active' the angular momentum properties of the particle are essential. The spinning nucleus is positively charged and generates a magnetic field, giving the magnetic moment (μ) that is proportional to the spin, which is a vector as it has

both magnitude and direction. The magnetic moment is analogous to a charge that moves in a circle and creates a magnetic field (Figure 10). NMR studies of C-N materials can exploit ^{1}H, ^{13}C and ^{15}N nuclei.
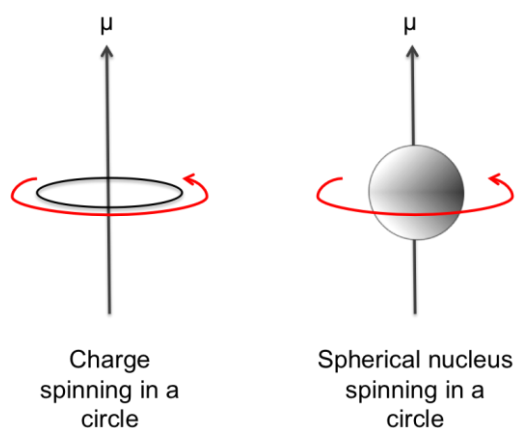
Figure 10: Analogy between a charge and a spherical nucleus spinning in a circle

The spin state of the nucleus is fundamental to NMR. In heavier elements the combination of the protons and neutrons define the overall spin of the nucleus and when the atomic number and mass are both even the nucleus does not have measureable magnetic properties, hence the spin quantum number (I) is zero. When either of the atomic number or mass is odd the nucleus has magnetic properties that can be measured as the nucleus has a spin state, the spinning nuclei can only have particular values either integral or fractional, i.e. ½, 1, $^3/_2$, 2, etc. The C, N and H nuclei whose NMR chemical shifts were measured or theoretically predicted in this PhD thesis all have I = ½, which is the most common spin state as well as the easiest nuclei to examine by NMR. The energy levels are same for nuclei of the same isotopes, when there is not a strong external magnetic field

present. When an external magnetic field, B_0, is applied along the *z*-axis there is a change in the energy of the nuclei.

The magnetic moment either aligns with (*+z*) or against (*-z*) the general direction of the external magnetic field, for nuclei with I = ½ they can only assume these two arrangements (I_z = +½ or I_z = -½). For nuclei where I = 1, $^3/_2$, 2…etc, there are more than two arrangements possible when an external magnetic field is applied. The splitting of the spins states into 2I + 1 levels is known as the Zeeman effect. The nuclear magnets do not align to be parallel to the +z or –z direction, rather they move in a circular motion around the ±z direction, this motion is termed precession (Figure 11). The nuclei whose precession motion is in the +z direction have slightly lower energy than those in the –z direction. In the absence of an external magnetic field the precessional motions are also absent, and the nuclei possess the same energy.
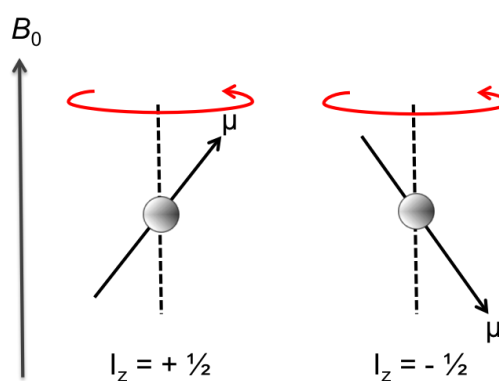
Figure 11: Zeeman effect and precession caused when an external magnetic field is applied to nuclei with I = ½

The difference in energy between spin states is dependent on the external magnetic field, as the strength of B_0 increases so too does the energy difference between the spin states (Figure 12).
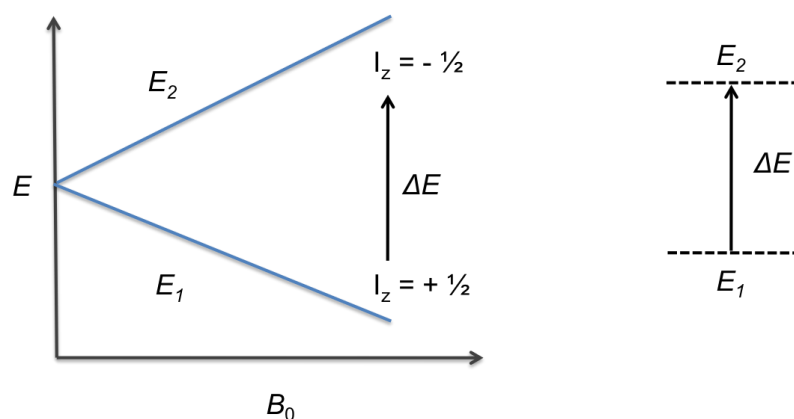
Figure 12: Effect of B_0 on the difference in energy between spin states

The difference in energy levels can be described by the Bohr frequency condition:

$$\Delta E = \Delta E_2 - \Delta E_1 = h\nu$$

(2.4)

Where ν is the frequency of the absorbed or emitted radiation resulting from transition. The magnitude of the magnetic moment is specific to each element and can be summarised by the following formula:

$$\mu = \gamma I$$

(2.5)

Where γ is the gyromagnetic ratio, which is a characteristic of the nucleus, thereby unique to every isotope, which is a crucial fact for NMR spectroscopy. The Larmor frequency is the angular frequency (ω) for the precessional motion of the magnetic moment around the external magnetic field, and is proportional to B_0.

$$\omega = 2\pi\nu$$

(2.6)

The proportionality constant between B_0 and ω is the gyromagnetic ratio, and can be represented as follows:

$$\omega = \gamma B_0$$

(2.7)

By irradiating the nuclei with the correct Larmor frequency energy that corresponds exactly to the spin state separation for a specific set of nuclei, will result in the nuclei in the + ½ spin state to flip to – ½ and vice versa with the absorption or emission of the energy taking place respectively, the nuclei are said to be in resonance. The resonance frequency is highly dependent on the structural environment of the nucleus and these do not overlap between elements or isotopes due to the difference in the gyromagnetic ratio, making NMR an excellent method to determine the structural environment within a system. Figure 13 represents the difference in energy between the spin states for ^{1}H, ^{13}C and ^{15}N.
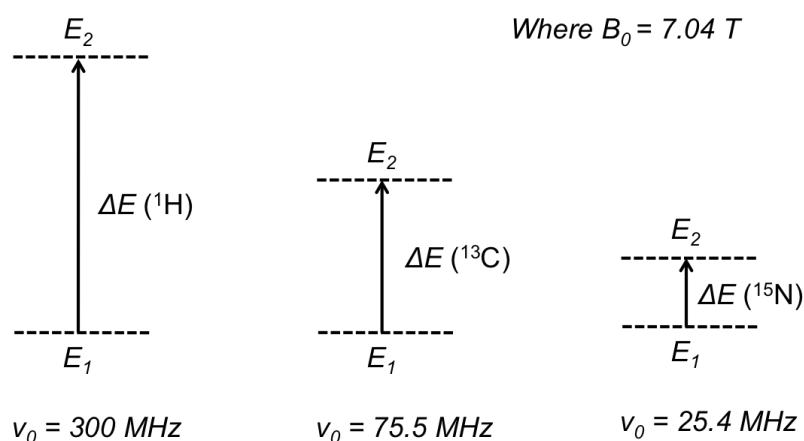
Figure 13: The difference in energy for three nuclides ^{1}H, ^{13}C and ^{15}N with various relative magnitudes of γ; 26.75, 6.73 and 2.71 respectively

Once the nuclei have been excited to a higher energy state by irradiation of the corresponding Larmor frequency, the spins will return to the initial equilibrium condition after a period of relaxation time T_2 and T_1, these are by transfer of energy to the surroundings (*spin-lattice relaxation*) or by redistributing the energy among various other nuclear spins in the system (*spin-spin relaxation*) respectively.

There is another magnetic field experienced by the nucleus other than B_0; electrons are charged and they produce an additional magnetic field as they move around the nucleus in molecular orbitals. This magnetic field created by the electrons affects the external magnetic field around the nucleus, as the electrons precess in the direction of B_0 this creates an opposing magnetic field, which shields the nucleus. The chemical shielding, σ, lessens the effective field experienced by the nucleus and is represented in Figure 14.

$$B_{eff} = B_0(1-\sigma)$$
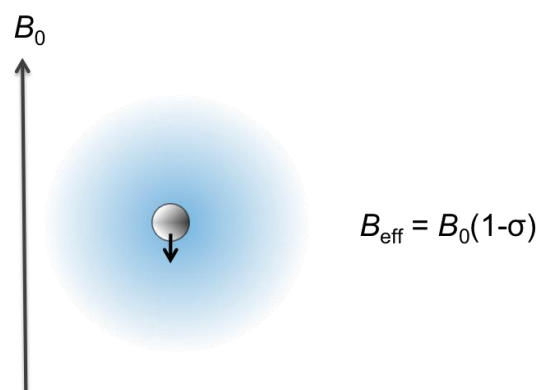
Figure 14: The electrons surrounding the nucleus precess in the direction of the external magnetic field, causing shielding of the nucleus

The differences in the electron density surrounding each non-equivalent nucleus in a molecule or crystal results in each nucleus experiencing a different B_{eff}, these differences give rise to the phenomenon of the chemical shift, δ. The chemical shift is a measure of frequency (ν) with respect to a reference standard (ν_{ref}), for ^1H and ^{13}C this is tetramethylsilane (TMS), for ^{15}N nitromethane is often used, δ is reported in parts per million (ppm).

$$\delta = ((\nu - \nu_{ref}) / \nu_{ref}) \times 10^6$$

(2.7)

While performing experimental NMR, absolute frequencies are not actually measured, instead the reference material for the nuclei under study is used and frequencies of lines are measured relative to a specific reference line in the spectrum, the chemical shift can be expressed as

$$\delta = (\sigma_{ref} - \sigma_{sample}) / (1 - \sigma_{ref})$$

$$(2.8)$$

Where σ_{ref} is much smaller than 1, the chemical shift term is simplified to

$$\delta \approx \sigma_{ref} - \sigma_{sample}$$

$$(2.9)$$

For our theoretical predictions we based our δ values on equation 2.9, where we calculated the isotropic chemical shielding (σ) for the reference standard and the material of interest to calculate the chemical shift by substituting the experimental values with our theoretically predicted values ($\delta \approx \sigma_{calculated\ ref} - \sigma_{calculated\ sample}$).

In liquid samples the effects of chemical shielding anisotropy (the non-symmetrical distribution of electrons in the chemical bonds), is averaged out by the rapid molecular tumbling of the solution, as the magnetic field experienced by the nucleus is determined by the orientation of its bonds with respect to the magnetic field. As a result of the averaging many of the line broadening interactions are reduced to zero.

In solid-state materials line broadening interactions are not removed as with liquid samples, which results in broad signals. Since the molecules in a solid are more rigidly fixed, the Zeeman interaction can no longer be considered a number, but it becomes a tensor property; chemical shielding, dipolar and quadrupolar interactions are tensor quantities too. Magic angle spinning (MAS) is a crucial

solid-state NMR experimental technique that reduces or even removes line broadening. In MAS the sample is spun at 54.74° to the magnetic field, causing the effects of the tensor properties to vanish. In order for MAS to be effective the spinning rate must be larger than the characteristic time-scale of the interaction being removed; the faster the spin rate the less the effect of the chemical shielding anisotropy, resulting in sharp isotropic chemical shifts. The experimental NMR spectra obtained in this research applied the MAS.

Cross polarization (CP) experiments are very useful and could be considered essential when studying solids; polarization is transferred from nuclei with a high gyromagnetic ratio i.e. ^{1}H, to those with dilute spin and low abundance e.g. ^{15}N. The natural abundance of ^{13}C and ^{15}N is approximately 1.108% and 0.37% respectively [95]. The cross polarization method was used to obtain the ^{13}C and ^{15}N NMR chemical shift spectra, for the C-N materials prepared during the research for this thesis.

Another technique within the NMR experimental method is CP-MAS with interrupted decoupling; in this method irradiation of the sample is interrupted (stopped) for a short time (i.e. in the region of 5 – 10 milliseconds) after which irradiation is applied again and the NMR spectra is acquired. One can think of this as looking at one atom through another i.e. looking at ^{13}C through ^{1}H. If the nuclei that is under study, is directly attached to a ^{1}H atom the chemical shift signal will decay at a faster rate than if the ^{1}H is attached to a near-by equivalent nuclei. Figure 15 illustrates what the NMR chemical shift spectra is expected to look like, if

the nuclei is directly attached to ^{1}H atom and a 'CP-MAS interrupted decoupling' experiment is conducted. This aspect of the NMR method is important in determining whether the ^{1}H atom is directly connected to ^{13}C or ^{15}N within the C-N material. Due to its importance the interrupted decoupling method has been used to obtain new information as part of our investigations in this thesis.
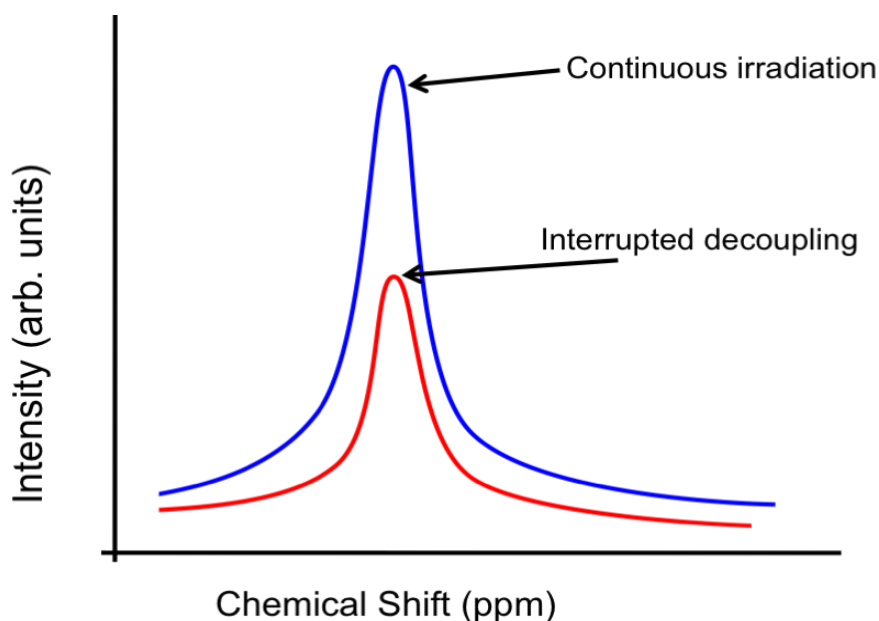
Figure 15: Schematic of NMR spectra where the intensity of the chemical shift collected by continuous irradiation (blue) is affected by applying interrupted decoupling to the irradiation of the nuclei (red) that is bound directly to the coupled nuclei

A large part of the NMR research in this thesis involved obtaining experimental spectra for the synthesised C-N materials, as well as calculating the predicted chemical shifts for specific C-N environments. The CASTEP code was employed for the NMR calculations, once the modelled structures had undergone geometry optimisation. The "gauge including projector augmented-wave" (GIPAW) method

[96-98] was used in the NMR shielding calculations for the optimised geometries of C-N structures, the isotropic shielding values (in units of ppm) were reported in the CASTEP output file; these were referenced to the calculated reference structures i.e. TMS or nitromethane, to obtain the chemical shift (in units of ppm). A structure was considered suitably converged with respect to NMR calculations, when the equivalent atoms in a structure gave rise to the same NMR output results i.e. the same isotropic shielding values. The CASTEP NMR predictions were compared for a range of structures with experimentally known results, and a scaling formula was derived; the process and formulas applied is described in Chapter 5. The NMR applications on C-N structures are presented in Chapters 6 and 7 of this thesis.

Chapter 3

Defective Wurtzite C₂N₃H Prepared by HPT Synthesis; Determination of N-H Orientations

3.1 Introduction

A relatively new solid state C-N material was synthesized within the McMillan group at UCL Department of Chemistry, as reported by Horvath-Bordon *et al* [41]. The compound was prepared from the starting material DCDA in a laser heated DAC at pressures greater than 27 GPa and temperatures of approximately 1800 K. The material was found to be a dense tetrahedrally bonded carbon nitride phase, and was shown to have C_2N_3H chemical composition and defective wurtzite structure with $Cmc2_1$ space group. The defect within the structure can be described as the nitrogen atoms occupy half the tetrahedral sites and the tetrahedral carbon atoms fill 2/3 of the sub-lattice, the remaining vacant bonds in the chemical system are completed by hydrogen attached to nitrogen atoms. The structural model was confirmed by the x-ray diffraction data obtained for the material at high pressure as well as at ambient conditions, confirming the material had been recovered without undergoing a phase transition during recovery. Although the XRD pattern was able to confirm the structural arrangement, the orientation of the N-H bonds could not be determined by experimentally available

techniques. We have investigated this problem with theoretical modeling, with two possible directions available, corresponding to two N lone pairs not engaged in the C-N bonds.

The aim of research presented in this Chapter, was to determine whether there was a preferred orientation of the hydrogen atoms within the defective wurtzite C_2N_3H structure. Alteration of the proton ordering gave rise to three different proton arrangements for the C_2N_3H material (Figure 17) that were studied for their stability and behaviour over a range of volumes and pressures. The system was modeled using the CRYSTAL code, in which two different hybrid functionals were tested, which allowed for comparison between the methods.

The results showed the overall structure of the system to behave in a similar manner upon compression independently on the orientation of the N-H groups; however there was one arrangement of the protons that was confirmed to be energetically favourable. The XRD pattern generated for the favoured atomic arrangement of the geometry optimised theoretical model was compared with data obtained experimentally, and showed good agreement.

3.2 Computational Detail

CRYSTAL was employed to carry out full geometry optimizations for the three C_2N_3H polymorphs with the defective wurtzite structure, as represented in Figure 17. The local minima were determined on the potential energy surface, at varying unit cell volumes, in order to obtain detailed information about structural behavior as pressure is applied to the system. In the calculations the B3LYP and PBE0 hybrid functionals were employed, this allowed for comparison of results obtained with the two hybrid functionals.

DFT calculations were carried out under periodic boundary conditions. All atoms were described with an all electron 6-21G** basis set. Full geometry optimizations of the periodic systems were carried out to determine the local minima on the potential energy surface using analytical gradients of the energy with respect to atomic positions and cell parameters. Symmetry was preserved throughout the optimizations. The SCF convergence threshold was set to 1×10^{-7} Hartree on the total energy. Calculations were performed using Pack-Monckhorst grids for integration in reciprocal space, with k-point nets of 4X4X4. The effects of pressure were simulated by performing a series of constant volume geometry optimizations, in which the volume varied between 109% and 90% of the ambient-pressure values. Following the constant-volume optimizations, a cubic fitting of the internal energy (E) vs volume (V) curve was employed to calculate pressure and enthalpy. Bulk moduli and their first derivatives were obtained from the E(V) results using a third order Birch-Murnaghan equations of state (Equation 3.1) [99].

$$P(V) = 3K_0 f(1 + 2f)^{5/2}\left[1 + \frac{3}{2}(K_0' - 4)f\right]$$

$$(3.1)$$

K_0 is the zero pressure bulk modulus and K_0' is its pressure derivative. Transforming the volume strain into the reduced variable, equation 3.2, and using the normalized F, equation 3.3, provides a lineraised version of the P(V) equation (3.1) for useful determination of K_0 and K_0' values.

$$f = \frac{1}{2}\left[\left(\frac{V_0}{V}\right)^{2/3} - 1\right]$$

$$(3.2)$$

$$F = P[3f(1 + 2f)^{5/2}]^{-1}$$

$$(3.3)$$

The experimental lattice parameters and refined fractional coordinates at ambient pressure for the recovered synthetic material for the C and N atomic coordinates are presented in Table 2.

Lattice Parameters	a (Å)	b (Å)	c (Å)
	7.618 (5)	4.483 (2)	4.038 (1)
Fractional Coordinates	*x*	*y*	*z*
C	0.325 (3)	0.328 (3)	0
N1	0.310 (1)	0.364 (4)	0.358 (2)
N2	0	0.285 (3)	0.422 (4)

Table 2: Experimental lattice parameters and refined fractional coordinates for the

C_2N_3H structure [42]

Upon completion of the geometry optimization, the simulated XRD patterns were generated for the optimized structure using PowderCell [100], which were then directly compared with experimentally obtained data, in order to confirm structural agreement. The experimental XRD patterns were obtained and provided by Ashkan Salamat and Katherine Woodhead, at beamline I15 of Diamond Light Source in Didcot, UK and ID27 of the European Synchrotron Radiation Facility, Grenoble .

The three C_2N_3H polymorphs, with the varying proton ordering are presented in Figure 16. The differences in the orientation of the protons can be described as follows in the three polymorphs; 'DefWur' the arrangement is based on the experimentally reported results, 'Afe' is due to the protons being orientated in an antiferroelectric fashion(where the adjacent dipoles of the H circled in yellow are in opposing axial directions) and 'Horiz' is due to all the protons being horizontal

when the structure is viewed along the c-axis, all the protons in this final structure are antiferroelectric.
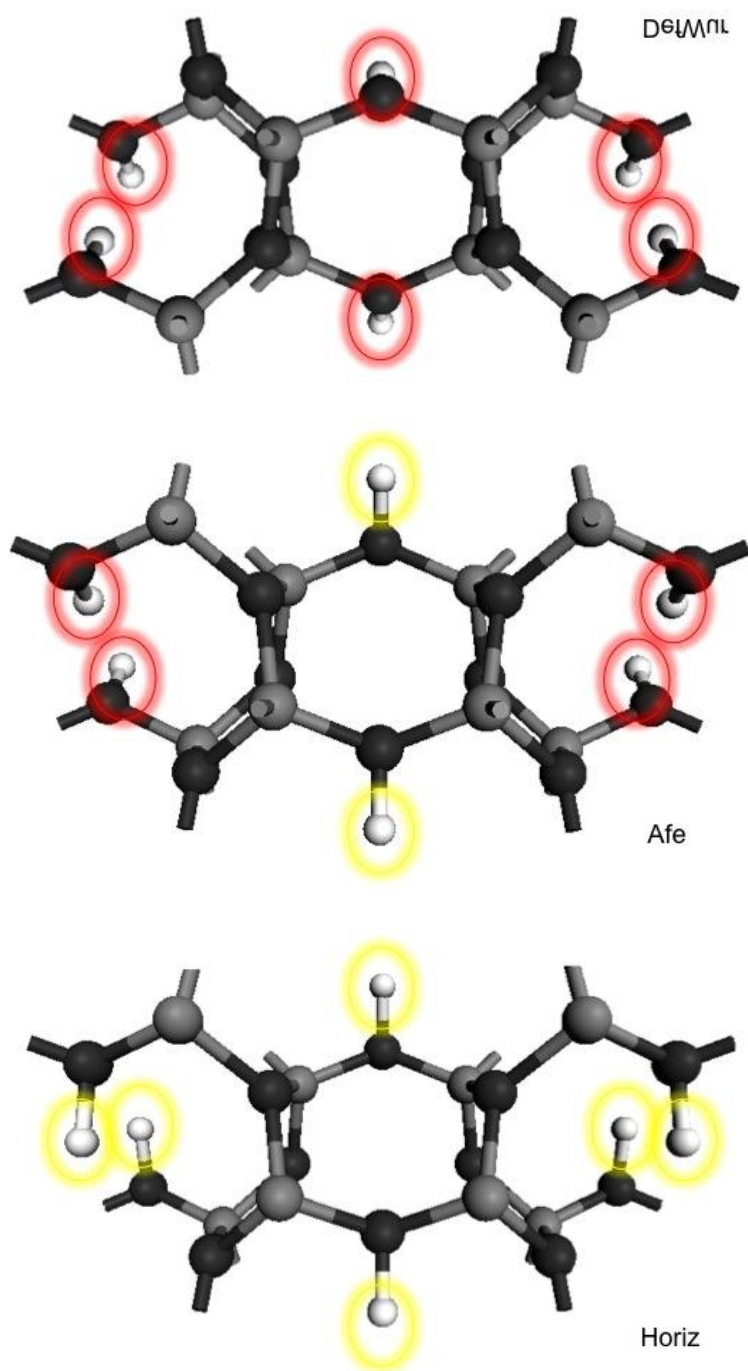
Figure 16: Images representing C$_2$N$_3$H defective wurtzite structure, and the three different polymorphs arising from the arrangement of proton ordering, labeled DefWur, Afe and Horiz. (C is grey, N is black, H is white)

3.3 Results and Discussion

The behaviour for the three polymorphs and the calculated internal energy (Ha) at equilibrium using B3LYP and PBE0 hybrid functionals, are represented in Figure 17(a) and Figure 17(b) respectively, over a range of volumes. The full data set is presented in Table 3 to 5.
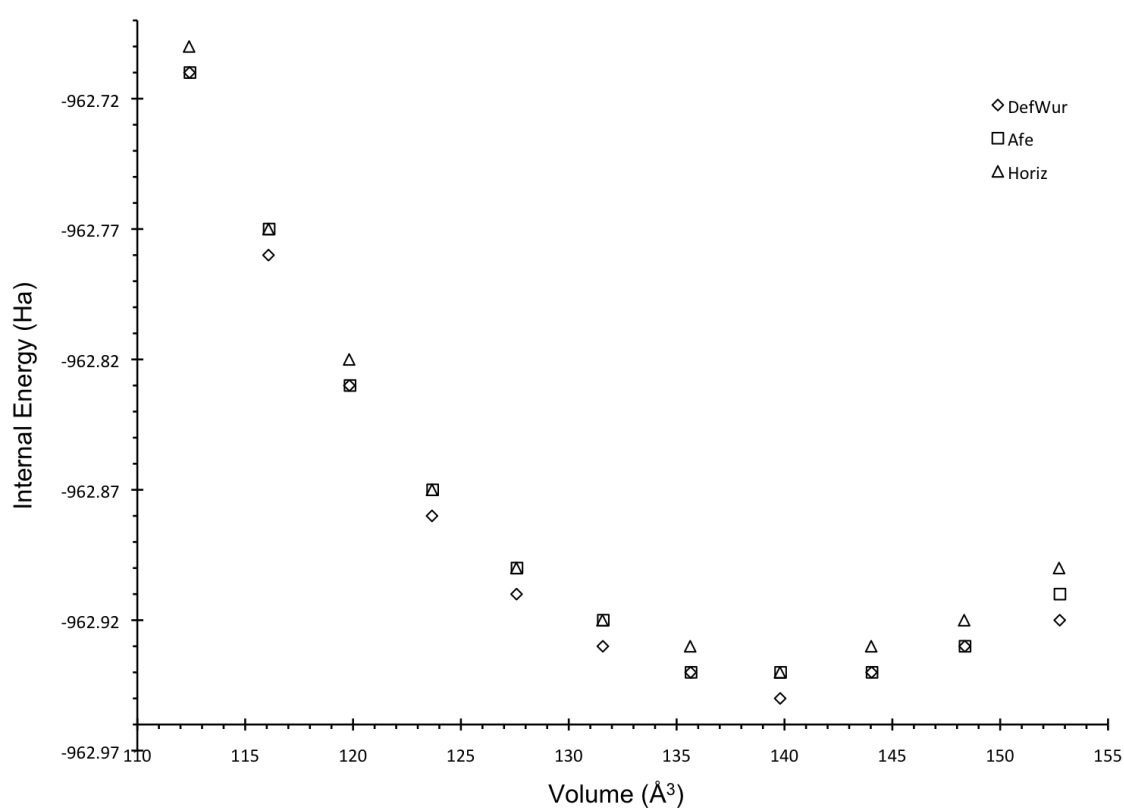
Figure 17(a): Calculated Internal Energy (Ha) at varying unit cell Volumes ($Å^3$) for the DefWur, Afe and Horiz structures using the B3LYP hybrid functional
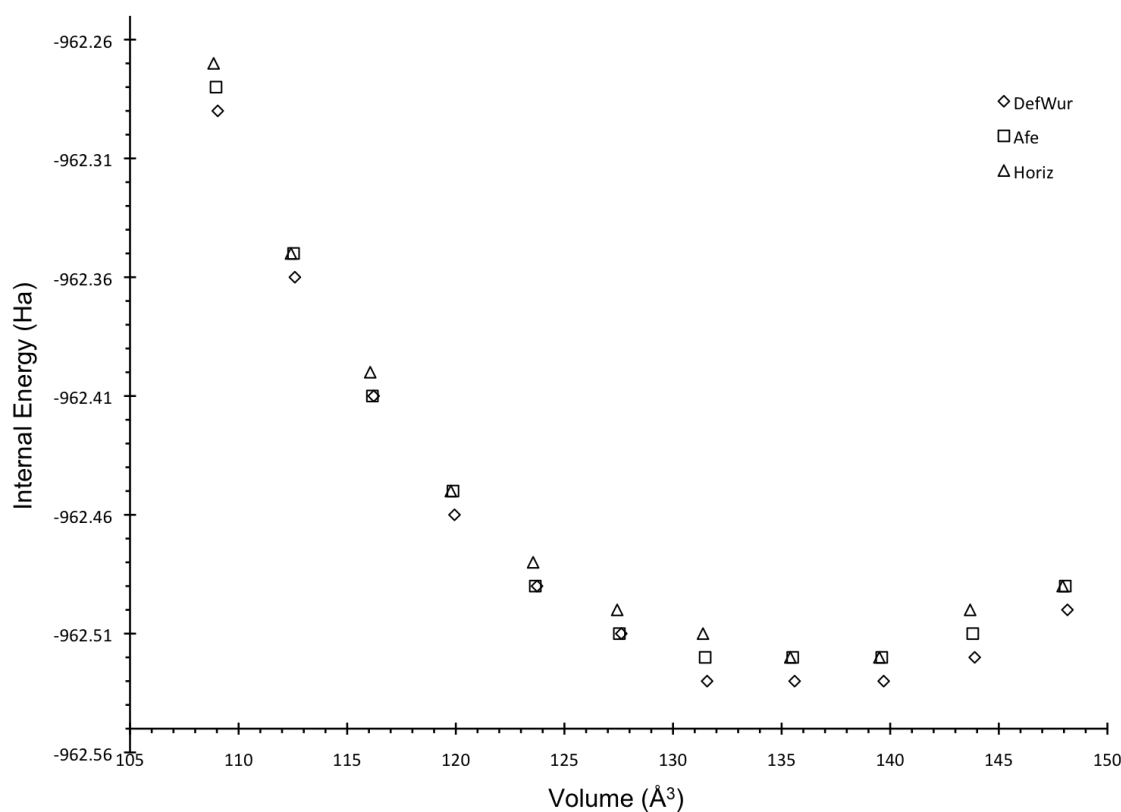
Figure 17(b): Calculated Internal Energy (Ha) at varying unit cell Volumes (Å³) for the DefWur, Afe and Horiz structures using the PBE0 hybrid functional

The three different C_2N_3H polymorphs remained stable over the range of volumes examined and behaved similarly for both sets of hybrid functional calculations. The original C_2N_3H defective wurtzite structure was the most energetically favourable arrangement, as calculated and shown for both B3LYP and PBE0 hybrid functionals. The next most stable proton arrangement was for Afe, this structure transformed into the DefWur structure at five volumes for B3LYP and three for PBE0 calculations. The Horiz structure was the least stable arrangement for the three different proton ordered C_2N_3H structures. Energy differences between the phases were very small, at approximately 0.01 Ha or less, at each volume.
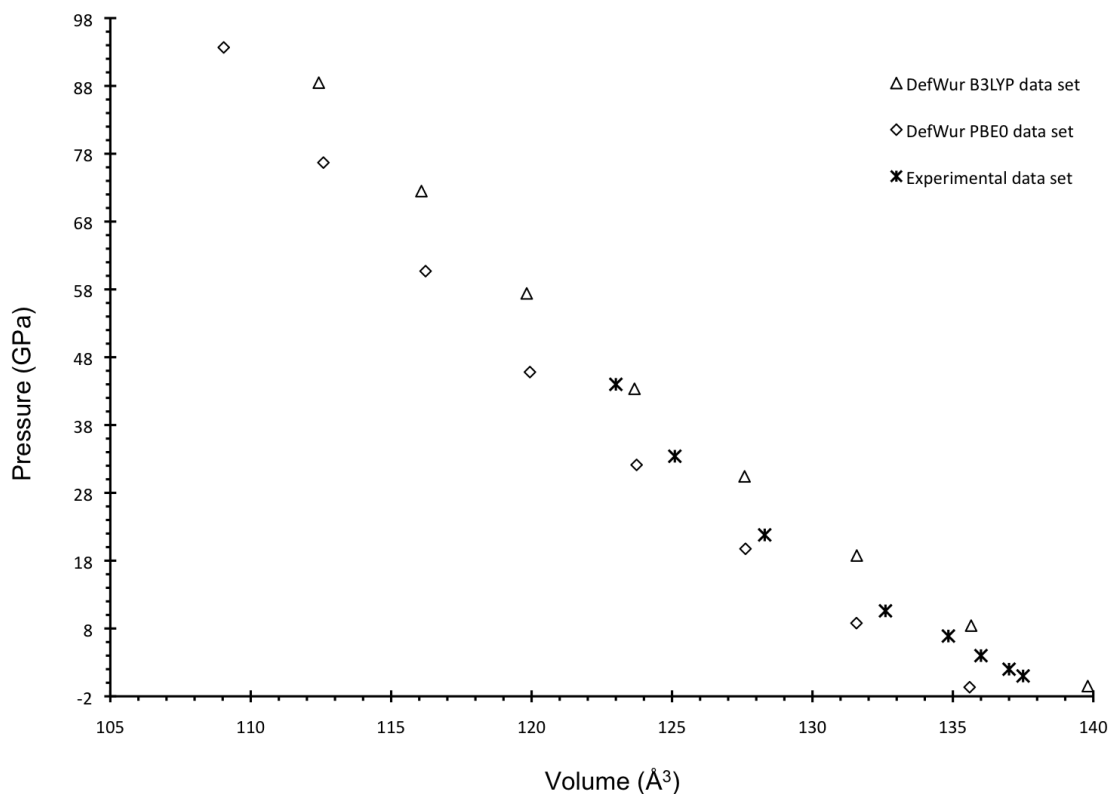
Figure 18: Comparison of experimental and theoretical data for the DefWur structure at differing Pressure (GPa) and Volume ($Å^3$)

The B3LYP calculations systematically underestimated the volume, whereas the PBE0 calculations systematically over estimated the volume, and the experimental data was shown to fit almost evenly between the two, as represented in Figure 18. The data indicate that the experimentally derived bulk modulus value K_0 = 258 ± 21 GPa with K_0' = 6.3 ± 0.8 is in good agreement with the theoretical calculations for the DefWur structure (B3LYP K_0 = 271 GPa, K_0' = 3.97 and PBE0 K_0 = 288, K_0' = 3.94). The bulk modulus for the DefWur structure is comparable with that determined for the refractory high-hardness ceramic Si_3N_4, K_0 = 256 GPa [101]. The full data set of the ambient lattice parameters and bulk modulus, for all investigated structures is presented in Table 3.
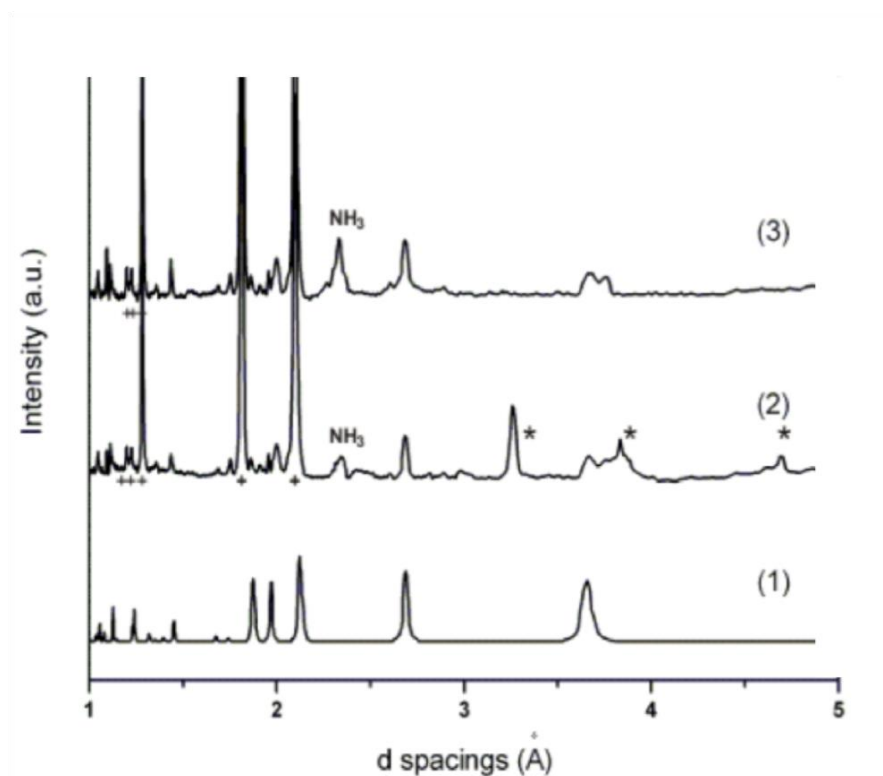
Figure 19: XRD pattern obtained at 45 GPa, following laser heated-DAC synthesis of DCDA starting material. (3) Pattern obtained *after* extended laser heating and (2) *before* the initial laser heating period. Additional peaks (*) correspond to an unidentified C-N-H metastable phase formed during initial synthesis, and (1) theoretically predicted XRD pattern for C₂N₃H with a Defective Wurtzite structure

Comparison of the experimental XRD patterns obtained at high pressure and ambient conditions, with the theoretically optimized defective wurtzite structure, showed excellent agreement as presented in Figure 19. The experimental XRD pattern contains a number of peaks that cannot be assigned to the defective wurtzite structure, and may indicate the presence of a new phase.

The theoretical XRD pattern represents a pure C_2N_3H defective wurtzite structure, which allows for assignment of the experimental XRD pattern and confirmation of the synthesised material. The theoretical results were used to identify the presence of ammonia (NH_3) and its interference with the XRD pattern. The peaks for the metastable phase disappeared when the sample was recovered to ambient conditions. One peak at 2.3 Å remained, which could not be assigned to the C_2N_3H defective wurtzite structure, when compared with the theoretical predication. The experimental observations reported the release of ammonia gas upon the opening of the diamond anvil cell; subsequently the peak at 2.3 Å was attributed to the presence of ammonia gas trapped in the sealed diamond anvil cell. The theoretical XRD pattern allowed for the structure identification at high pressure, as well as highlighting the presence of an unknown phase, (marked with * in Figure 19). The theoretically generated XRD pattern also confirmed the presence and identification of NH_3 gas. The synthesis of C_2N_3H with a defective wurtzite structure, from DCDA can be expressed in the chemical equation 3.4.

$$C_2N_4H_{4\,(s)} \xrightarrow[\text{2500-2800 K}]{\text{30-45 GPa}} C_2N_3H_{(s)} \quad + \quad NH_{3\,(g)}$$

DCDA

Defective Wurtzite Structure

(3.4)

B3LYP Hybrid Functional											
DefWur				**Afe**				**Horiz**			
Volume (Å^3)	Pressure (GPa)	Internal Energy (Ha)	Enthalpy (Ha)	Volume (Å^3)	Pressure (GPa)	Internal Energy (Ha)	Enthalpy (Ha)	Volume (Å^3)	Pressure (GPa)	Internal Energy (Ha)	Enthalpy (Ha)
152.76	-17.80	-962.92	-963.54	152.77	-17.51	-962.91	-963.52	152.73	-17.19	-962.90	-963.52
148.36	-13.71	-962.93	-963.40	148.37	-13.44	-962.93	-963.38	148.33	-13.24	-962.92	-963.37
144.04	-7.91	-962.94	-963.21	144.06	-7.70	-962.94	-963.19	144.02	-7.62	-962.93	-963.18
139.80	-0.49	-962.95	-962.96	139.82	-0.39	-962.94	-962.95	139.79	-0.41	-962.94	-962.95
135.65	8.42	-962.94	-962.68	135.67	8.40	-962.94	-962.67	135.63	8.28	-962.93	-962.67
131.58	18.76	-962.93	-962.36	131.60	18.57	-962.92	-962.36	131.56	18.37	-962.92	-962.36
127.58	30.43	-962.91	-962.02	127.60	30.03	-962.90	-962.02	127.57	29.76	-962.90	-962.03
123.66	43.34	-962.88	-961.65	123.69	42.71	-962.87	-961.66	123.66	42.38	-962.87	-961.66
119.83	57.41	-962.83	-961.25	119.86	56.50	-962.83	-961.27	119.82	56.12	-962.82	-961.28
116.08	72.49	-962.78	-960.85	116.11	71.30	-962.77	-960.87	116.08	70.87	-962.77	-960.88
112.42	88.48	-962.71	-960.43	112.44	87.02	-962.71	-960.46	112.40	86.61	-962.70	-960.47
PBE0 Hybrid Functional											
DefWur				**Afe**				**Horiz**			
Volume (Å^3)	Pressure (GPa)	Internal Energy (Ha)	Enthalpy (Ha)	Volume (Å^3)	Pressure (GPa)	Internal Energy (Ha)	Enthalpy (Ha)	Volume (Å^3)	Pressure (GPa)	Internal Energy (Ha)	Enthalpy (Ha)
148.16	-18.96	-962.50	-963.14	148.06	-18.54	-962.49	-963.12	147.94	-18.04	-962.49	-963.10
143.89	-14.64	-962.52	-963.00	143.80	-14.38	-962.51	-962.98	143.68	-14.07	-962.50	-962.97
139.70	-8.50	-962.53	-962.80	139.61	-8.37	-962.52	-962.79	139.50	-8.22	-962.52	-962.78
135.60	-0.66	-962.53	-962.55	135.51	-0.62	-962.52	-962.54	135.40	-0.60	-962.52	-962.54
131.57	8.79	-962.53	-962.26	131.48	8.75	-962.52	-962.26	131.38	8.70	-962.51	-962.25
127.62	19.75	-962.51	-961.94	127.53	19.66	-962.51	-961.93	127.43	19.57	-962.50	-961.93
123.74	32.12	-962.49	-961.58	123.66	32.00	-962.49	-961.58	123.56	31.90	-962.48	-961.58
119.94	45.81	-962.46	-961.20	119.87	45.67	-962.45	-961.20	119.77	45.59	-962.45	-961.19
116.22	60.69	-962.41	-960.80	116.16	60.55	-962.41	-960.79	116.06	60.56	-962.40	-960.79
112.59	76.69	-962.36	-960.38	112.53	76.57	-962.35	-960.37	112.41	76.74	-962.35	-960.37
109.04	93.67	-962.29	-959.94	108.96	93.68	-962.28	-959.94	108.85	93.96	-962.27	-959.93

Table 3: The calculated volume (Å^3), pressure (GPa), internal energy (Ha) and enthalpy (Ha) for the three proton ordered phases of the defective wurtzite C_2N_3H polymorphs (DefWur, Afe and Horiz)

Structure	PBE0			B3LYP			
	DefWur	Afe	Horiz	DefWur	Afe	Horiz	Experimental
Space Group	$Cmc2_1$	$Pmc2_1$	$Cmc2_1$	$Cmc2_1$	$Pmc2_1$	$Cmc2_1$	$Cmc2_1$
a (Å)	7.580	7.581	7.583	7.656	7.659	7.663	7.618
b (Å)	4.447	4.421	4.393	4.500	4.475	4.447	4.483
c (Å)	4.023	4.043	4.065	4.058	4.079	4.102	4.038
K_0 (GPa)	288	285	281	271	267	264	258
K_0' (GPa)	3.94	4.04	4.18	3.97	3.94	4.01	6.3
Vol (Å³)	135.596	135.510	135.399	139.803	139.824	139.786	137.904

Table 4: Unit cell information obtained using PBE0 and B3LYP hybrid functionals for the optimised C_2N_3H polymorphs (DefWur, Afe and Horiz), alongside the experimental data

Volume (Å³)	Pressure (GPa)
123.00	44.00
125.10	33.40
128.30	21.80
132.60	10.60
134.84	6.89
136.00	4.00
137.00	2.00
137.50	1.00

Table 5: Experimentally obtained volume (Å³) and pressure (GPa), for the recovered C_2N_3H material

3.4 Conclusion on the N-H ordering for Defective Wurtzite C_2N_3H

DFT calculations were used to confirm experimental results and to investigate the C_2N_3H material with defective wurtzite structure. A number of different proton positions were simulated and the results showed the proton ordering to cause an indistinguishable change to the overall structure or the compressibility parameters. The energy optimizations within all three structural arrangements converged and suggested they may each occupy a subsidiary minimum within the PES. Experimentally this can be interpreted that the recovered material may correspond to either one of the proposed structures.

The XRD patterns generated theoretically for the optimized structure were used to identify the defective wurtzite phase from the experimental data. Initially the XRD assignment was difficult due to the presence and interference of ammonia in the results, as well as the presence of an unknown phase, which was identified to exist at high pressure. We provide a possible identification to the unknown phase, using a DFT structure prediction method, in the following chapter.

The DFT results showed excellent agreement with the experimental data and allowed for a better understanding of the overall proton arrangement of the C_2N_3H defective wurtzite structure and the interpretation of the XRD patterns. The theoretical results gave an additional insight into the experimental process, specifically in the assignment of NH_3 gas, and supporting the understanding of the presence of a metastable phase.

Chapter 4

Exploring the C-N-H Energy Landscape using the *Ab Initio* Random Structure Searching (AIRSS) Method

4.1 Introduction

As discussed in Chapter 3, a HPT method was reported to produce a new dense nanocrystalline carbon nitride material, which was recovered to ambient conditions [42]. The recovered material had a defective wurtzite structure and C_2N_3H composition. At high pressure it was noted in the XRD pattern there was potentially another phase present alongside the defective wurtzite C_2N_3H phase. The phase present at HPT disappeared upon extended laser heating of the sample, suggesting the possibility of a metastable C_2N_3H structure.

A previously reported characterisation of the XRD pattern for material obtained from shock synthesis experiments, (using the DCDA as a precursor) assigned the pattern to the β-C_3N_4 theoretically predicted phase [34]. The study of DefWur in the previous chapter, suggests that the XRD pattern corresponds to DefWur along with intermediate C_2N_3H phases [42]. In this chapter, structure searching techniques is

applied to confirm the plausible existence of more than one C_2N_3H phase during synthesis. The XRD patterns for the low energy structures are presented and compared with experimental results.

The AIRSS method was employed to explore the C-N-H energy landscape with the aim to find a new structure with C_2N_3H stoichiometry that may account for the unknown peaks of the XRD pattern, presented in the previous chapter. The AIRSS method was successful, and a C_2N_3H structure with a different arrangement to the known defective wurtzite structure is proposed. The computationally predicted findings fit with the experimental XRD data available.

An important aspect to analysing the results is being able to predict the pressures at which the polymorphs exist, and crucially at what pressures they change in stability, relative to one another. Figure 20 illustrates two points at which two different structures with the same stoichiometry exist. The structures are stable and the calculated final enthalpy (eV) is at equilibrium i.e. coordinates (V1, E1) and (V2, E2). The mathematical expression combining the Enthalpy (H), Internal Energy (E), Volume (V) and Pressure (p) is represented in equation 4.1.

$$H = E + pV$$

(4.1)

H is the enthalpy of the system. E is the internal energy, which is the total energy contained by the system i.e. kinetic and potential energy.
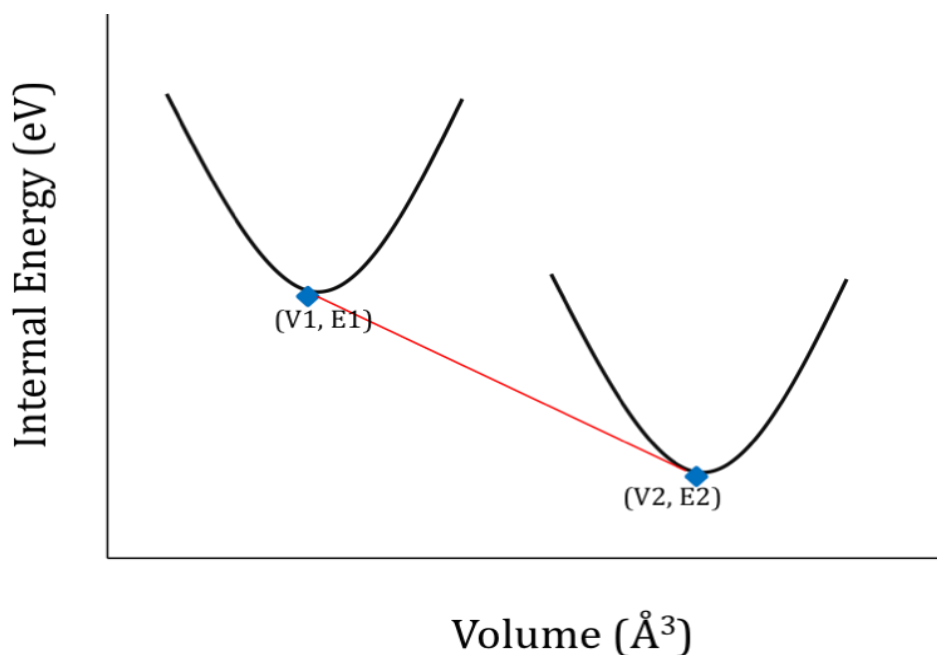
Figure 20: Energy Landscape where two structures are calculated to be at chemical equilibrium. The red line is the gradient between the two points, which is also the pressure at which (V1,E1) is predicted to be isoenthalpic to (V2,E2)

In order to calculate the predicted pressure at which a phase transition between two structures (with the same stoichiometry) takes place, a simple rearrangement of equation 4.1 provides the formula to be applied. The formula that is used to analyse the pressures between polymorphs, is represented in equation 4.2. When E is expressed in eV and V in Å³, and the equilibrium pressure in GPa (between phases 1 and 2), a scaling factor of 0.006 is applied.

$$\text{Pressure (GPa)} = \left(\frac{E1 - E2}{V1 - V2} \right) \div 0.006$$

(4.2)

The energy landscape for the C_2N_3H stoichiometry was explored in detail, and the predicted XRD patterns were generated for the lowest energy structures. The detail of the AIRSS method has been presented in Section 2.2, further detail regarding the constraints applied during the implementation of the method is discussed in Section 4.2.

4.2 Computational Detail

AIRSS searches were conducted at a range of pressures for materials of C_2N_3H stoichiometry, between 1 GPa and 75 GPa. Exploiting high performance computing (HPC) the searches begin generating new structures in a short time frame, as the code is parallelized over a number cores allowing for generation of results to be fast (1000s of structures within 5 days). The Legion HPC cluster at UCL was employed to run the calculations and CASTEP was the DFT code used to optimize the structures generated from the AIRSS method. The cut off energy for the DFT calculations was set to 500 eV and k-point spacing was 0.07 Å; these parameters were 'fine' enough to allow the results obtained to provide good information about the optimized cell, and 'coarse' enough to allow fast geometry optimizations for several hundred different initial configurations. The ultrasoft pseudopotentials available from the CASTEP library were used for the C, N and H atoms. Symmetry was exploited in this method by using the 'symmetry_generate' command, which would search for symmetry rotations and translations within the unit cell. Another use of symmetry was the command 'symm_ops', where the user starts with a unit cell that already has defined symmetry, and a further 1, 2, 3... symmetry operations are applied to the atoms in the unit cell. The resulting unit cell has double the

number of atoms than the starting geometry, which becomes the new unit cell for geometry optimisation. The use of symmetry reduces the computational time and allows for an increase in the number of atoms within the unit cell. This maximizes the chances of finding new C-N structures. The searches were conducted in order of increasing 'constraints', which are outlined below.

1. Random – no constraints applied at all on the atoms within the unit cell or the unit cell itself.

2. Minsep – a minimum separation distance between atoms is defined i.e. 0.5 or 1 Å. This avoids wasting computational time in optimizing unit cells where the atoms have randomly been placed very close (< 0.5 Å) to one another.

3. Dimer – atoms already bonded to one another are randomly placed within the unit cell i.e. C-N and N-H, this is useful for guiding connectivity of the overall system.

4. Symm-Ops – applies additional symmetry operations to the starting geometry of atoms in the unit cell.

5. Coordinated – final atom coordination is specified in the cell input file i.e. C to make 4 bonds and N to make 3 bonds, in the final structure. This is also useful in guiding the overall connectivity of the system.

The constraints applied to the individual AIRSS search are indicated for each search, in the results section.

In order to visualise the structures generated the Materials Studio software was used. For the generation of XRD patterns for the optimized structures the Powder Cell software was employed.

4.3 Results and Discussion

4.3.1 C_2N_3H AIRSS Search

The AIRSS structure search method was applied to cells with C_2N_3H stoichiometry, with either 1 or 2 formula units per cell, without imposing symmetry constraints at 1, 25 and 50 GPa pressures. Constrained searching was implemented at 75 GPa, by either specifying the minimum separation between atoms, applying symmetry operations or specifying the coordination the C and N atoms. The list of pressures and conditions specified in the AIRSS search is summarised in Table 6.

C_2N_3H Stoichiometry	
1 formula unit	**2 formula unit**
1 GPa	1 GPa
25 GPa	25 GPa
50 GPa	50 GPa
75 GPa 0.5 Å*	75 GPa C±
75 GPa 1 Å*	-
75 GPa 1x2§	-
* = minimum separation defined § = two symmetry operations applied on 1 unit cell ± = coordination of atoms defined C4, N3	

Table 6: Summary of the pressures and constraints applied to AIRSS search on

C_2N_3H stoichiometry

The searches above pressures of 50 GPa generated more than 3000 structures. In order to analyse the AIRSS results for each condition examined, the energy

landscape is described by plotting i.e. a graph collecting equilibrium volume (V, in units $Å^3$) and enthalpy (H, in units eV) of each structure generated and then optimised with CASTEP. For each search a selection of structures chosen from different regions of the (H, V) diagram is presented. In the images C is grey, N is blue and H is white. The simulated XRD patterns are generated, from the same search and energy landscape where the known defective wurtzite C_2N_3H structure is 'found', for a range of predicted structures. At the end of the AIRSS analysis five candidate structures have been identified and selected from 'accessible' enthalpy regions, for which the relative stability has been calculated as a function of pressure. We finally compare the calculated results with the XRD pattern for the metastable C_2N_3H phase observed experimentally.

4.3.1.1 C₂N₃H, 1 Formula Unit, 1 GPa Random Search
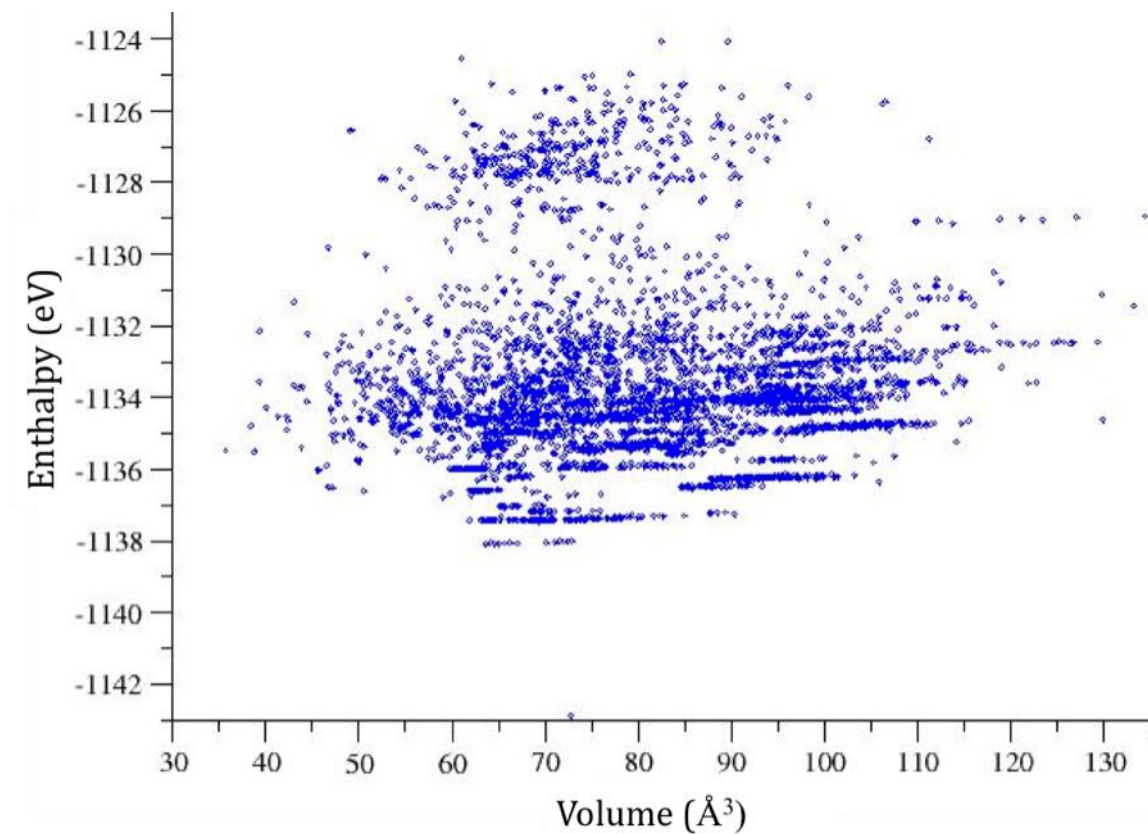
Figure 21: Energy Landscape for C$_2$N$_3$H, 1 Formula Unit at 1 GPa Random Search

Figure 21 represents the PES in which the different C$_2$N$_3$H configurations exist, for the AIRSS search performed at 1 GPa using 1 formula unit (6 atoms) and not specified constraints. Searches at 1 GPa were the most computationally expensive, due to the length of time involved for the geometry optimizations to complete. This can be explained with the presence of several layered structures, which are held together by dispersion forces, as in graphite. Such forces are not represented in DFT, resulting in a very shallow energy minimum as a function of interlayer separation, that causes problems of numerical stability in the geometry

optimization procedure. A large number of structures generated in this search contained C-C or N-N bonds.

The lowest energy structure (5201) is 5 eV more stable than all other structures; the system is molecular rather than crystalline, and is best described as a combination of N_2 interacting with polyacetonitrile chains. The overall combined molecule for structure 5201 has three terminate N atoms, two of which are involved in H-bonding with the adjacent molecule. The bond length for N_2 bonding to the polyacetonitrile chain was 1.52 Å, and may mean that N_2 exists as a molecule, but is drawn to the polyacetonitrile structure due to the H-bonding. A potential candidate structure was the next lowest in energy (7026) that formed AAA stacked layers with alternating C-N bonds and the H atoms attached to the N, this structure shared the same motif with the experimentally recovered defective wurtzite C_2N_3H material. A single layer within the defective wurtzite three-dimensional structure can be described as a defective-BN motif, with the B site occupied by ⅔ C atoms and ⅓ H atoms.

A selection of structures from different regions of the energy landscape is presented in Table 7; most structures with enthalpy values of -1335 eV or above were found to be 1D. The least stable structures were found to exist primarily in molecular form and C-N-H fragments.
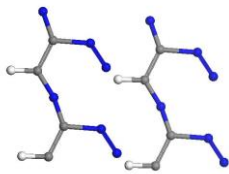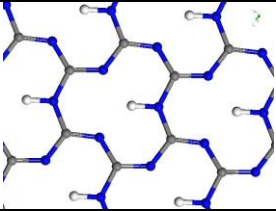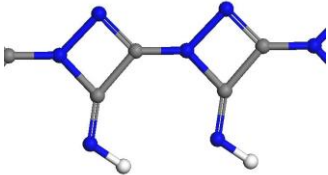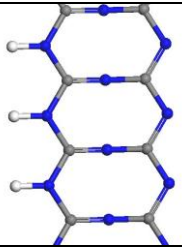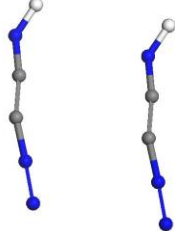
Structure Identifier and (Dimension)	Enthalpy (eV)	Volume (Å^3)	Space Group	Structure Image
5201 (Molecular)	-1142.9	72.8	P1	
7026 (2D)	-1138.1	63.6	Imm2	
6863 (3D)	-1135.5	35.7	Cm	
9500 (2D)	-1135.5	75.4	P1	
2329 (2D)	-1137.4	63.5	C2/m	
6128 (Molecular)	-1134.4	99.9	P1	

Table 7: Structure details for C_2N_3H, 1 Formula Unit at 1 GPa Random Search

4.3.1.2 C_2N_3H, 1 Formula Unit, 25 GPa Random Search
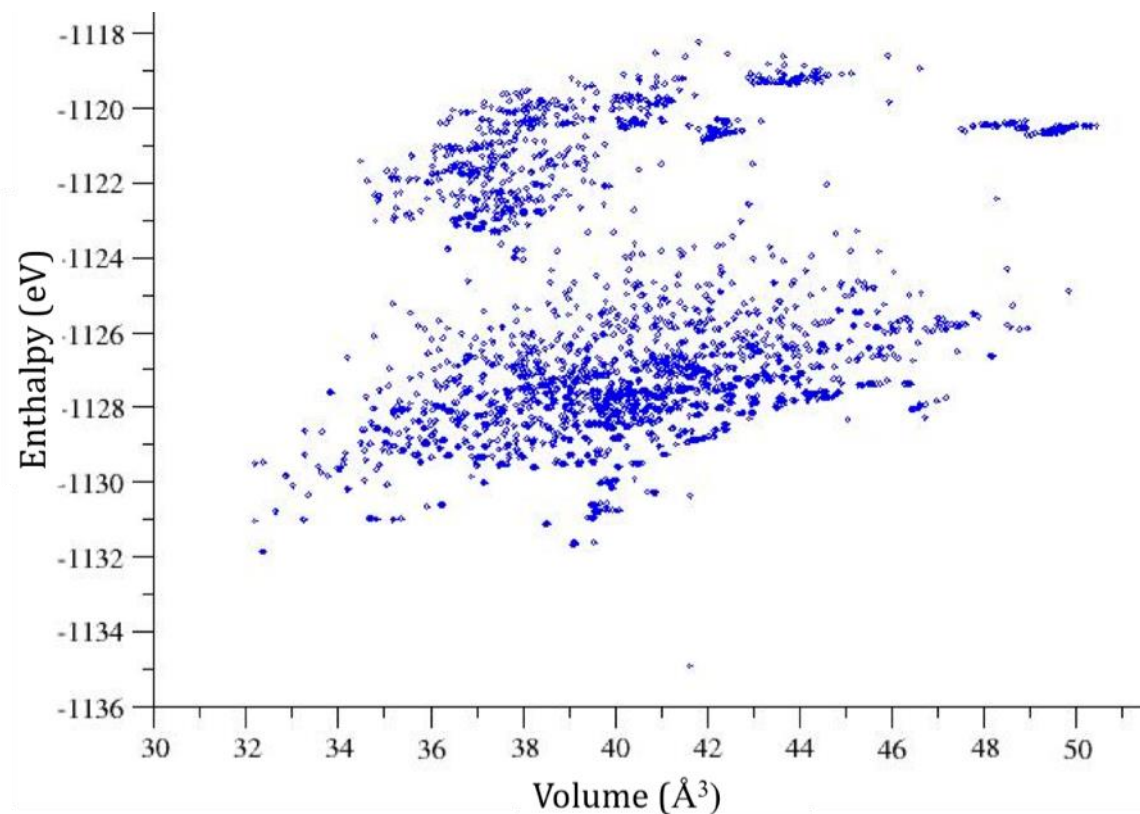
Figure 22: Energy Landscape for C_2N_3H, 1 Formula Unit at 25 GPa Random Search

At 25 GPa the AIRSS search provided a large number of non-crystalline structures, Figure 22 represents the energy landscape that was generated from the search. A selection of structures with a range of enthalpies and volume are represented in Table 8. The least stable structures formed largely molecular structures or C-N-H fragments, and were at -1124 eV or higher in energy.

The lowest energy structure (2252) was a 1D repeating chain and was more stable than the other structures by 3 eV. The defective-BN motif appeared again in 2D

arrangement (0075), although the stacking is less aligned than in the previous search, as there appears to be shearing between planes.

A slightly 'deformed' version of the defective wurtzite motif appeared in another low energy structure (5646), where the N-H bonded N atom appeared to make almost planar bonds with the adjacent C atoms, resulting in a larger volume of the unit cell.

The high-energy regions of the landscape predominantly formed fragments or molecular arrangements, often with C-C or N-N bonds dominating the configuration, as such these structures are not sampled in the table.
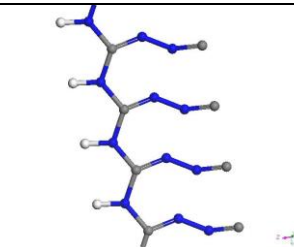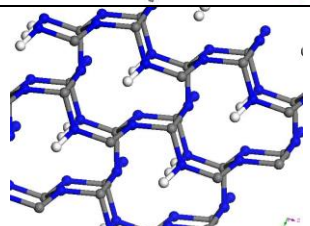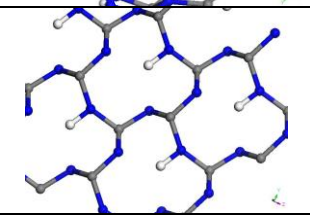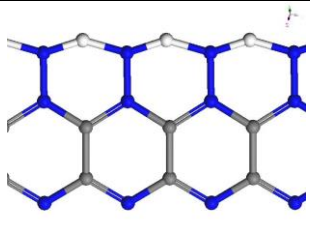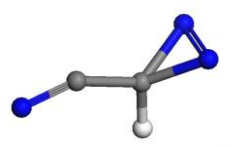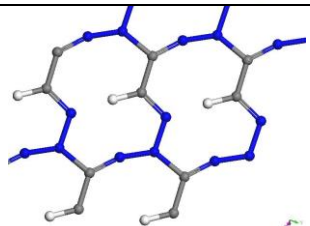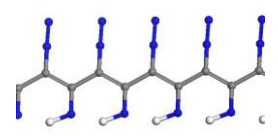
Structure Identifier and (Dimension)	Enthalpy (eV)	Volume (Å³)	Space Group	Structure Image
2252 (1D)	-1134.9	41.6	P1	
0075 (2D)	-1131.9	32.4	Cm	
5646 (2D)	-1131.0	33.3	Imm2	
3417 (2D)	-1129.5	32.2	P1	
1216 (Molecular)	-1124.9	49.8	Cm	
4068 (2D)	-1127.9	40.3	P1	
1422 (1D)	-1128.0	42.2	Cmcm	

Table 8: Structure details for C_2N_3H, 1 Formula Unit at 25 GPa Random Search

4.3.1.3 C_2N_3H, 1 Formula Unit, 50 GPa Random Search
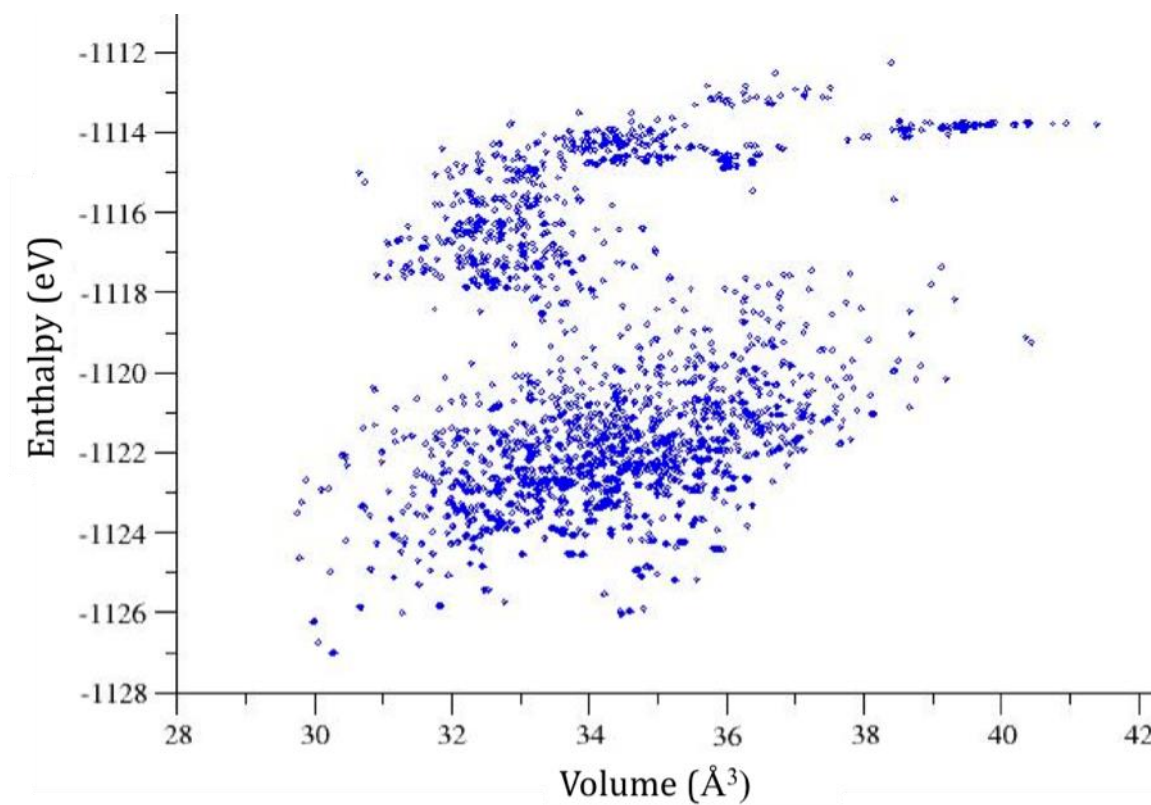
Figure 23: Energy Landscape for C_2N_3H, 1 Formula Unit at 50 GPa Random Search

At 50 GPa the AIRSS search provided a mixture of crystalline, molecular and chained structures presented in Table 9, with the least stable above -1118 eV that took the form of molecular fragments; the same pattern seen for the previous searches. The energy landscape for this search is presented in Figure 23.

The most stable structure was based on the defective-BN motif, the same low energy structure found in the previous searches; the structure was layered with AAA stacked planes, and Imm2 symmetry. A cluster of the same structure with Imm2 symmetry was found in the region of 29.5 to 30.3 Å and -1126 to -1127 eV.

Chained structures formed at approximately -1122 eV, with a large number forming C-C, N-N bonds, of which two examples are represented (8894 and 3931).

The search did not provide the experimentally known defective wurtzite structure, for this reason it was necessary to start applying constraints to the next search attempt. All further searches using 1 C_2N_3H formula unit were conducted at 75 GPa.
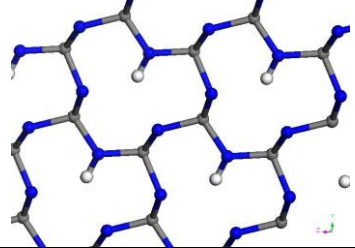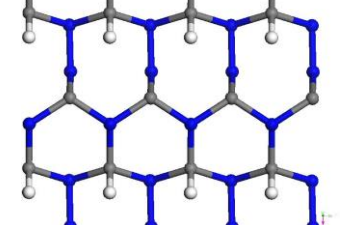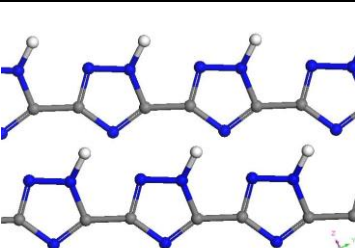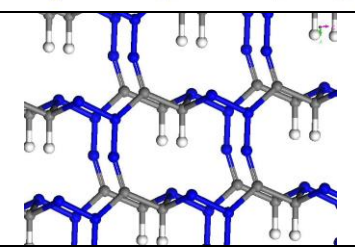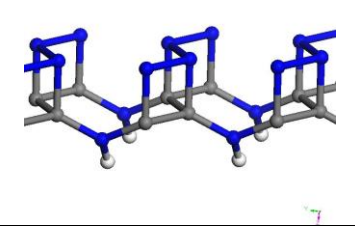
Structure Identifier and (Dimension)	Enthalpy (eV)	Volume (Å³)	Space Group	Structure Image
0972 (2D)	-1127.0	30.3	Imm2	
0928 (2D)	-1123.5	29.8	Pm	
8894 (1D)	-1113.8	41.4	P1	
3931 (1D)	-1124.4	35.9	P1	
5271 (3D)	-1122.7	34.3	P1	
7631 (2D)	-1122.7	32.8	Fmm2	

Table 9: Structure details for C$_2$N$_3$H, 1 Formula Unit at 50 GPa Random Search

4.3.1.4 C_2N_3H, 1 Formula Unit, 75 GPa Constrained Search, 0.5 Å Separation
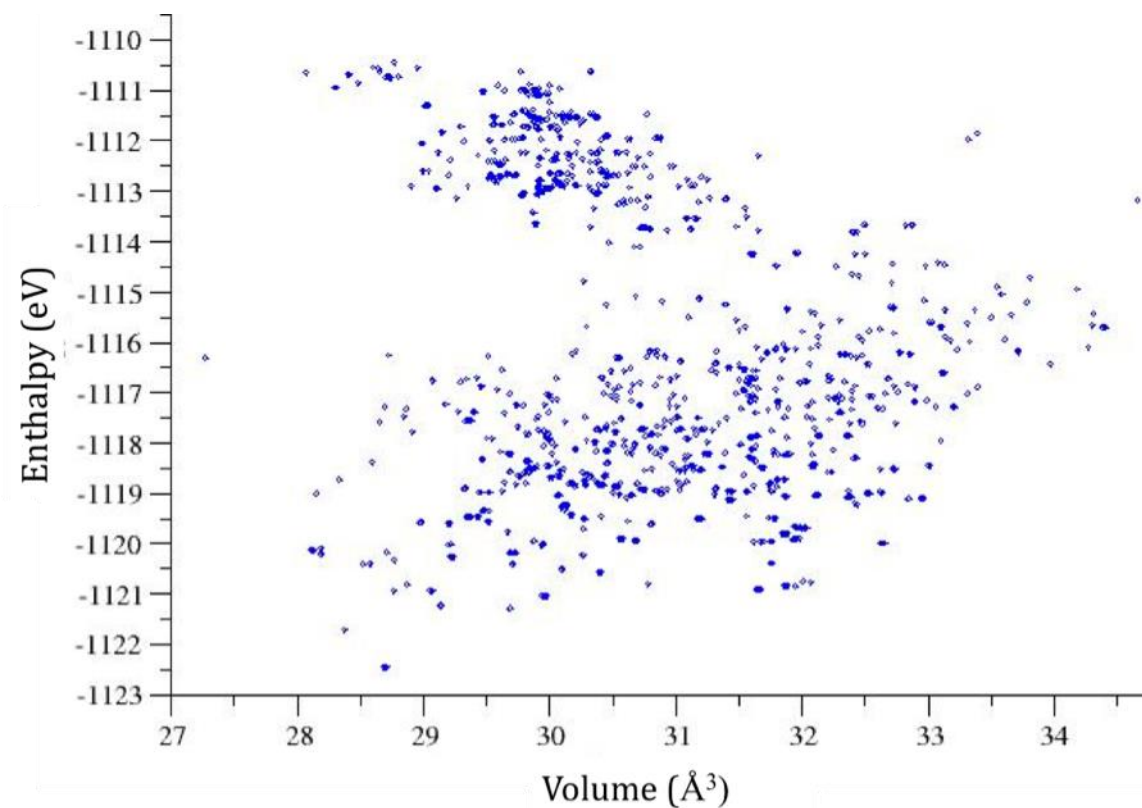
Figure 24: Energy Landscape for C_2N_3H, 1 Formula Unit at 75 GPa, 0.5Å Separation

At 75 GPa the minimum separation constraint was applied to the search, specifying a minimum distance of 0.5 Å between atoms. This would remove some of the 'nonsense' structures from the search, i.e. starting geometries where the atoms overlap in the randomised unit cell; these unit cells are disregarded by the AIRSS code, which maximizes use of computational time. Fewer structures were generated (~2000). The energy landscape is presented in Figure 24, and a selection of structures is presented in Table 10.

More crystalline structures were found from this search, and the lowest energy structure was the similar to that which was found in previous searches (1735), with

Imm2 symmetry. This time however, the structure was crystalline (3D) rather than graphitic (2D) in nature; the C atoms form single bonds to N atoms in the layers above and below. Another structure based on the same defective wurtzite motif was found in the low energy area of the energy landscape at -1121 eV (4953), with Cm space group, the bonds are strained when compared with the Imm2 structure, which provides a possible explanation for the higher energy calculated for this C-N arrangement.

The molecular structures and C-N-H fragments are found in the energy landscape at -1115 eV or higher. Crucially, the known C_2N_3H structure has eluded the search again; therefore another AIRSS search specifying minimum distance was attempted at 75 GPa.
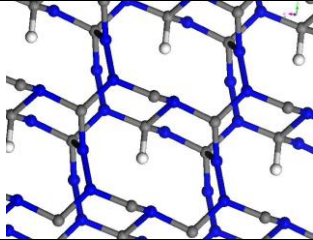
Structure Identifier and (Dimension)	Enthalpy (eV)	Volume (Å^3)	Space Group	Structure Image
1735 (3D)	-1122.5	28.7	Imm2	
5729 (3D)	-1121.2	29.1	P1	
4953 (2D)	-1120.9	31.7	Cm	
7062 (2D)	-1116.3	27.3	P1	
9774 (1D)	-1120.0	28.2	Fmm2	
0038 (1D)	-1118.2	30.8	P1	

Table 10: Structure details for C_2N_3H, 1 Formula Unit at 75 GPa, 0.5Å Separation

4.3.1.5 C_2N_3H, 1 Formula Unit, 75 GPa Constrained Search, 1 Å Separation
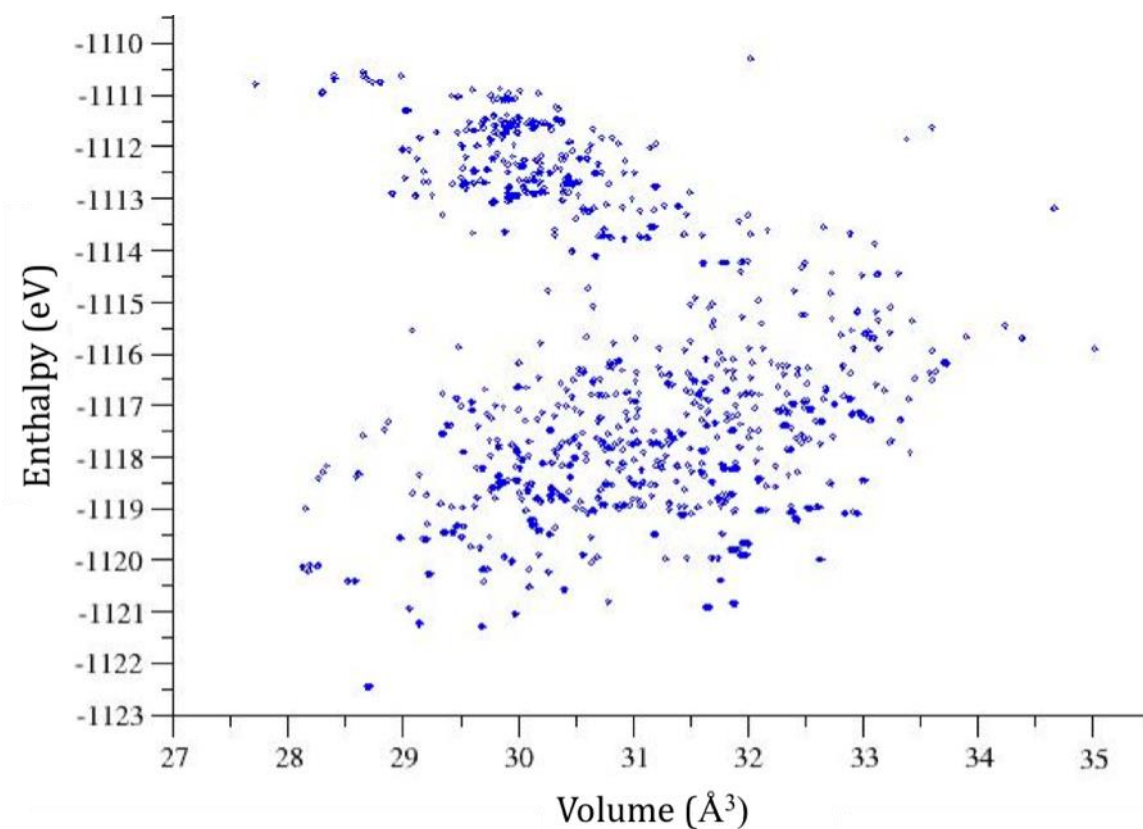
Figure 25: Energy Landscape at 75 GPa for C_2N_3H, 1 Formula Unit, 1Å Separation

Another constrained AIRSS search at 75 GPa, specifying the minimum separation between the atoms in the starting geometry was conducted, this time setting the distance to 1 Å. There were approximately 1000 structures generated in this search. The energy landscape is presented in Figure 25, and the corresponding structural details can be found in Table 11 for a selection of structures.

This search found the AAA stacked structure with Imm2 symmetry (4097) in crystalline form, and another structure with less symmetry, based on the same motif (3671).

The search still did not find the known defective wurtzite structure; although a number of alternating C-N bonded systems were located. Further constraints were applied in the following search, this time employing symmetry, which in effect would double the number of atoms in the unit cell. The unit cell for the C_2N_3H defective wurtzite structure requires 6 atoms, a requirement that the current set of searches fulfill. However, the $Cmc2_1$ space group has increased symmetry when compared to the Imm2 space group of the lowest energy structure found in all the AIRSS searches thus far. The defective wurtzite structure requires two unit cells for visualizing the structural form of the material. Hence, increasing the number of atoms, by applying a symmetry operation to the atoms in a unit cell with Imm2 as the starting configuration, allows for further flexibility in the arrangement. This increases the probability of finding the known defective wurtzite C_2N_3H material.
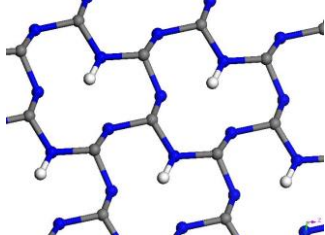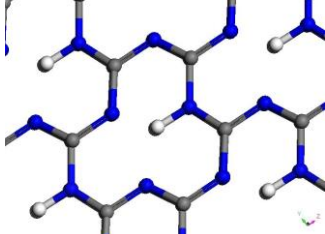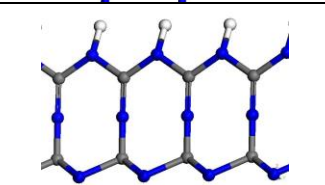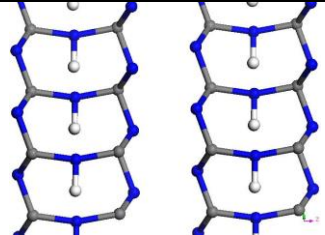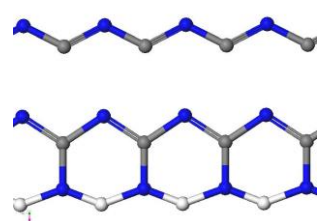
Structure Identifier and (Dimension)	Enthalpy (eV)	Volume (Å^3)	Space Group	Structure Image
4097 (3D)	-1122.5	28.7	Imm2	
3671 (3D)	-1121.0	30.0	P1	
0155 (1D)	-1120.0	29.9	Fmm2	
3115 (2D)	-1120.2	28.1	P3m1	
4869 (1D)	-1115.9	35.0	Pm	

Table 11: Structure details for C_2N_3H, 1 Formula Unit at 75 GPa, 1Å Separation

4.3.1.6 C$_2$N$_3$H, 1 Formula Unit – 75 GPa Constrained Search – 1x2 symmetry operation
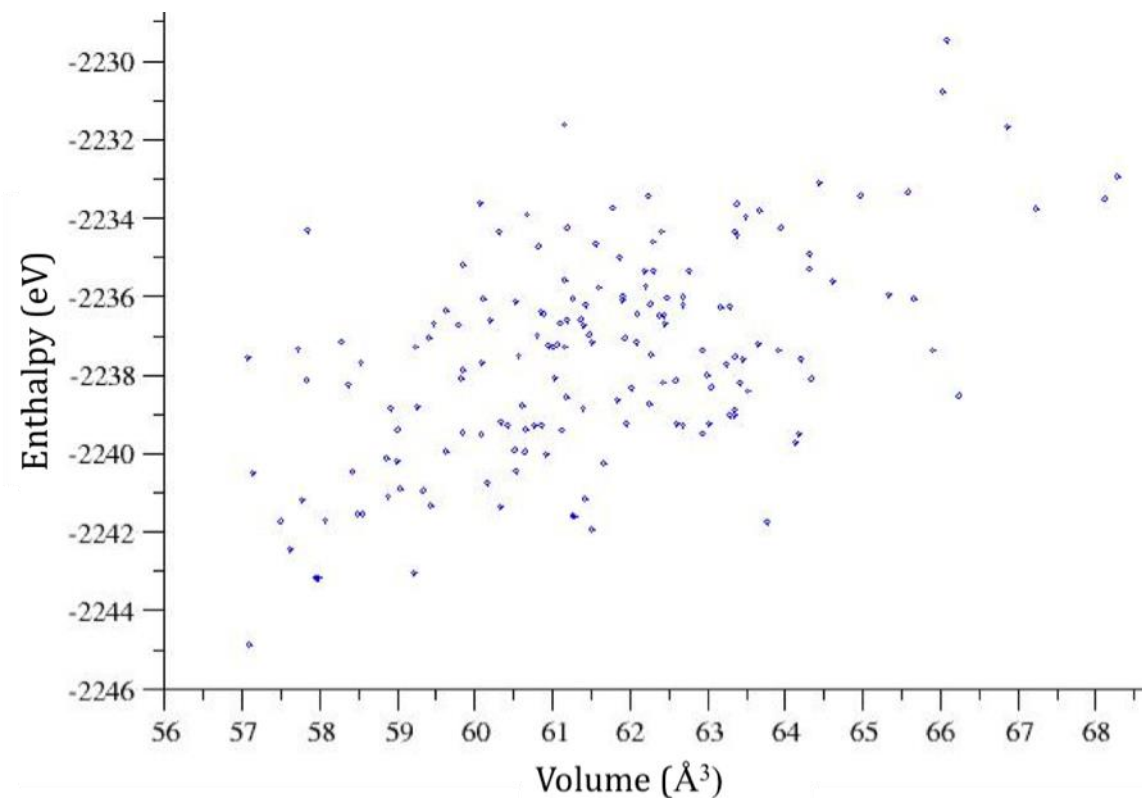
Figure 26: Energy Landscape for C$_2$N$_3$H at 75 GPa, 1x2 symmetry operation

Since the structure with Imm2 symmetry and AAA stacking was found in all the searches, we decided to employ the symmetry constraint, using this particular unit cell as the starting point for the AIRSS search; as mentioned previously the motif is related to the defective wurtzite structure.

The energy landscape is presented in Figure 26, and the corresponding structural details can be found in Table 12 (for a selection of structures).

At 75 GPa, the unit cell was specified with atomic coordinates of the Imm2 C_2N_3H arrangement and another symmetry operation was applied to the atoms within the unit cell, effectively doubling the number of atoms.

Many of the structures were crystalline or they formed chains. Despite having found a new low energy phase (7814) with the desired motif and a new space group (Cm), and an interesting 1D chain-like structure (6049), we did not locate the known defective wurtzite structure from this search.
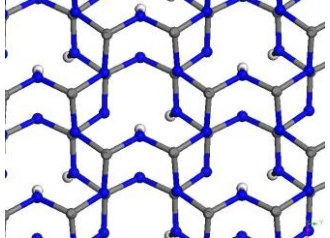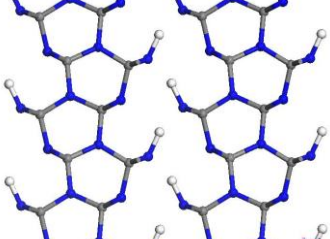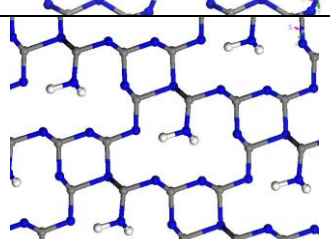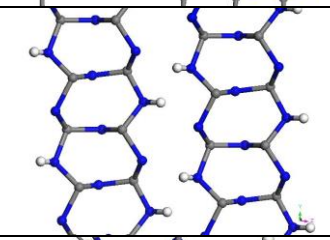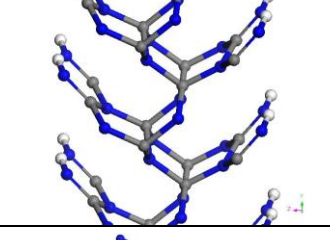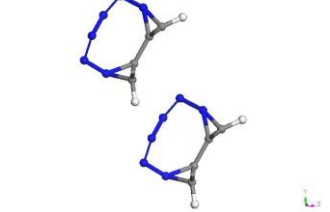
Structure Identifier and (Dimension)	Enthalpy (eV)	Volume (Å³)	Space Group	Structure Image
7814 (3D)	-2244.9	57.1	Cm	
6049 (1D)	-2243.2	58.0	Cc	
9324 (2D)	-2242.4	57.6	Cm	
5035 (1D)	-2241.7	57.5	P1	
30357 (1D)	-2241.6	61.3	Pmn21	
12460 (Molecular)	-2229.5	66.1	C2	

Table 12: Structure details for C$_2$N$_3$H, at 75 GPa 1x2 symmetry operation

4.3.1.7 C₂N₃H, 2 Formula Unit – 1 GPa Random Search
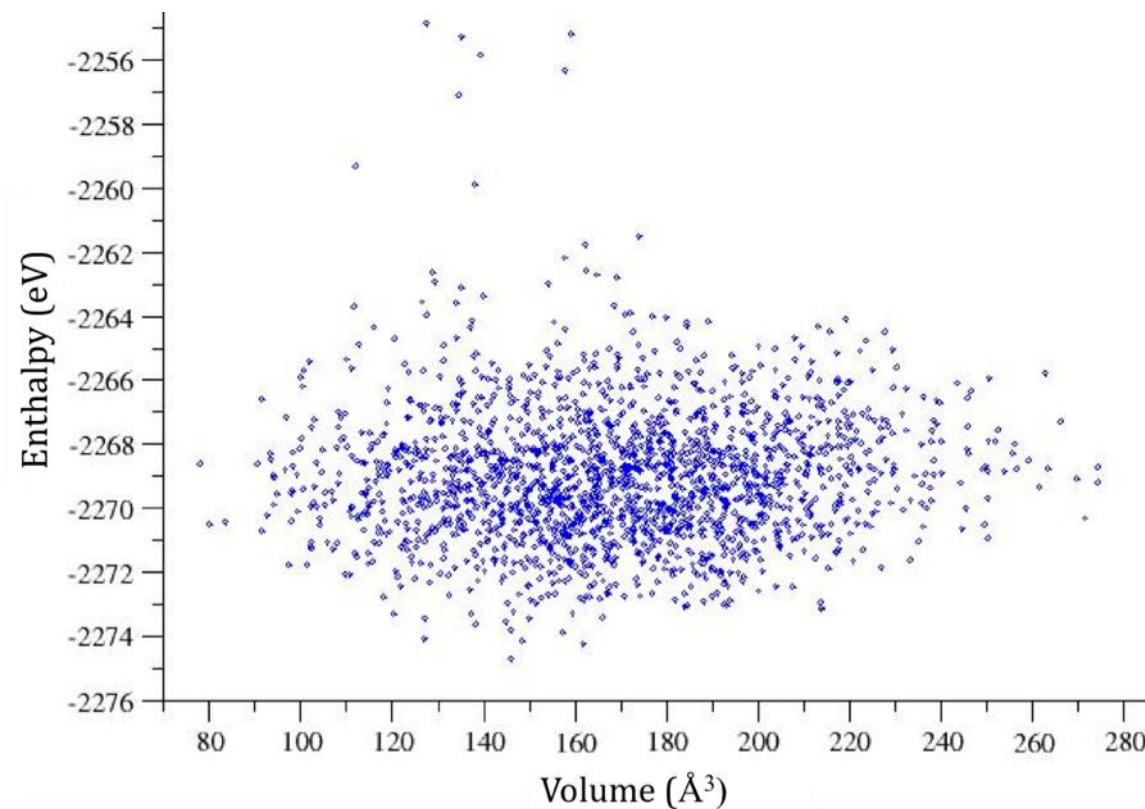
Figure 27: Energy Landscape for (C₂N₃H)x2 at 1 GPa Random Search

We carried out a series of searches with the stoichiometry $C_4N_6H_2$ without applying constraints to the AIRSS search. The energy landscape is presented in Figure 27, and the corresponding structural details can be found in Table 13 for a selection of structures. At 1 GPa the lowest energy structure was a layered phase with large voids, linked by pentane shaped rings consisting of 3N and 2C. A number of molecular and fragment arrangements were found above -2265 eV. Neither the Imm2 phase that had been found in the previous searches nor the defective wurtzite structure was located from this search.

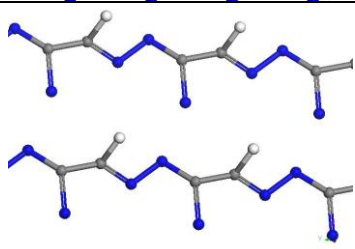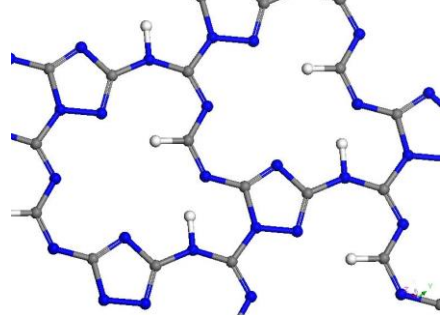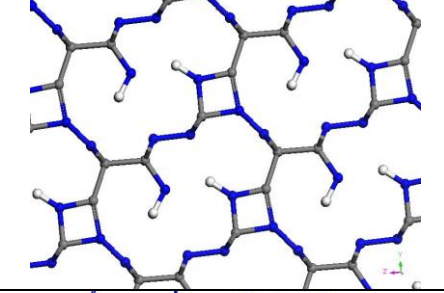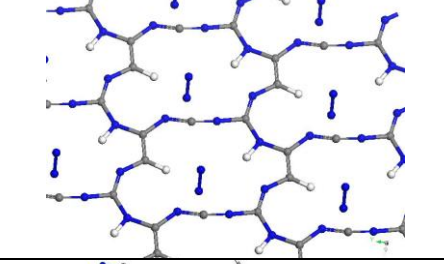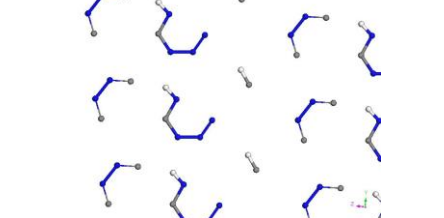| Structure Identifier and (Dimension)	Enthalpy (eV)	Volume (Å^3)	Space Group	Structure Image
7366 (2D)	-2274.7	146.0	P1	
1709 (2D)	-2268.6	77.9	Cm	
6665 (2D)	-2273.1	213.8	P1	
8261 (Molecular)	-2254.8	127.5	P1	

Table 13: Structure details for (C_2N_3H)x2 at 1 GPa Random Search

4.3.1.8 C_2N_3H, 2 Formula Unit – 25 GPa Random Search
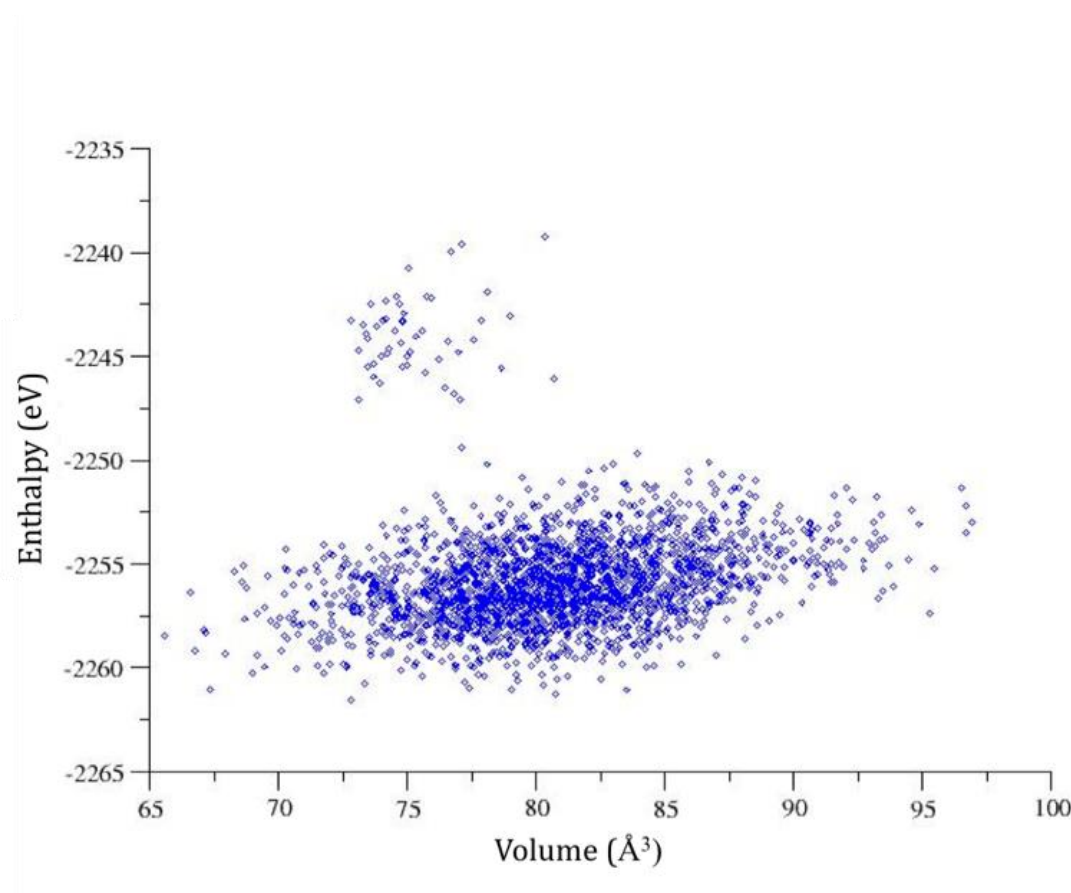
Figure 28: Energy Landscape for $(C_2N_3H)x2$ at 25 GPa Random Search

Another AIRSS search was conducted for two C_2N_3H formula units at 25 GPa, similar structures to those in the analogous search at 1 GPa were found (3986 and 3654). The energy landscape is presented in Figure 28, and the corresponding structural details can be found in Table 14 for a selection of structures.

A notable difference between 1 GPa and 25 GPa, the latter search found more structures in a 1D chain-like arrangement. Regions of molecular fragments were noticeable above -2250 eV. The known defective wurtzite structure was not located

in this search, and there was not a structure resembling the motif, unlike the previous searches, which only used half the number of atoms.
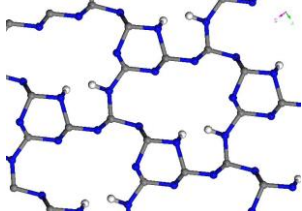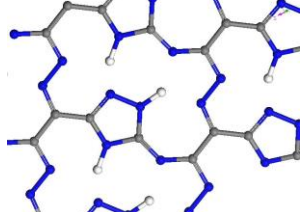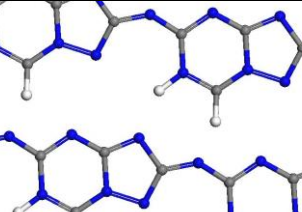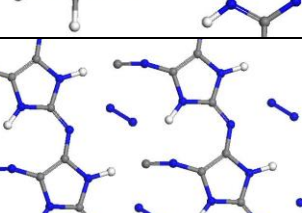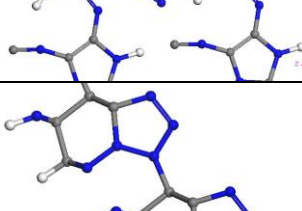
Structure Identifier and (Dimension)	Enthalpy (eV)	Volume (Å³)	Space Group	Structure Image
3986 (2D)	-2261.6	72.8	Pm	
3654 (2D)	-2261.3	80.8	P1	
3183 (1D)	-2261.1	83.5	P1	
9846 (1D)	-2258.0	88.6	P1	
4248 (1D)	-2258.0	70.8	C2/m	

Table 14: Structure details for (C$_2$N$_3$H)x2 at 25 GPa Random Search

4.3.1.9 C_2N_3H, 2 Formula Unit – 50 GPa Random Search
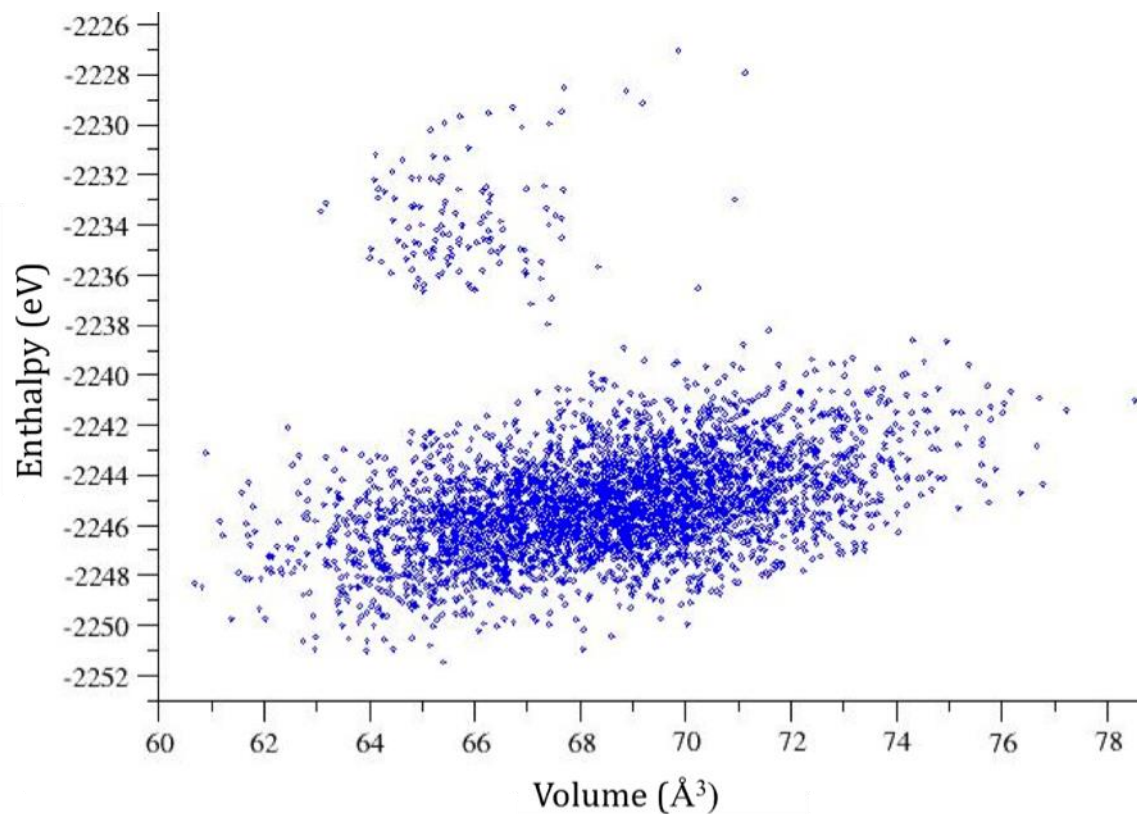
Figure 29: Energy Landscape for $(C_2N_3H)x2$ at 50 GPa Random Search

A final AIRSS search using $C_4N_6H_2$ atoms, at 50 GPa was attempted. The energy landscape is presented in Figure 29, and the corresponding structural details can be found in Table 15 for a selection of structures.

Interestingly the lowest energy structure was a chain-like formation (5457), with fully alternating C-N bonds with the H bonded to a N atom. The next structure that was lowest in energy (6333) was crystalline in arrangement, although there were C-C bonds present in the system. Similar structures were found as in the 1 GPa and 25

GPs searches (1161 and 5016). This search did not find the known phase or a structure resembling its motif. After the series of attempts, we decided that a constrained search, specifying the coordination of atoms was to be conducted at 75 GPa.
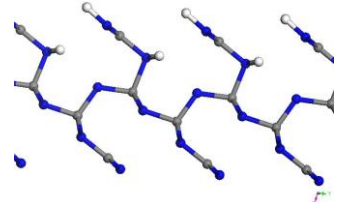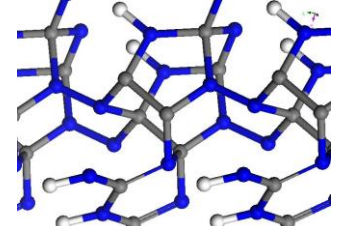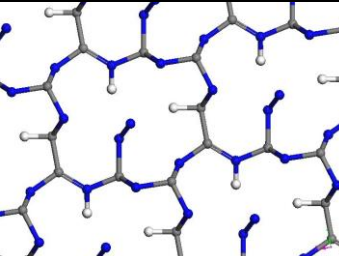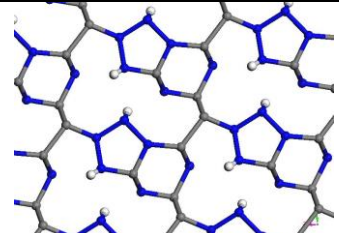
Structure Identifier and (Dimension)	Enthalpy (eV)	Volume (Å^3)	Space Group	Structure Image
5457 (1D)	-2251.5	65.4	P1	
6333 (3D)	-2251.0	63.9	C2/m	
1161 (2D)	-2249.7	65.1	Pm	
5016 (2D)	-2248.3	60.7	Pm	

Table 15: Structure details for (C$_2$N$_3$H)x2 at 50 GPa Random Search

4.3.1.10 C_2N_3H, 2 Formula Unit – 75 GPa Constrained Search – C 4 bonds, N 3 bonds
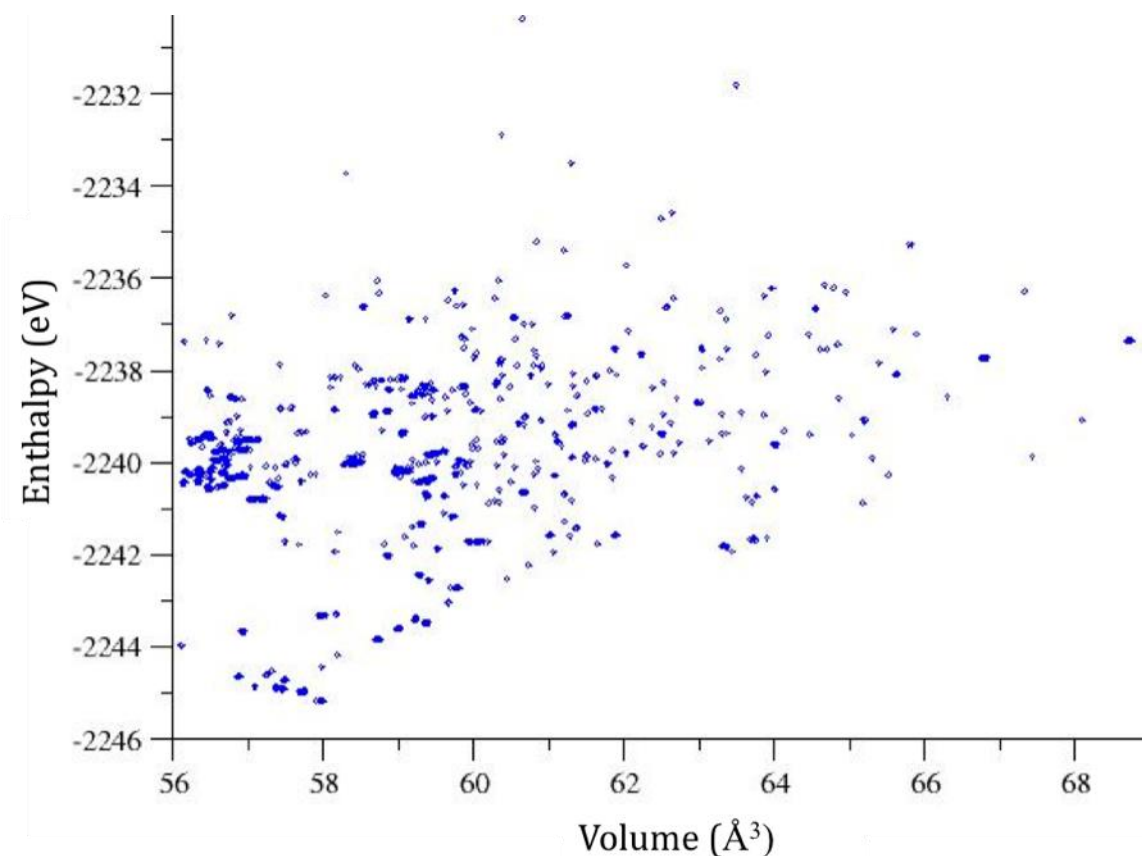
Figure 30: Energy Landscape for (C_2N_3H)x2, at 75 GPa constrained search C 4 bonds, N 3 bonds

We carried out an AIRSS search with extremely specific constraints at 75 GPa. Using two C_2N_3H formula units we specified that in the final structure C makes 4 bonds and the N makes 3 bonds. We also specified that C atoms only bond to N atoms, and H atoms only bond to the N. The lowest energy structure from the AIRSS constrained search at 75 GPa, was the known and experimentally obtained defective wurtzite structure, with $Cmc2_1$ space group; this structure was found within 10

minutes of starting this AIRSS search. The energy landscape is presented in Figure 30, a closer look at five selected low energy structures is presented in Figure 31, and the corresponding structural details are presented in Table 16.

When the energy landscape is compared with other AIRSS searches at 75 GPa, we find that many more structures are predicted in the low energy/small volume region i.e. bottom left of the landscape. This is the area where we expect to find a new dense C_2N_3H structure that may form during the synthesis of C_2N_3H defective wurtzite.

Since this constrained AIRSS search found the C_2N_3H structure, known to exist experimentally, a closer look at the newly predicted low energy structures in the landscape was necessary. The overall aim was to propose the structure for the metastable C_2N_3H phase that appeared to be present during the HPT synthesis of C_2N_3H defective wurtzite.

Five candidate structures were selected to investigate in more detail; a close up of the energy landscape is presented in Figure 31 and the defective wurtzite structure is outlined in red. One structure was found to exist in two distinct areas in the energy landscape, and one image has been used to represent this candidate (135cm and 969cm).
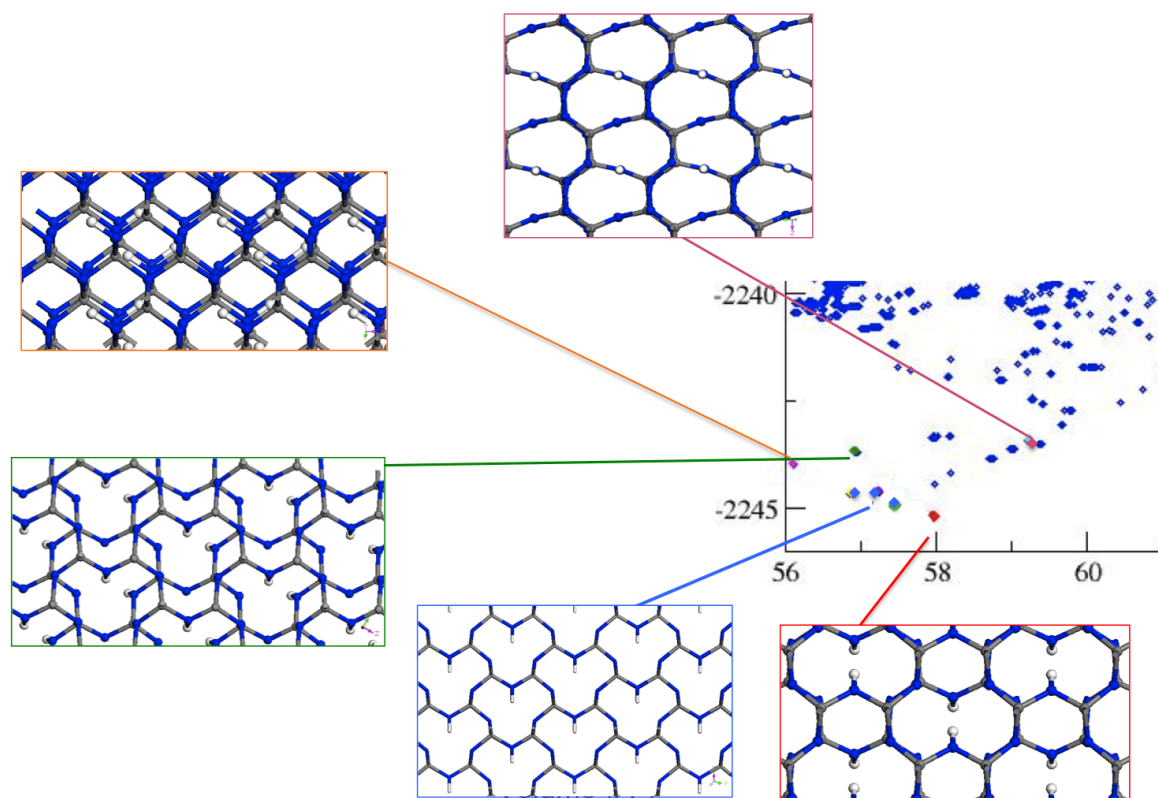
Figure 31: Structures selected for further investigation from the constrained search, specifying atom coordination at 75 GPa
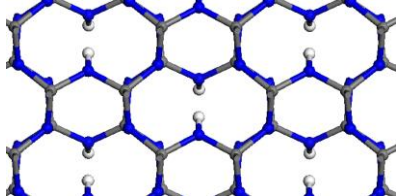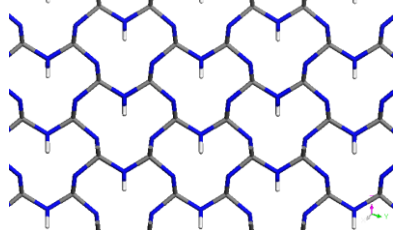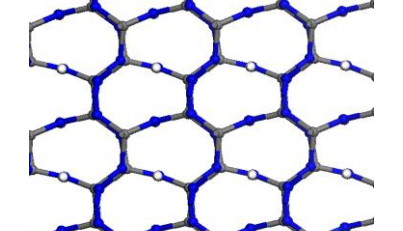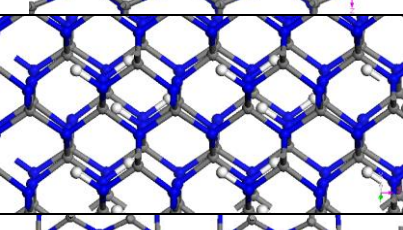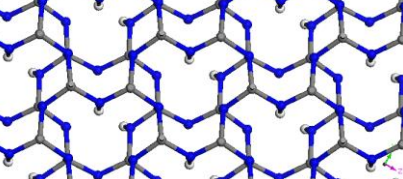
Structure Identifier	Energy (eV)	Volume (Å^3)	Space Group	Structure Image
cmc21	-2245.2	58.0	Cmc21	
808imm2	-2245.0	57.5	Imm2	
514aba2	-2243.4	59.2	Aba2	
104cc	-2244.7	57.5	Cc	
135cm & 969cm	-2244.7 -2244.9	56.9 57.1	Cm	

Table 16: Structure details for $(C_2N_3H)x2$, at 75 GPa constrained search C 4 bonds, N

3 bonds

The investigations into the candidate structures began with the calculation of the pressures at which these new structures would be more stable than the known phase, Table 17.

Structure Identifier	Transformation Pressure (GPa)
808imm2	72.8
514aba2	240
104cc	154
135cm	75.8
969cm	60.0

Table 17: Calculated pressures at which candidate structures are formed

The structure that is predicted to be more stable than the experimentally known defective wurtzite phase at the lowest pressure is 969cm, this structure is based on the same motif as defective wurtzite with an alternative stacking arrangement of the layers. The B layer is staggered compared to the layer above, by approximately $1/3$ of the unit cell. The next two structures that would be predicted to form at pressures 72.8 and 75.8 GPa are the 808imm2 and 135cm respectively, where they would be to be in equilibrium with the known phase at these pressures; during synthesis at high pressures these candidate structures may co-exist. The structures

that are predicted to be inaccessible by the HPT synthetic methods are 514aba2 and 104cc, where they are not predicted to form until pressures of 240 and 154 GPa respectively.

For each structure a full geometry optimization, in which all the atoms in the system were allowed to relax was carried out at a number of pressures between 0 – 60 GPa, as represented in Figure 32. The difference in energy between each predicted structure was compared to the known phase at each pressure.

The theoretical calculations showed that neither of the candidate structures was more stable than the known phase, up to 60 GPa. In fact if the trend line of the 808imm2 and 969cm structures were followed in Figure 32, we would not expect any crossing over in the most stable C_2N_3H arrangement until at least 100 GPa. The 514aba2 candidate was the only structure to become less stable with the increase in pressure; this structure had the least stable starting geometry from the constrained search. There was some crossover in stability between two structures (104cc and 969cm) at 40 GPa, however these were 0.6 eV less stable than the known defective wurtzite phase. These computational calculations are in contrast to the predicted transformation pressures using equation 4.3, which predict transformation between C_2N_3H phases starting from pressures of 60 GPa. The experimental observations show that the transformation begins at much lower pressures (~45 GPa).
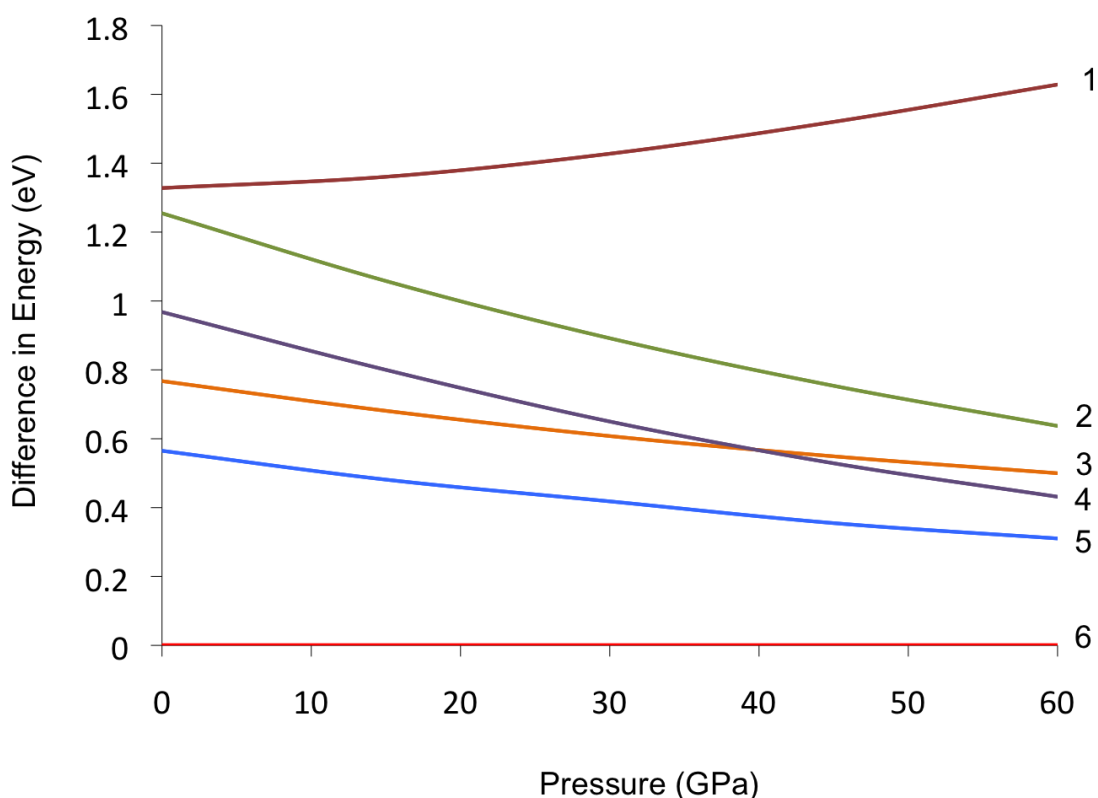
Figure 32: Difference in energy (eV) between candidate structures over a range of pressures (GPa) 1=514aba2, 2=135cm, 3=969cm, 4=104cc, 5=808imm2, 6=Defective Wurtzite

The next most stable configuration after the known defective wurtzite phase is the 808imm2 structure, which has consistently been found in the previous AIRSS searches (random or constrained) as the lowest energy candidate structure. The experimental pressures at which there was potentially a metastable phase present for the corresponding experimental XRD pattern was 45 GPa. In the theoretical calculations a range of pressures were specified pressure up to 75 GPa.

Using the optimized unit cell information and atomic coordinates for each candidate structure, the XRD patterns were generated. The d spacing peaks that disappeared

upon laser heating and could not be assigned to the defective wurtzite structure had values at ~3.3 Å and ~ 3.7 Å, represented in Figure 33. There was only one structure from the candidate selection that matched the region in which the XRD peaks for the metastable phase existed; 808imm2 had two d spacing peaks at 3.3 and 3.7 Å. The intensities (2:1) were found to be similar to those in the experimental pattern. The XRD patterns for the experimentally obtained metastable phase (highlighted with red arrows) and the theoretically predicted candidate C_2N_3H structures are represented in Figure 33.
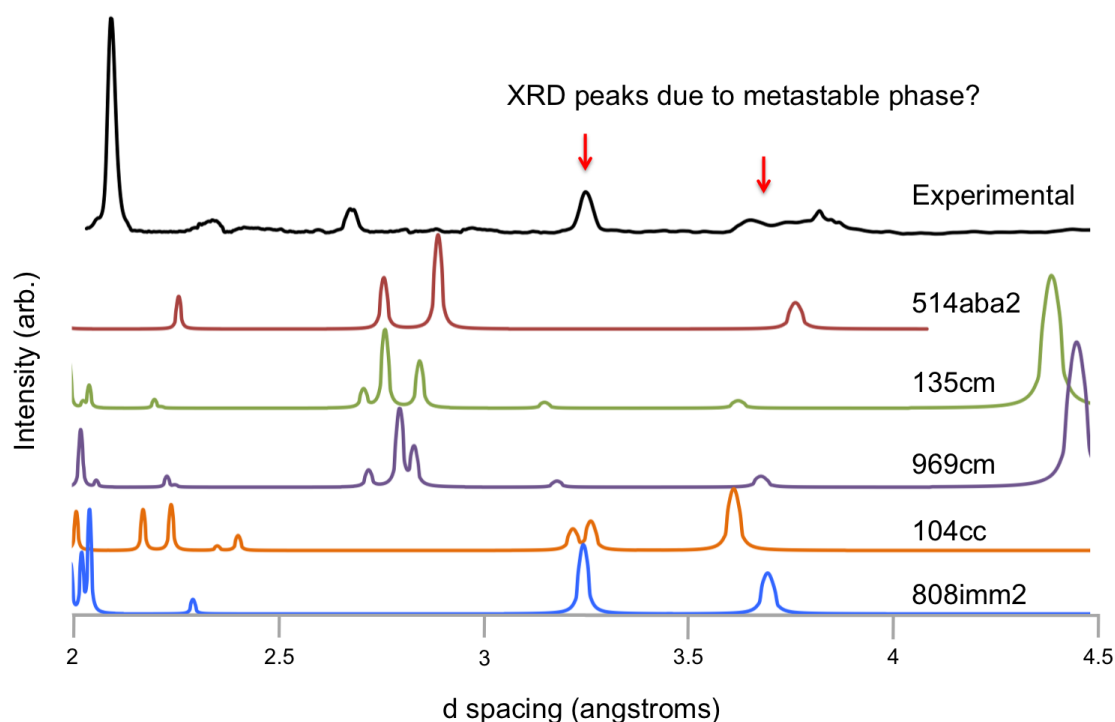
Figure 33: XRD patterns generated for the candidate structures from the AIRSS search, compared with experimental XRD pattern (black line) at 45 GPa

As mentioned previously the 808imm2 structure shares the same motif as the defective wurtzite, but the difference arises in the stacking arrangement; defective

wurtzite is ABA and 808imm2 is AAA. The 808imm2 structure is best described as defective-BN, where the defect is with the B site that is occupied by ⅔ C and ⅓ H atoms. Two possible explanations exist as to the presence of another phase; a stacking fault within the defective wurtzite structure where part of the framework could not align to be ABA stacked and was forced into AAA stacking, which is possible due to the nature of the DAC synthesis. Another possible explanation is the two phases co-exist at high pressures and both formed independently of one another during the synthesis, the 808imm2 structure is not sufficiently large to be stable and is only held in place by the pressures applied by the DAC. The laser heating resulted in a re-alignment of the bonds in favour of the most stable configuration of the two phases that are present.

Our theoretical calculations predict that the 808imm2 phase was less stable than the defective wurtzite phase by approximately 0.6 eV. In a situation where both phases are present we would predict that the defective wurtzite phase would be the favoured arrangement. After laser heating, the experimental XRD pattern showed the reflection at ~3.3 Å disappeared completely, whereas the reflection at ~3.7 Å was not as intense although was still present from the defective wurtzite structure. For the candidate structure 808imm2, the hkl values for the peaks at 3.7 and 3.3 Å are (1, -1, 0) and (0, 1, -1) respectively. During synthesis the pressure is applied along the z-axis in the DAC. The hkl values for the reflection at 3.3 Å may explain why the reflection and the phase disappears; compression takes place along the z-axis which may encourage AAA stacking, hence the reflection and therefore the metastable phase. However, once the sample is laser heated it causes the AAA

stacked layers to reconfigure (if there is a stacking fault) or disappear (if the phase is independent of the known phase).

4.4 Conclusion for C_2N_3H structure prediction to identify a metastable phase, using AIRSS

Structure prediction was employed to try and understand and explain an experimental problem. We propose to provide a structure profile with a consistent XRD pattern for the previously unidentified C_2N_3H metastable phase, which was reported to be present during the HPT DAC synthesis, using the AIRSS structure prediction method.

To search the C-N-H energy landscape the AIRSS method was employed to find a new C_2N_3H phase over a range of pressures (1 – 75 GPa), for 1 and 2 formula units. When the truly random searches did not find the known phase, a number of constraints were applied. These included specifying a minimum separation distance between atoms, applying symmetry operations to an initial starting geometry and specifying the coordination of atoms within the unit system. A general picture of the structural regions in the energy landscape emerged and is presented in Figure 34. Although the odd anomaly may exist and be found in other regions of the landscape, more than 95 % of the structures surveyed, fit in the areas specified in the figure. The AIRSS method located the known phase only when coordinated constraints were applied, after which the known phase was located with 10 minutes of the search commencing. The AIRSS method proved to be extremely effective at providing a range of different C-N structures, however the

useful and sought after C-N and N-H bonded structures were only found in abundance, when precisely specified at the beginning of the search.
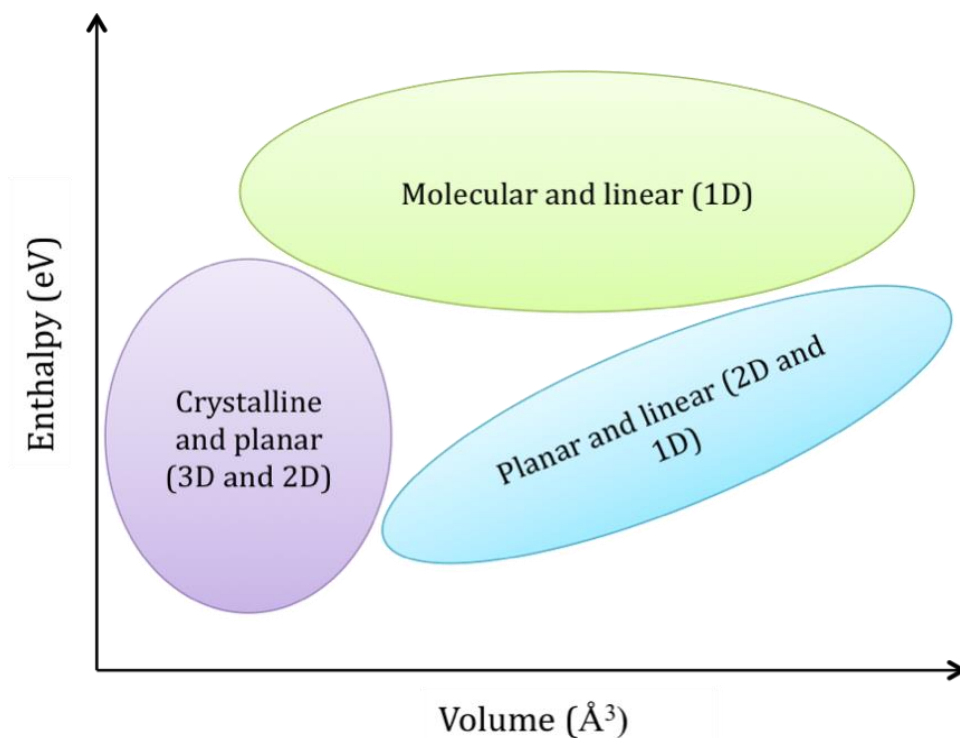
Figure 34: Regions where Crystalline, Planar, Linear and Molecular structures can expected to be found, in the energy landscape from the AIRSS searches

All AIRSS searches using 1 formula unit found a low energy phase with Imm2 symmetry that was based on the same motif as the defective wurtzite structure, differing by AAA stacking arrangement to give a defective-BN structure (with the B site occupied by ⅔ C and ⅓ H atoms). The experimentally known phase was found from a search that specified the C and H bonded to N, and the C and N atoms made 4 and 3 bonds respectively.

Neither of the searches predicted a structure to be more stable than the experimentally known phase. However, the next most stable arrangement after the known defective wurtzite structure was the candidate with Imm2 symmetry. This structure was found repeatedly in the AIRSS searches.

Simulated XRD patterns for the Imm2 candidate structure produced an XRD pattern that agreed with the previously unassigned reflections at ~3.3 and ~3.7 Å, which disappeared upon laser heating experiments. We propose from the AIRSS searches that the Imm2 phase is the most plausible explanation for the existence of a metastable phase, the structure shares the same motif as the existing C_2N_3H structure. This proposition is supported by the experimentally available XRD pattern and the common motif shared by both structures.

Chapter 5

Calculated NMR Chemical Shifts for Carbon Nitride Structures

5.1 Introduction

The use of NMR techniques has previously been discussed in Chapter 2. In the field of carbon nitrides this method was key to the structure elucidation of Liebig's 'melon'. In this part of the thesis, the NMR method has been employed to better understand atom connectivity of synthesized C-N materials, theoretically and experimentally. Information on the presence or absence of N-H species and triazine ring units can be gained using vibrational spectroscopy. These methods however, are limited to the types of bonds present, rather than topology and structure determination. The primary characterization technique that can lead to understanding the linkage within C-N structures, as a function of the preparation conditions, is solid-state ^{13}C and ^{15}N NMR spectroscopy.

It is necessary to begin with an investigation of computational NMR chemical shifts and a comparison with known experimental results, for determining the reliability of the predicted calculations. The comparison has been performed on a set of chemical shifts for known materials reported in the literature for both C and N.

This allowed for determination of accurate assignments of NMR chemical shifts for C-N structures as a function of their atomic environments. The determination and subsequent use of a scaling factor (to correct for systematic errors in the calculated chemical shifts) allowed for better-predicted theoretical results.

The NMR chemical shifts were then predicted for a commonly used starting material for C-N synthesis; triazine, as well as the structurally related motif present in the C-N structures; heptazine. Predictions were also made using this method for heptazine agglomerates, and the results have been presented in this thesis for the first time.

5.2 Scaling Calculated NMR Chemical Shifts with Experimental Values

A series of theoretical calculations were completed on structures or molecules where the experimental NMR chemical shift was already reported in the literature [102-104]. Specifically, structures with C-N bonds present within the system were modeled, as these were most relevant to this study. A complete list can be found in Tables 18 and 20 for ^{13}C and ^{15}N respectively. The structure that was used for referencing the carbon chemical shifts was tetramethylsilane (TMS), and nitromethane (CH_3NO_2) was used for referencing the nitrogen chemical shifts; the reference structures were fully optimized. The optimized geometries were then used in NMR shielding calculations using the "gauge including projector augmented-wave" (GIPAW) method available in CASTEP [96-98].

All molecular structures investigated were constructed using Materials Studio [105], for determining the atomic coordinates within the unit cell for generation of the 'cell' file. The structure was optimized using the CASTEP code, under periodic boundary conditions and using large unit cells where periodic images of the molecule are separated by a large enough vacuum to ensure that intermolecular interactions are negligible. All calculations used the PBE exchange correlation functional [106], with ultrasoft pseudopotentials [107] for each atom, and all atoms in the structure were allowed to relax.

A number of molecular systems were modeled, which were all optimized in varying unit cell sizes, to be certain that there was minimal electron interference between the periodic images in the neighboring unit cells. A suitable unit cell size for each structure was chosen on the basis of the lowest energy. The smallest unit cell suitable for modeling molecular structures was $(6 \text{ Å})^3$, and for larger structures the ideal size was between $(10 \text{ Å})^3$ and $(20 \text{ Å})^3$.

The k-point spacing was tested on all structures between 0.01 and 1 Å^{-1}, with the final calculations reaching a suitable convergence with k-point spacing set at 0.03 Å^{-1}. The energy cut off was also tested between the range of 400 to 900 eV, with the calculations reaching suitable convergence at 700 eV. These parameters (k-point spacing at 0.03 Å^{-1} and cut of energy at 700 eV) gave suitable ground state results for all structures, when compared with calculations that used finer parameters (higher cut off and finer k-point spacing).

The optimized geometries for the structures were then directly used in NMR shielding calculations. The calculated isotropic shielding parameters (σ_{iso}) were subtracted from the isotropic shielding value calculated for the reference compounds, for conversion into calculated chemical shifts (δ_{iso}). These values were applied to equation 2.9, to generate a series of chemical shift values for the C-N structures modeled. The output file generated by the CASTEP code listed the predicted isotropic magnetic shielding values for all the atoms present (C, N, H) in a single calculation. This meant in the case of carbon nitrides, it was not necessary to re-calculate the NMR isotropic shielding values for both the atoms of interest (^{13}C or ^{15}N).

5.2.1 Scaling ^{13}C NMR Chemical Shifts

The calculated ^{13}C NMR isotropic magnetic shielding (σ_{iso_calc}, in ppm) for each C-containing molecules examined, is reported in Table 18 together with the experimental values (σ_{iso}, in ppm) obtained from the literature.

Molecule	Cell Size (Å)^3	Isotropic Magnetic Shielding	
		Experimental (σ_{iso}, ppm)	CASTEP ($\sigma_{iso.calc}$, ppm)
CH_4	6	195.1	186.3
C_2H_2	6	117.2	104.3
C_2H_4	6	64.5	43.6
C_2H_6	6	180.9	173.8
C_6H_6	12	57.2	39.8
CH_3OH	6	136.6	119.8
HCN	6	82.1	55.5
$\underline{C}H_3CN$	6	187.7	174.9
$CH_3\underline{C}N$	6	73.8	43.7
CH_3NH_2	6	158.3	145.2
H_2CN_2	6	164.5	151.8
TMS*	**10**	**188.1**	**178.2**
$C_6N_{10}H_6$	10	165	175
$C_6N_{10}H_6$	10	156	167
$C_3N_6H_6$	10	168	176
*TMS = reference structure for ^{13}C atoms $NB:$ for structures where more than one C atom is present, the chemical shift for the corresponding C atom is denoted as $\underline{\textbf{C}}$			

Table 18: Experimental and theoretical isotropic ^{13}C NMR magnetic shielding in ppm

The isotropic magnetic shielding value for each structure was subtracted from the value obtained for the TMS reference, to determine the chemical shift, δ_{iso} in ppm. Experimentally the reference isotropic magnetic shielding value was 188.1 ppm and theoretically this was calculated to be 178.2 ppm. A full set of chemical shifts for the structures under investigation can be found in Table 19.

A comparison between the experimental and theoretical δ_{iso}, Figure 35, shows that the calculated values correlate well with the experiment and hence can be used for assignments of chemical shifts for unknown structures. However, the error is not uniform and the higher chemical shift values (above 120 ppm) are further away from the expected experimental values, deviating by as much as 20 ppm for $CH_3\underline{C}N$. The lower chemical shift values (below 80 ppm) deviate from the experimental results by 8 ppm or less. The correspondence between calculated and experimental shifts can be improved by scaling. The calculated $\delta_{iso.calc}$ data points were plotted, which allowed for the line of best fit and scaling formula to be obtained, represented as the blue line in Figure 35.

The scaling formula obtained for the ^{13}C chemical shift as shown in equation 5.1, allowed for better correspondence to the experimental results compared with the calculations; the scaled chemical shift values are represented on the same graph as the non-scaled values, in Figure 35, where a clear improvement in the chemical shifts is evident.

$$\delta_{scaled} = 0.9295\,\delta_{iso.calc} - 0.8771$$

(5.1)

The calculated δ_{scaled} values obtained using equation 5.1, are reported in Table 19.
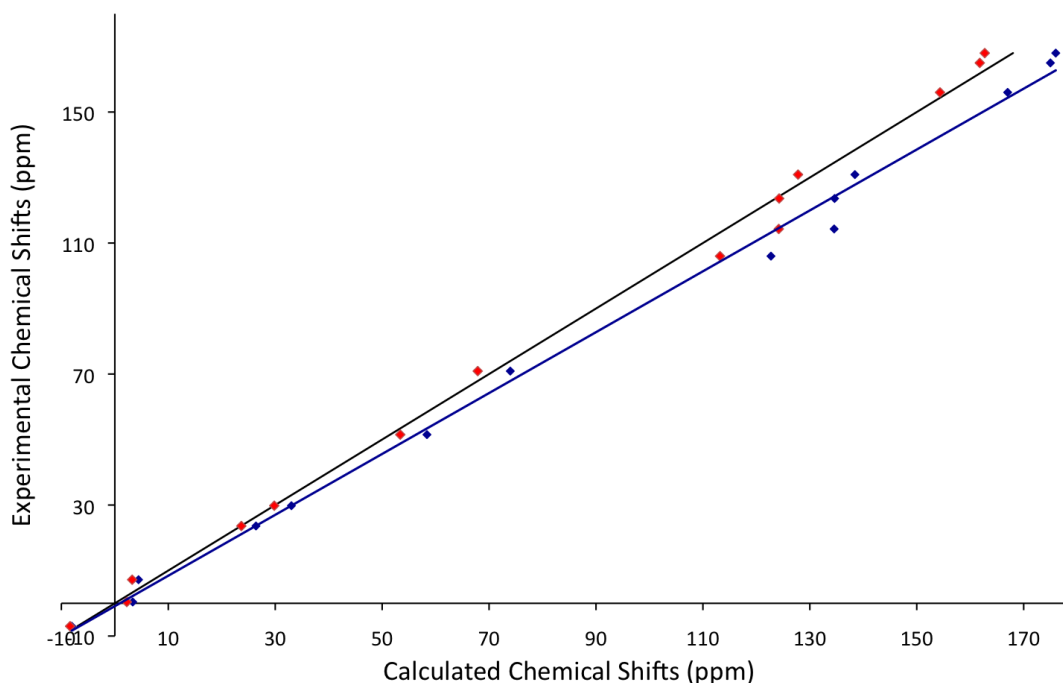
Figure 35: Graph that shows the linear correlation between experimental and theoretical ^{13}C NMR chemical shifts. The line of best fit (blue line) is used to determine the scaling formula from the predicted chemical shifts (blue); scaled values are represented in red

The results show the initial calculated ^{13}C NMR chemical shifts are improved by linear scaling, the R^2 value is calculated to be 0.996. The average was calculated by summing the modulus of the difference between experimental and calculated chemical shifts, before dividing by the total number of molecules investigated. Comparison with experimental chemical shifts, before and after scaling show improvement of more than 50%, from 7.7 to 3.1 ppm.

The largest deviation is observed for the cyano C in CH_3CN, and this value improved from 20 ppm deviation to 10 ppm deviation, in the rescaled results, when compared with the experimental data set.

Molecule	Referenced to TMS	Referenced to TMS	Difference Between Experimental and CASTEP	Referenced to TMS and Scaling Formula Applied	Difference Between Experimental and CASTEP
	Experimental (δ_{iso}, ppm)	CASTEP ($\delta_{iso.calc}$, ppm)	$\|\delta_{iso.calc}\text{-}\delta_{iso}\|$	CASTEP (δ_{scaled}, ppm)	$\|\delta_{scaled}\text{-}\delta_{iso}\|$
CH_4	-7.0	-8.1	1.1	-8.4	1.4
C_2H_2	70.9	74.0	3.1	67.9	3.0
C_2H_4	123.6	134.6	11.0	124.3	0.7
C_2H_6	7.2	4.4	2.8	3.2	4.0
C_6H_6	130.9	138.4	7.5	127.8	3.1
CH_3OH	51.5	58.4	6.9	53.4	1.9
HCN	106.0	122.7	16.7	113.2	7.2
$\underline{C}H_3CN$	0.4	3.4	3.0	2.2	1.8
$CH_3\underline{C}N$	114.3	134.6	20.3	124.2	9.9
CH_3NH_2	29.8	33.0	3.2	29.8	0
H_2CN_2	23.6	26.4	2.8	23.7	0.1
$C_6N_{10}H_6$	165.0	175.0	10.0	161.8	3.2
$C_6N_{10}H_6$	156.0	167.0	11.0	154.3	1.7
$C_3N_6H_6$	168.0	176.0	8.0	162.7	5.3
NB: for structures where more than one C atom is present, the chemical shift for the corresponding C atom is denoted as $\underline{\textbf{C}}$					

Table 19: Experimental and theoretical isotropic ^{13}C NMR chemical shift (δ), theoretical results before and after scaling

The improvement in the chemical shift values allows for confidence in our theoretically predicted ^{13}C NMR results, when using the CASTEP code to model new C-N structures. Predictions are especially useful for compounds whose structure is unknown and reference NMR data is not available in the literature.

5.2.2 Scaling ^{15}N NMR Chemical Shifts

The calculated ^{15}N NMR chemical shifts were compared and referenced with experimental results, in a similar way to the ^{13}C NMR results. The ^{15}N NMR chemical shifts listed in Table 20 are referenced to nitromethane. The calculated ^{15}N isotropic magnetic shielding for nitromethane, is calculated to be -166.5 ppm. The calculated ^{15}N chemical shift values are generally within 4% error to the experimental values. As with the ^{13}C chemical shift values the correspondence between experiment and theory can be improved by scaling. The predicted results are compared with the experimentally known values in Figure 36, where the line of best fit and scaling formula are derived. The results show the initial calculated chemical shifts were improved by linear scaling, the R^2 value at 0.996 showed there to be a good model fit.

Molecule	Cell Size $(\text{Å})^3$	Referenced to nitromethane	Isotropic Magnetic Shielding	Referenced to nitromethane	Difference Between Experimental and CASTEP
		Experimental (δ_{iso}, ppm)	CASTEP ($\sigma_{iso.calc}$, ppm)	CASTEP ($\delta_{iso.calc}$, ppm)	$|\delta_{iso.calc}\text{-}\delta_{iso}|$
NH_3	6	-380	248.6	-415.1	35.1
$CH_3CH_2NHCH_3$	8	-352	192.7	-359.2	7.2
CH_3NHCH_3	8	-369	214.6	-381.1	12.1
NH_4Cl	6	-352	200.3	-366.7	14.7
$(CH_3)_2\underline{\mathbf{N}}\text{-}N\text{=}CHCH_3$	8	-279.8	106.5	-273	6.3
$(CH_3)_2N\text{-}\underline{\mathbf{N}}\text{=}CHCH_3$	8	-24.4	-139.9	-26.6	2.2
$s\text{-}C_3N_6H_3$	6	-98.5	-76	-90.5	8.0
C_5H_5N	6	-63.2	-110.6	-55.9	7.3
C_4N_2H4 *ortho*	6	20.2	-209	42.5	22.3
$C_4N_2H_4$ *meta*	6	-84.5	-93.4	-73.1	11.4
$C_4N_2H_4$ *para*	6	-46.1	-128.6	-37.9	8.2
$C_4N_2H_4O$ [1]	6	-55.1	-111	-55.5	0.4
$C_4N_2H_4O$ [2]	6	-33.8	-143	-23.5	10.3
$C_5N_2H_6$ [3]	6	19	-220	53.5	34.5
$C_5N_2H_6$ [4]	6	15.1	-215	48.5	33.4
$C_6N_{10}H_6$*	10	-295	140.8	-307.3	12.3
$C_6N_{10}H_6$*	10	-207	24.3	-190.8	16.2
$C_6N_{10}H_6$*	10	-234	65.1	-231.6	2.4
$C_3N_6H_6$*	10	-275	156.4	-322.8	47.8
$C_3N_6H_6$*	10	-200	45.5	-212	12.0

[1] Aromatic N not attached to O atom. [2] Aromatic N attached to the O atom
[3] Aromatic N adjacent to hydrogenated C. [4] Aromatic N adjacent to methlyated C
* Melamine/Heptazine adducts not used in the scaling graph, Figures 30-33 pictorially represent the different chemical shifts for these molecules

Table 20: Experimental ^{15}N NMR chemical shift (δ) and theoretical ^{15}N isotropic

magnetic shielding (σ) and the corresponding calculated chemical shift
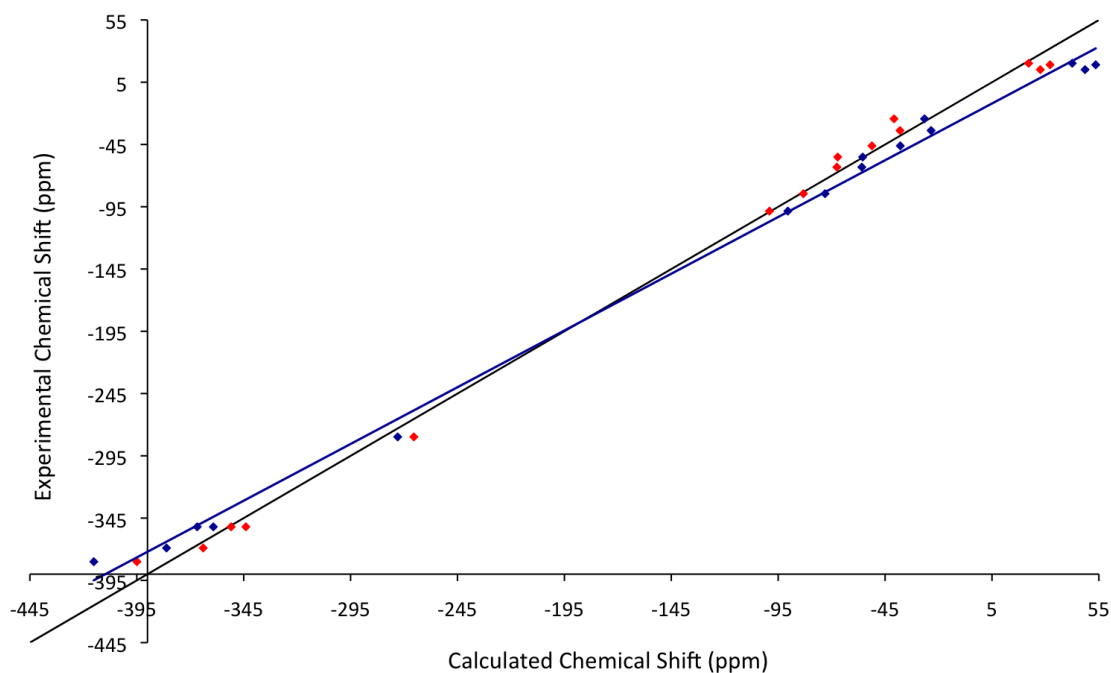
Figure 36: Graph that shows the linear correlation between experimental and theoretical ^{15}N NMR chemical shifts. The line of best fit (blue line) is used to determine the scaling formula from the predicted chemical shifts (blue), scaled values are represented in red

The scaling formula obtained for the ^{15}N NMR chemical shift is represented in equation 5.2.

$$\delta_{scaled} = 0.9114\,\delta_{iso.calc} - 16.6130$$

(5.2)

The formula obtained from the line of best fit was used to re-calculate the theoretical ^{15}N NMR shifts, and we can see from Figure 36, the scaled results (red dots) are closer to the experimental line than the initial theoretical values (blue

dots). The full data set with the scaled theoretical chemical shifts is presented in Table 21. The average deviation between experiment and theory was calculated to be 9.2 ppm, an improvement from 15.2 ppm for the non-scaled CASTEP calculations.

For prediction of ^{15}N NMR chemical shifts we can therefore confidently use the CASTEP code. Reliable predictions about the local environment for the nitrogen atoms in C-N structures can be made, which allows for elucidation of atom connectivity, hence structure determination.

Molecule	Referenced to Nitromethane	Referenced to Nitromethane and Scaling Formula Applied	Difference Between Experimental and CASTEP
	Experimental (δ_{iso}, ppm)	CASTEP (δ_{scaled}, ppm)	$\|\delta_{scaled} - \delta_{iso}\|$
NH_3	-380	-394.9	14.9
$CH_3CH_2NHCH_3$	-352	-344	8.0
CH_3NHCH_3	-369	-363.9	5.1
NH_4Cl	-352	-350.9	1.1
$(CH_3)_2\mathbf{N}$-N=CHCH_3	-279.8	-265.4	14.4
$(CH_3)_2N$-$\mathbf{N}$=CHCH_3	-24.4	-40.8	16.4
s-$C_3N_6H_3$	-98.5	-99.1	0.6
C_5H_5N	-63.2	-67.5	4.3
C_4N_2H4 ortho	20.2	22.1	1.9
$C_4N_2H_4$ meta	-84.5	-83.2	1.3
$C_4N_2H_4$ para	-46.1	-51.1	5.0
$C_4N_2H_4O$ [1]	-55.1	-67.1	12.0
$C_4N_2H_4O$ [2]	-33.8	-38	4.2
$C_5N_2H_6$ [3]	19	32.2	13.2
$C_5N_2H_6$ [4]	15.1	27.6	12.5
$C_6N_{10}H_6$*	-295	-296.7	1.7
$C_6N_{10}H_6$*	-207	-190.5	16.5
$C_6N_{10}H_6$*	-234	-227.7	6.3
$C_3N_6H_6$*	-275	-310.8	35.8
$C_3N_6H_6$*	-200	-209.8	9.8

[1] Aromatic N not attached to O atom. [2] Aromatic N attached to the O atom
[3] Aromatic N adjacent to hydrogenated C. [4] Aromatic N adjacent to methlyated C
* Melamine/Heptazine adducts not used in the scaling graph, the figures pictorially representing the different chemical shifts will be presented later in the chapter

Table 21: Experimental ^{15}N NMR chemical shifts (δ) and scaled theoretical predictions

5.2.3 Conclusion for Calculating Scaled NMR Chemical Shifts

A number of C-N molecules were investigated using the CASTEP code for predicting the ^{13}C and ^{15}N NMR chemical shifts. The calculated isotropic shielding parameters ($\sigma_{\text{iso.calc}}$) were subtracted from the reference values and scaled in order to convert them into comparable chemical shifts (δ_{scaled}) in ppm units. The isotropic chemical shift ($\delta_{\text{iso.calc}}$) was relative to TMS for ^{13}C and relative to nitromethane for ^{15}N, to allow for direct comparison with the referencing of experimental results. The reference $\sigma_{\text{iso.calc}}$ value for ^{13}C was 178.2 ppm and for ^{15}N was -168.5 ppm. A number of known experimental values were compared with our predicted theoretical values, to obtain the scaling formula, to account for systematic over or under estimations of the theoretical results. The scaling formula for ^{13}C was determined to be $\delta_{\text{scaled}} = 0.9295\delta_{\text{iso.calc}} - 0.8771$ and for ^{15}N was determined to be $\delta_{\text{scaled}} = 0.9114\delta_{\text{iso.calc}} - 16.6130$.

The results presented above show that CASTEP calculations with the parameters used in this research could be employed reliably to estimate the chemical shifts of C-N materials. The local environment for the C-N materials can be better understood, when interpreting new experimental NMR data, or predicting chemical shifts for new postulated C-N structures. The application of this calibrated method is applied for triazine based C-N materials, in Section 5.3, and for synthesised C-N materials in Chapter 6.

5.3 NMR Chemical Shift Predictions for Aromatic Carbon Nitrides

In this section we discuss the prediction of NMR chemical shifts for aromatic C-N molecules (traizines), which are commonly found as building blocks in the structure of C-N materials at ambient conditions. The ^{1}H NMR chemical shifts are also presented, as most synthetic C-N contain an appreciable amount of H from incomplete condensation of the precursors. Information on ^{1}H NMR chemical shifts would be useful for structure determination for future synthetic attempts in this area of research.

The ^{1}H NMR chemical shifts were referenced to calculated TMS, and although a systematic scaling of ^{1}H NMR chemical shifts have not been scaled, it was found that non-scaled $\delta_{exp} = \sigma_{ref} - \sigma_{calc}$, was accurate for identifying the isomeric state of Glycine. This investigation was conducted in a separate collaborative project, with Dr Abil Aliev from UCL Department of Chemistry, and the results have been reported in the literature [108]. The calculated σ_{ref} for ^{1}H is 31.1 ppm.

The same level of theory, as described in Section 5.2, was employed for the geometry optimization and NMR chemical shift calculations of these materials. For the molecular based units, different sized unit cells were tested to ensure the unit cell was large enough to prevent interactions between periodic images. We found the following unit cell sizes were sufficient for the structure optimization and NMR calculations; for single melamine and heptazine molecular structures the unit cell size was (10 Å)^3 and for the larger heptazine based molecular structures the unit cell size was (20 Å)^3.

In Chapter 6 the theoretical predictions are used further, to support the elucidation of a new graphitic C-N structure. A group from Germany recently reported the proposed C-N arrangement in the literature [48], and as part of our theoretical NMR study the graphitic forms were also considered and modeled.

5.3.1 Predicted Melamine and Heptazine NMR Chemical Shifts

The molecular structures for melamine and heptazine are presented in Figures 37 and 38, with the scaled NMR chemical shift for each symmetry unique atom highlighted with an arrow. In the images the H atoms are white, C atoms are grey and N atoms are blue.
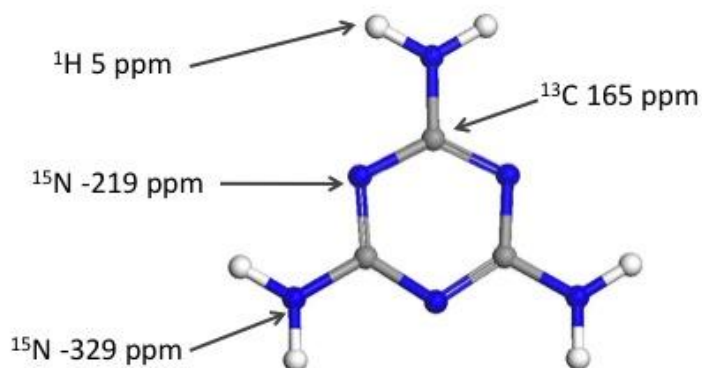
Figure 37: Calculated and scaled NMR chemical shifts in ppm for Melamine

Figure 38: Calculated and scaled NMR chemical shifts in ppm for Heptazine

The chemical shifts of equivalent atoms in these two molecules are very similar. The ^{1}H NMR chemical shift, as a result of the NH_2 groups, differs by only 1 ppm in melamine and heptazine and would be indistinguishable in experimental spectra. In melamine there are three C atoms bonded to a NH_2 group and two N atoms in the triazine ring, whose ^{13}C NMR chemical shift is 165 ppm. The corresponding C atom in heptazine gives rise to a predicted ^{13}C NMR chemical shift at 162 ppm. There is only 3 ppm difference between these C atoms.

When compared with melamine, the heptazine structure has three C atoms in another environment, the C is bonded to three N atoms, and is responsible for the fusion between two triazine rings; the corresponding ^{13}C NMR chemical shift is 154 ppm. For a C-N system that had heptazine present we would expect to find two ^{13}C NMR chemical shifts in the experimental spectra with 1:1 intensity ratio. It would be difficult to determine whether a pure product with one type of structural

ring arrangement has formed based on ^{1}H and ^{13}C NMR chemical shifts alone, for this reason the ^{15}N NMR chemical shifts play an important role in structure determination. There are two N atoms that are in a similar environment in both structures. One N atom forms the NH$_2$ group that gives a ^{15}N NMR chemical shift of -329 ppm in melamine and -298 ppm in heptazine. The other N atom is found on the outer edge of the aromatic rings and gives -219 ppm and -190 ppm ^{15}N NMR chemical shifts, for melamine and heptazine respectively. In experimental spectra the distance between these chemical shifts would be far enough apart, to consider the chemical shifts resulting from differing bonding environments. The heptazine molecule has a unique N atom that is central to the structure, and results from the fusion on three triazine rings; the corresponding ^{15}N chemical shift is predicted as -228 ppm.

The theoretical NMR predictions so far, using the CASTEP code, could be used to determine whether a structure contained heptazine, by the presence or absence of the additional C atom, and the presence or absence of the central N atom, both involved in the fusion of triazine rings.

The calculated chemical shifts for all the atoms in melamine and heptazine are collated in Table 22.

5.3.2 Predicted NMR Chemical Shifts for Larger Heptazine Agglomerates

NMR shifts originating from triazine condensation in polymeric heptazine agglomerates, as would occur in C-N synthesis were investigated. Heptazine agglomerate structures were modeled by joining three heptazine units to form a 3-membered ring structure (3 x heptazine), represented in Figure 39 and six heptazine units to form a 6-membered ring structure (6 x heptazine), represented in Figure 40.

By modeling these larger heptazine structures, a number of features arising from NMR chemical shift predictions that remain consistent, regardless of the size of the structure, can be determined and understood.
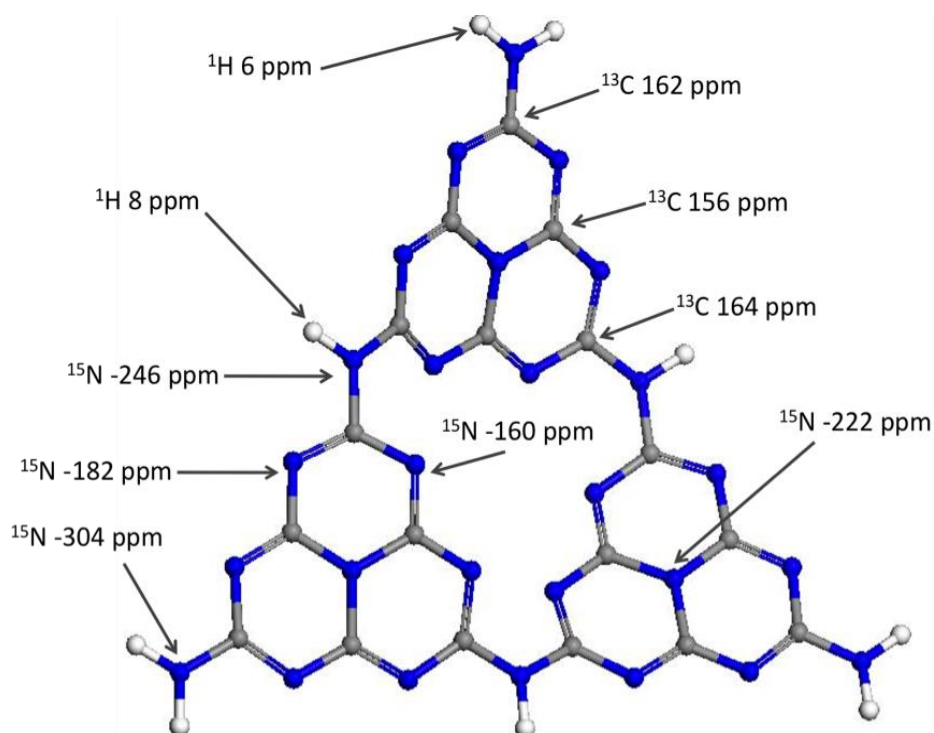
Figure 39: Calculated NMR chemical shifts (scaled) for 3 x Heptazine ring structure
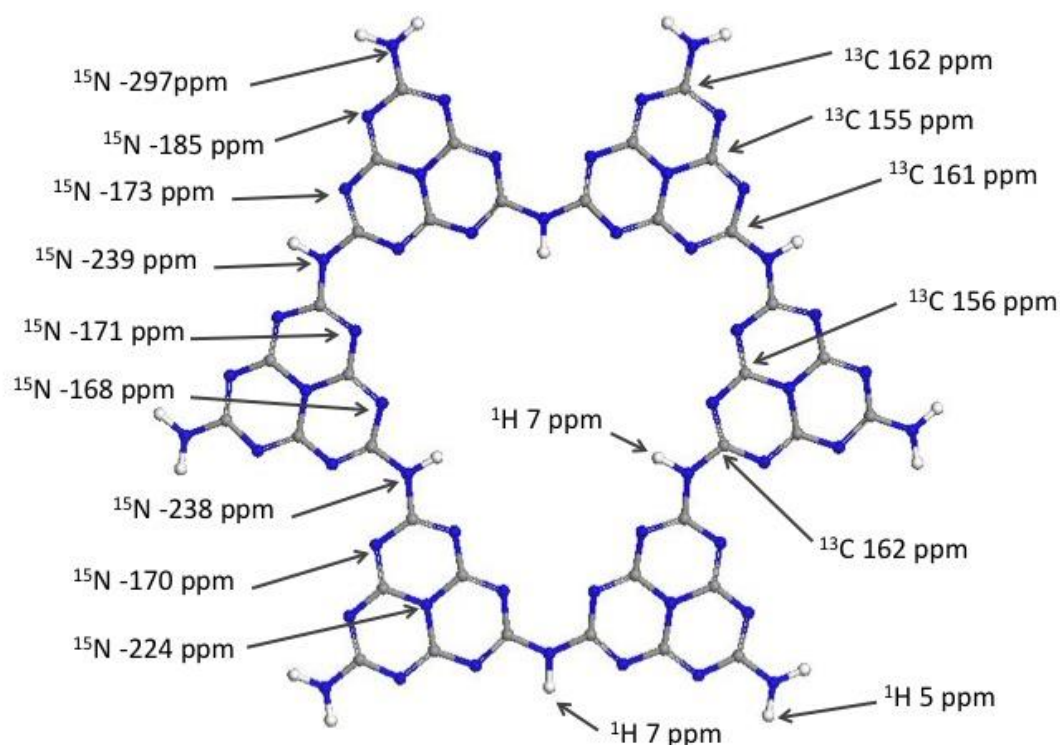
Figure 40: Calculated NMR chemical shifts (scaled) for 6 x Heptazine ring structure

The outermost NH_2 group give ^{15}N NMR chemical shift in the range of -297 to -304 ppm, which is consistently in the region of ~30 ppm lower than melamine.

The formation of a three-unit heptazine ring introduces the potential for a C atom to be next to a N-H bridging N atom, giving a ^{13}C NMR chemical shift at 164 ppm. When the ring size is further expanded to a six-unit heptazine ring, the orientation of the proton arising from the N-H bond (either facing in or out of the ring), generates two C environments (next to a NH pointing in or out of the ring), whose predicted chemical shift is 161 and 162 ppm; since the shift is so similar it is expected to be difficult to differentiate in experimental spectra. Overall, for

heptazine-based agglomerates there are three main C environments with calculated chemical shifts at 162, 161–164 and 155-156 ppm. Although the shifts in the 160s would be difficult to differentiate and assign, in any experimental data broad peaks would be predicted, in this region of the spectra.

The ^{15}N NMR chemical shifts gave similar results for both the larger heptazine based units. The NH_2 environment gave rise to a chemical shift at $\sim$ -300 ppm. The N-H bridging group in the 3 x heptazine unit was modeled with the proton facing out from the C_9N_9 ring and gave a chemical shift at -246 ppm. For the 6 x heptazine unit, the cavity was larger, and the calculated ^{15}N chemical shift for the N-H group was predicted at $\sim$ -238 ppm, irrespective of whether the proton was facing inside or outside the ring. The N atoms in the triazine ring next nearest the NH_2 group gave chemical shifts at $\sim$ -184 ppm for the larger heptazine units, for the single heptazine unit this chemical shift was -190 ppm (and for melamine -219 ppm). This large difference would allow, when interpreting experimental data, to determine whether a heptazine or melamine based unit is present, or even if there is a mixture of these C-N ring structures within a sample.

For the N atoms that are part of the heptazine ring situated near a N-H bridging group, the chemical shift calculated was affected by the size of the $CxNy$ ring formed. For the 6 x heptazine unit, the ^{15}N NMR chemical shift was predicted to be $\sim$ -170 ppm, whether the N atom was inside the ring or situated on the outer edge. For the 3 x heptazine unit, if the N was on the outer edge of the structure the chemical shift was predicted to be -182 ppm, and if the N was inside the C_9N_9 ring

the chemical shift was calculated to be -160 ppm. This small but significant difference between these N chemical shifts provide a useful indication as to whether smaller or larger heptazine based rings have formed, when interpreting experimental spectra.

A full summary of the different atomic environments and the predicted chemical shifts, for all triazine based molecular structures discussed above, are tabulated and presented in Table 22.

Type of Bond	Calculated Chemical Shifts (scaled) for Triazine Based Molecular Units (ppm)		
	^{1}H	^{13}C	^{15}N
NH$_2$	5[a], 6[b], 6[c], 5[d]	-	-329[a], -298[b], -304[c], -297[d]
Outer triazine ring, next to NH$_2$	-	165[a], 162[b], 162[c], 162[d]	-219[a], -190[b], -183[c], -185[d]
NH pointing out	8[c], 7[d]	-	-246[c], -239[d]
NH pointing in	7[d]	-	-238[d]
Outer triazine ring, next to NH facing in	-	162[d]	-170[d]
Inner triazine ring, next to NH facing in	-	162[d]	-168[d]
Outer triazine ring, next to NH facing out	-	164[c], 161[d]	-182[c], -173[d]
Inner triazine ring, next to NH facing out	-	161[d]	-160[c], -171[d]
Central N in heptazine	-	-	-228[b], -222[c], -224[d]
C outer perimeter of heptazine ring	-	154[b], 156[c], 155[d]	-
C inner perimeter of heptazine ring	-	156[c], 156[d]	-
a = Melamine, b = Heptazine, c = 3 x Heptazine, d = 6 x Heptazine			

Table 22: Summary of the calculated ^{1}H, ^{13}C, ^{15}N NMR chemical shifts (scaled) obtained for melamine, heptazine and heptazine based molecular units

5.3.3 Conclusion for Predicted NMR Chemical Shifts for Melamine and Heptazine Based Structures

Triazine based structures that are often present in CN synthesis, were investigated using the CASTEP code, for predicting NMR chemical shifts. Melamine was modeled in its molecular form, which resulted in one C atom environment (part of the triazine ring) and two N atom environments (part of the triazine ring or the NH$_2$ group). The predicted NMR chemical shifts for the atoms in the melamine model were found to be different to those in heptazine, even for atoms in a similar environment.

The C atoms in the melamine structure exist in one environment, and any experimental spectra for a pure melamine system is expected to give a sharp ^{13}C NMR chemical shift at 165 ppm, only 3 ppm higher than heptazine with C in the same environment. This subtle difference between the C-N starting materials is important to note for full appreciation of the overall atomic connectivity.

The NH$_2$ group gave a ^{15}N NMR chemical shift that differed by approximately 30 ppm between the melamine model and the three different heptazine structures, which was -329 ppm and ~-300 ppm respectively. All the heptazine models were found to be consistently ~-300 ppm, regardless of the size of the ring structure.

The heptazine structure had a uniquely bonded N atom that fused together three triazine rings and gave a ^{15}N NMR chemical shift at -228 ppm. This particular chemical shift has the potential to be an indicator to the presence or absence of

heptazine, within a structure. Larger heptazine ring systems were modeled, by joining together either three or six heptazine units; this gave rise to an increased number of C and N atomic environments. The central N environment was almost unaffected by the increased number of heptazine units and the ^{15}N NMR chemical shift ranged between -222 to -228 ppm, when all the systems were compared.

A number of differences between the melamine and heptazine based materials have been identified by these NMR chemical shift predictions. A synthesised product that is made up of these materials can be identified using NMR experimental techniques, guided by theoretical predictions. These results hold the potential to form the tools for structure elucidation.

Chapter 6

Application of Calculated NMR Parameters for Synthesised Carbon Nitride Materials

6.1 Introduction

Experimental solid-state NMR techniques were employed to investigate the bonding environments for C, N, H in samples synthesised as part of this research. The assignment of the NMR chemical shifts for these structures required further theoretical predictions for a range of C-N materials, in addition to those on molecular aggregates discussed in Chapter 5.

In the previous chapter the use of NMR techniques using the CASTEP code was explored as a method to assess atomic connectivity for C-N systems, for which calculated chemical shifts were shown to be useful in determining the atomic arrangement. In this Chapter, the use of the NMR method is employed to improve the understanding of the topology of extended graphitic C-N materials prepared by two synthetic methods. These graphitic materials were synthesised using facilities at UCL Department of Chemistry, as part of the research towards this PhD thesis. The experimental techniques were either ionothermal or thermal, and were shown to yield two different carbon nitride materials. A set of molecular precursors

(DCDA, melamine, cyanuric chloride) was used in the thermal method, the full experimental details for both methods are provided in Appendix 1. The difference in the C-N material structure, as a function of preparation conditions, is confirmed by the IR and Raman spectra and the XRD pattern, also provided in Appendix 1.

C-N materials have important electrochemical and photochemical properties, which is why it was important to characterise them. During this time the samples were tested for their photocatalytic properties, of which the ionothermal sample did not show any photocatalytic activity, whereas the thermally prepared samples did. The interest in testing the photocatalytic nature of these materials was to understand whether C-Ns could be a potential candidate in the effective extraction of H from H_2O [109].

Experimental ^1H, ^{13}C and ^{15}N NMR spectra were collected for these C-N samples at the national EPSRC ss-NMR facility at Durham University; simultaneously, theoretical predictions for plausible graphitic C-N materials were conducted. NMR spectra collected for all the thermally prepared samples showed chemical shifts in the same region, albeit with varying intensities. The spectra for thermally prepared sample Mel is presented in this chapter for comparison with the ionothermal sample (I.P) as the Mel sample gave the most intense chemical shifts; for reference a full set of ^{13}C and ^{15}N NMR spectra for the five thermally prepared samples are attached in Appendix 2 and Appendix 3, respectively.

The theoretical investigations were focused around C-N structures that had previously been postulated in the literature [47, 48] along the DCDA condensation pathway (DCDA ➔ Melamine ➔ Heptazine ➔ Melem ➔ Larger CN structures..). The NMR chemical shift predictions for molecular based melamine and heptazine structures were presented previously in Chapter 5; these results are referred to in the discussion below. In this Chapter, the graphitic C-N arrangement is based on the postulated structure proposed by Wirnhier *et al* in 2011, as the resulting material for the ionothermal synthetic method [48]. The structure is presented in Chapter 1, Figure 6. This graphitic C-N structure is investigated using the CASTEP code. Initially the graphitic structures were modeled without the presence of Li^+ or Cl^- ions (non intercalated models). Due to the preparation conditions in the ionothermal synthetic method (that occurs in a molten eutectic salt mixture), a thorough investigation of Li^+ and Cl^- ion intercalation was conducted. The effects of the degree of ion intercalation on the NMR chemical shifts allowed for better understanding of the experimental results. A theoretical study of graphitic C-N structures, in particular investigations on the effect of ion intercalation and NMR predictions, is not currently available in the literature.

This study is concluded by a discussion on the proposed connectivity for the C-N structural arrangement, for the solid-state materials prepared by the ionothermal and thermal methods.

6.2 Methods

6.2.1 Computational Details

Initially, purely C-N-H based graphitic systems were modeled without the presence of any salts or ions, in order to determine their expected chemical shifts. Following these calculations the effects of varying the number of ions (Li^+ and Cl^-) present within the system were modeled. Two calculations were conducted on each individual system modeled using the CASTEP code; geometry optimizations under periodic boundary conditions, where all atoms and cell dimensions were allowed to relax, followed by the NMR calculation on the optimized atomic coordinates.

A full investigation of the NMR chemical shifts resulting from the nature of graphitic layering was essential to understanding the effects of intercalation; to this aim two types of layering were modeled that were identified as AAA or ABA stacking arrangements. In AAA stacking the triazine rings were above and below each other in the adjacent layers. In ABA stacking the triazine rings alternated in positioning above voids of the adjacent layer (as opposed to another triazine). The layered structures are presented in section 6.3

The AAA stacking was further categorized to account for true AAA stacking i.e. each layer was structurally identical to the one above and below it, or whether the structural arrangement was the same, with a subtle difference in the orientation of the triazine rings (this affected the ordering of the N-H bridges). This latter stacking was labeled AA'A. Figure 41 represents the difference between the AAA and AA'A stacking; the protons have been omitted from the diagram. The N atoms

attached to the triazine rings are responsible for the bridging between adjacent rings, these host protons in the extended graphitic system.

AAA Stacking   *AA'A Stacking*
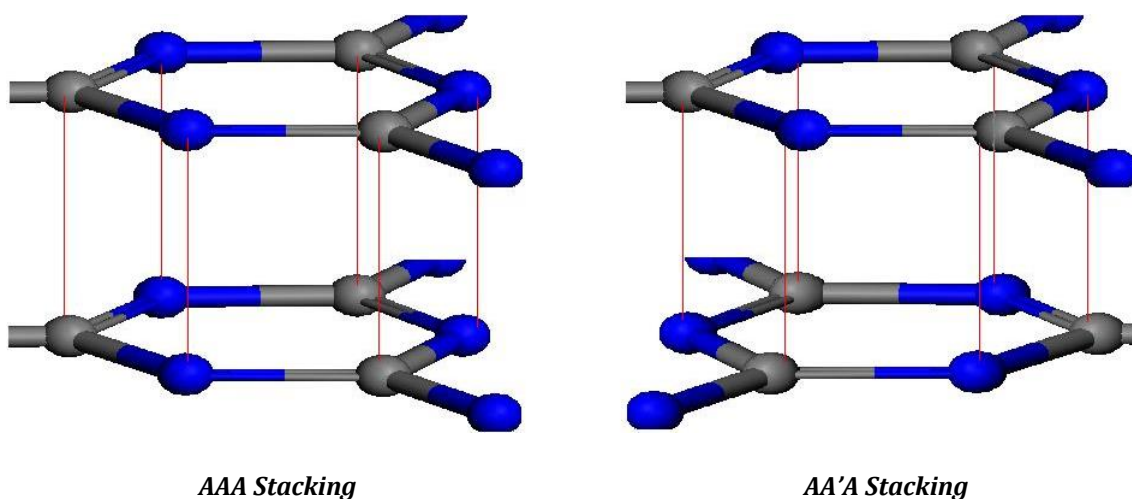
Figure 41: Triazine ring arrangement in the graphitic C-N system. Red line highlights the atoms that are situated directly below the atom in the layer above. AAA stacking (left) occurs when layers are repeated in an identical fashion, AA'A stacking (right) occurs when there is a reorientation of the triazine rings in every other layer. C is grey, N is blue.

The overall ordering of the proton in the AAA and AA'A stacking arrangements is depicted schematically in Figure 42.

AAA Stacking   *AA'A Stacking*
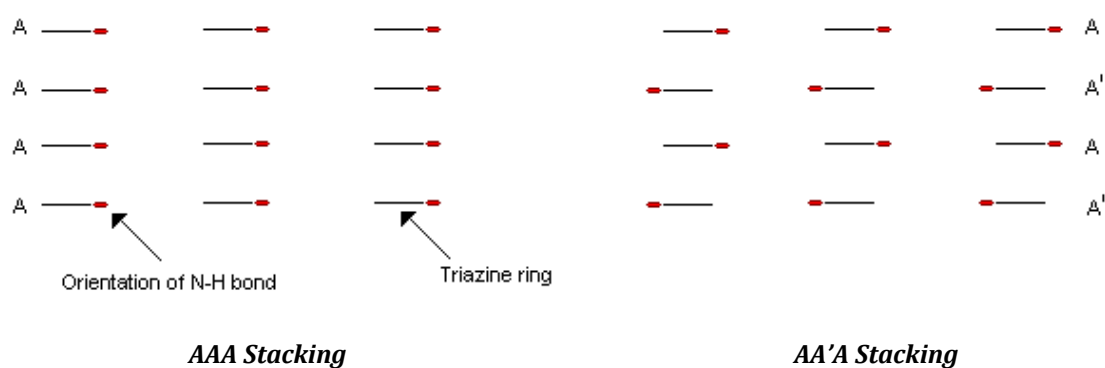
Figure 42: Orientation of the proton on the N-H bond, in the triazine based graphitic C-N system. AAA stacking (left) all protons repeated in an identical fashion, AA'A stacking (right) the N-H bonds alternate direction in every other layer.

In the ABA structure the graphitic layers are stacked so that a triazine ring is situated between $C_{12}N_{12}$ cavities, in every second layer. The ABA stacked structure was modeled using unit cell coordinates reported in the literature by Zhang *et al* [44]. The AAA and AA'A stacked C-N graphitic system was modeled using unit cell coordinates reported by Wirnhier et al [48]. Ions were introduced into the structural voids and during the calculations it was necessary to retain charge neutrality, which in turn restricted the number of ions that were intercalated within the structural $C_{12}N_{12}$ voids. Intercalation in ABA stacked structure was not calculated, due to the arrangements of the $C_{12}N_{12}$ voids and the triazine rings, the entry of ions is expected to be limited. Figure 43 represents the difference between the types of stacking and the ion intercalation.
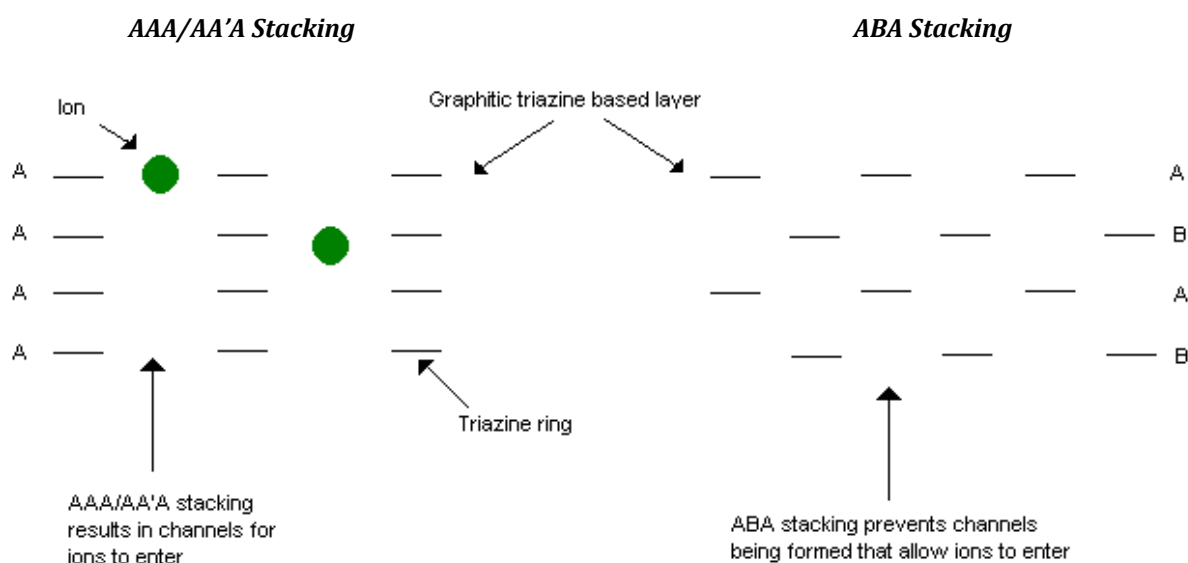
Figure 43: Ion intercalation in the AAA/AA'A (left) and ABA (right) stacking arrangement of the triazine based graphitic C-N system

The graphitic triazine based structure was modeled as an extended periodically repeating model, with the initial atomic coordinates and unit cell information taken from the literature [48]. A number of parameters were tested and it was found that k-point spacing at 0.07 Å and the cut off energy at 600 eV for these graphitic systems, provided suitable ground state results when compared with finer parameters, in all cases. The predicted NMR isotropic shielding parameters only differed by 0.01 ppm when comparing the same structure modeled using cut off energies of 600 and 700 eV.

For the AAA/AA'A triazine based extended graphitic structure of general composition $C_6N_9(H,Li)_4Cl$, the effect of varying the ratio of H^+ and Li^+ ions within the $C_{12}N_{12}$ cavities was determined by modeling materials of stoichiometry $C_6N_9Li_4Cl$, $C_6N_9HLi_3Cl$, $C_6N_9H_2Li_2Cl$ $C_6N_9H_3LiCl$, $C_6N_9H_4Cl$, $C_6N_9Li_3$, $C_6N_9H_3$. Whilst

all the structures could be geometry optimised, structures with more than two Li$^+$

ions per unit cell in the voids yielded metallic solutions for which the NMR

calculations did not converge. Therefore, NMR calculations have been performed

for the following compositions $C_6N_9H_2Li_2Cl$, $C_6N_9H_3LiCl$, $C_6N_9H_4Cl$ and $C_6N_9H_3$.

For the AA'A triazine based extended graphitic structure whose unit cell comprises

of two atomic layers, the effect of varying the H$^+$ and Li$^+$ ratio was explored by

studying materials of stoichiometry $C_{12}N_{18}Li_8Cl_2$, $C_{12}N_{18}HLi_7Cl_2$, $C_{12}N_{18}H_2Li_6Cl_2$,

$C_{12}N_{18}H_3Li_5Cl_2$, $C_{12}N_{18}H_4Li_4Cl_2$, $C_{12}N_{18}H_5Li_3Cl_2$, $C_{12}N_{18}H_6Li_2Cl_2$, $C_{12}N_{18}H_7Li_1Cl_2$,

$C_{12}N_{18}Li_6$, $C_{12}N_{18}H_6$. Although all the structures were successful in the geometry

optimisation calculations, only $C_{12}N_{18}H_7Li_1Cl_2$ and $C_{12}N_{18}H_6$ were insulating and

could be employed in the NMR isotropic shielding calculations. The CASTEP code

interpreted all other structures as metallic.

Following the NMR calculations, the C atoms were referenced to TMS (178.23

ppm) and N atoms to nitromethane (-166.48 ppm). The scaling factors determined

in Chapter 5 were used to correct ^{13}C and ^{15}N NMR chemical shifts, while ^{1}H NMR

chemical shifts referenced to TMS were not scaled. The calculated σ_{ref} for the H

atom was 31.1 ppm. Theoretically predicted NMR chemical shifts for these

materials are reported here for the first time, and will be applied to the

understanding of the products formed by the different synthetic pathways.

6.2.2 NMR Experimental Details

Solid-state NMR spectra were obtained at the EPSRC UK National Solid-State NMR Service at Durham. All the experimental NMR spectra were collected at room temperature and pressure on the Varian VNMRS spectrometer with a 9.4 T magnet. The full experimental set-up details are listed in Table 23. For the ^{13}C and ^{15}N NMR spectra, cross-polarization (CP) methods were used to enhance the signal intensity. Interrupted decoupling was used to identify direct attachment of ^{13}C and ^{15}N to protons. Magic angle spinning (MAS) was used to reduce the broadening of the NMR peaks for all three elements ^{1}H, ^{13}C and ^{15}N.

Atom	Experimental Detail
^{1}H	4 mm sample probe, 399.882 MHz, 10 ms acquisition time, 5.0 sec recycle time, 32 repetitions, spin rate 10000 Hz
^{13}C	6 mm sample probe, 100.562 MHz, 15 ms acquisition time, 1.0 recycle time, 176 repetitions, 1 ms contact time, spin rate 6800 Hz
^{15}N	6 mm sample probe, 40.527 MHz, 16.4 ms acquisition time, 3.0 sec recycle time, 9860 repetitions, 10 ms contact time, spin rate 3400 Hz

Table 23: Experimental set up on the Varian VNMRS spectrometer for acquiring the NMR spectra for ^{1}H, ^{13}C, ^{15}N

6.3 Calculated NMR Results

6.3.1 Non-Intercalated Graphitic Carbon Nitride Structures

The graphitic C-N material built on extended triazine rings has only one symmetry unique C atom, the N atoms are in two distinct environments; either a protonated imido N-H bridging group or part of the C_3N_3 triazine ring. Figure 44 depicts a single layer of the graphitic material. This layer formed the basis of AAA stacking.
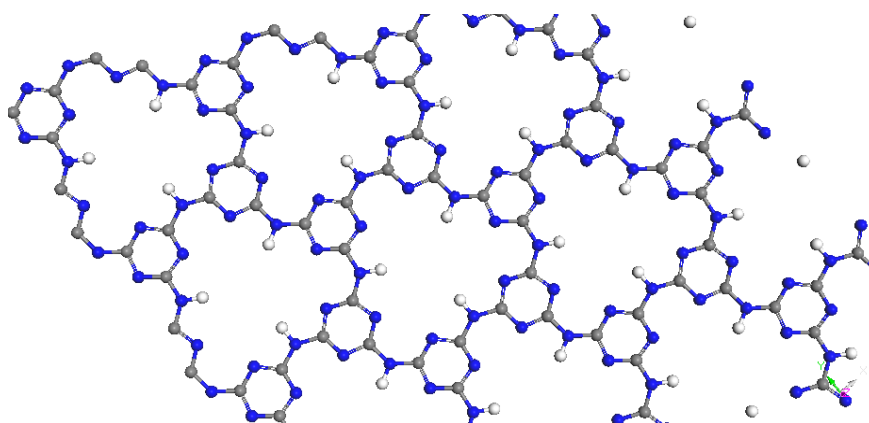
Figure 44: Single layer of the triazine based $C_6N_9H_3$ structures. All the C atoms are equivalent, N atoms are part of the triazine ring or N-H bridging group. C is grey, N is blue and H is white

The ABA stacked graphitic arrangement is best described as ½ the triazine rings in the 'A' layer are situated directly above and below the $C_{12}N_{12}$ cavity of the 'B' layer (circled green), and ½ the triazine rings are situated directly above and below another triazine ring (circled red) Figure 45. The triazine rings that are situated directly above and below one another follow the AA'A stacking arrangement shown in Figure 41.
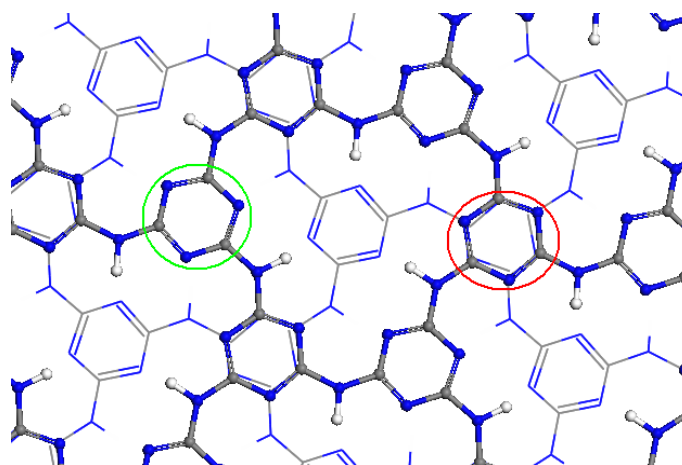
Figure 45: Melamine based $C_6N_9H_3$ structures, showing ABA stacking, the B layer is represented by the wire structure. In both layers C is grey, N is blue and H is white

The calculated and scaled ^{13}C NMR chemical shift for the C atoms in the AAA stacked C-N structure is predicted to be 162 ppm. The ^{15}N NMR chemical shift for N atoms that are part of the triazine ring structure are predicted to be at -172 ppm, and -246 ppm for the N-H bridging group. The calculated NMR chemical shifts for the ABA stacked C-N structure was identical to the AAA stacked structure. The AA'A stacked C-N structure resulted in similar chemical shifts; the C atoms were calculated to give the same chemical shift as the AAA and ABA stacking arrangements, whereas the ^{15}N NMR chemical shifts differed by only 1 ppm, calculated at -173 ppm and -246 ppm for the triazine and N-H bridging group respectively. These results indicate that orientation of the layers for the graphitic traizine sheets or the direction of the N-H bridging group (in the alternate layers) do not affect the NMR chemical shifts for the C and N atoms in the extended system.   The ^{15}N NMR chemical shifts differ significantly from the isolated melamine molecule; the triazine N is calculated to be -219 ppm and the NH_2 group

is calculated as -329 ppm. The C atom remains similar to the extended system at 165 ppm.

The NMR chemical shifts for both C and N atoms are very similar for the melamine and heptazine based extended structures. The results for the heptazine-modeled systems were presented previously in Chapter 5. To determine which triazine based ring system is the 'building block' for a synthesised carbon nitride material, one should look for the presence/absence of ^{15}N NMR chemical shift for the central N atom (bonded to three C atoms) in heptazine, at $\sim$ -224 ppm. For a purely melamine based structure the C atom would appear in one environment as opposed to two for the heptazine based structures, and there would only be two N environments present.

6.3.2 Intercalated Graphitic Carbon Nitride Structures

The structure discussed in Section 6.3 has $C_6N_9H_3$ composition; it is known that the materials synthesised from the molten eutectic salts contained Li^+ and Cl^- ions. The structures with LiCl intercalated are considered here in both AAA and AA'A starting geometries. When using AAA stacking the crystallographic cell contains 6xC and 9xN atoms, while the AA'A cell contains 12xC and 18xN.

6.3.2.1 AAA Stacked

Table 24(a) summarises the final enthalpy and equilibrium volume information for each optimised AAA stacked $C_6N_9H_aLi_bCl_c$ structure. Five structures have large

final volumes above 400 $Å^3$, which can be explained by the presence of ions within the void and between the layers. An exception to this explanation is the $C_6N_9H_3$ composition, the structure results in the largest volume at 435 $Å^3$, but is not intercalated with either Li^+ or Cl^- ions; the lack of ions in the system reduces Van der Waals interactions between layers resulting in the layers being further apart, when compared to the other systems. The $C_6N_9H_4Cl$ structure was calculated to have a compact volume of 232 $Å^3$, when compared with the other AAA stacked structures. The small volume is explained by the Van der Waals interactions taking place between the protons bonded in the C-N framework and the attraction to the Cl^- ion located in the $C_{12}N_{12}$ cavity. The attractive forces between charged ions extend to the layers above and beneath the cavity, hence reducing the overall volume of the structure. The initial and optimised structural arrangements for each composition are presented in Table 24(b).

Structural Stoichiometry	Volume ($Å^3$)	Final Enthalpy (eV)
$C_6N_9HLi_3Cl$	415.15	-4420.41
$C_6N_9H_2Li_2Cl$	423.71	-4242.18
$C_6N_9H_3LiCl$	412.74	-4064.59
$C_6N_9H_4Cl$	232.43	-3886.83
$C_6N_9Li_4Cl$	353.18	-4597.11
$C_6N_9H_3$	435.40	-3440.79
$C_6N_9Li_3$	421.17	-3972.90

Table 24(a): The volume ($Å^3$) and final enthalpy (eV) for the optimised $C_6N_9H_aLi_bCl_c$ AAA stacked structures
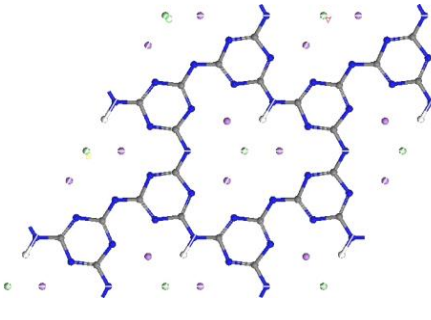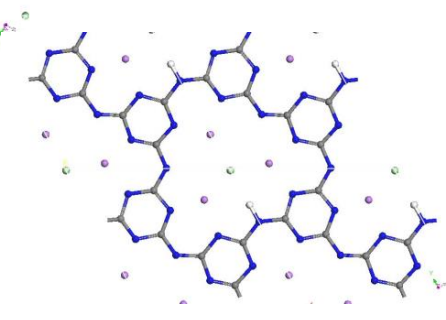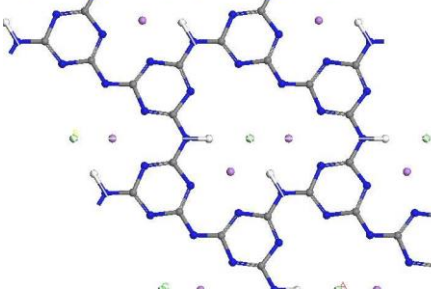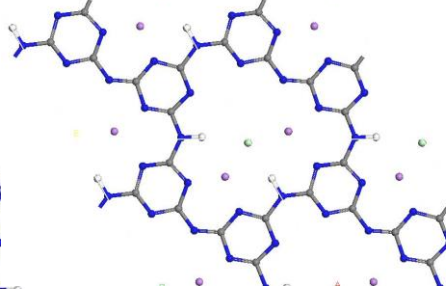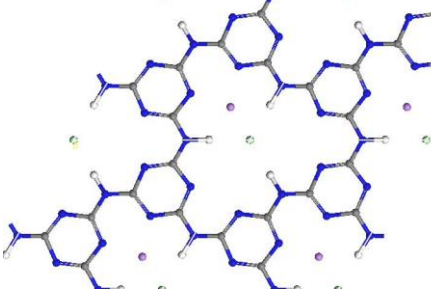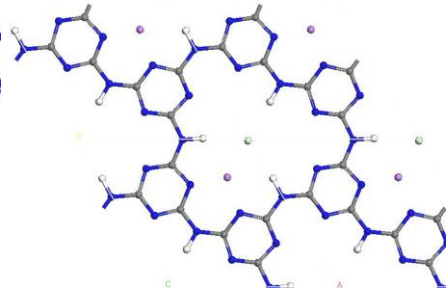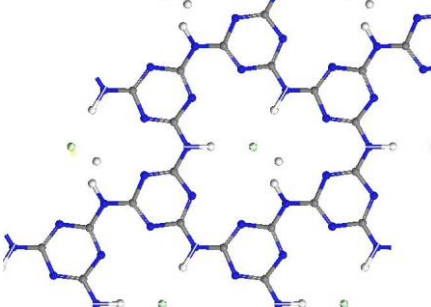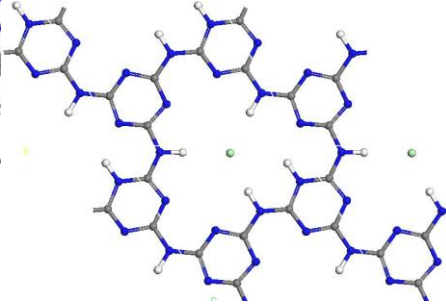
Structural Stoichiometry	Initial Structure	Optimised Structure
$C_6N_9H_1Li_3Cl$		
$C_6N_9H_2Li_2Cl$ *		
$C_6N_9H_3LiCl$ *		
$C_6N_9H_4Cl$ *		

Table 24(b) part 1/2: Summary of the optimised $C_6N_9H_aLi_bCl_c$ AAA stacked structures
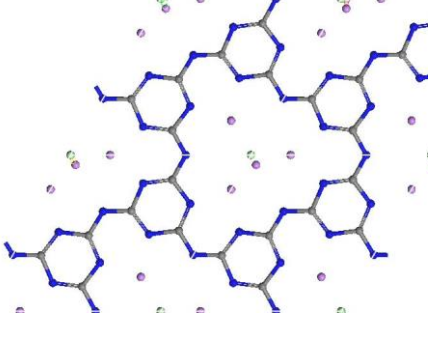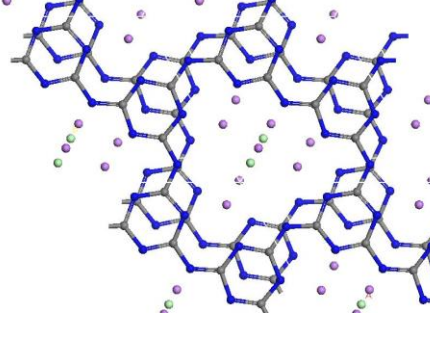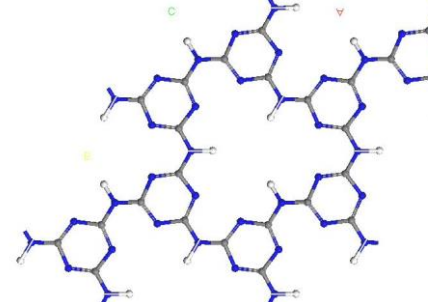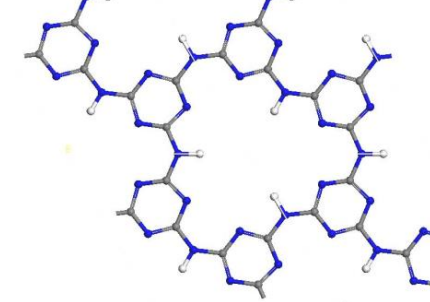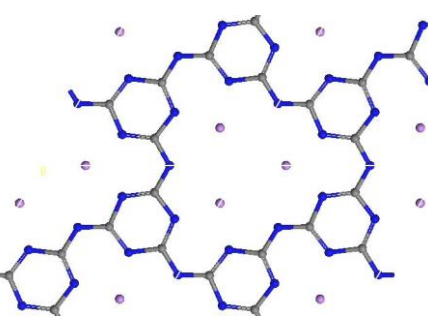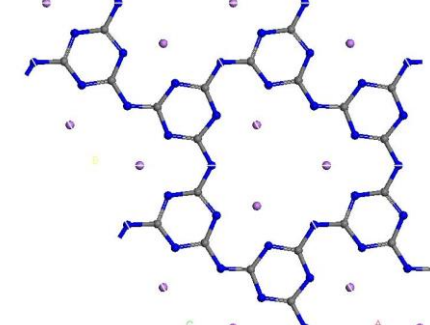
Structural Stoichiometry	Initial Structure	Optimised Structure
$C_6N_9Li_4Cl$		
$C_6N_9H_3$ *		
$C_6N_9Li_3$		

Table 24(b) part 2/2: Summary of the optimised $C_6N_9H_aLi_bCl_c$ AAA stacked structures with varying H^+/Li^+ and Cl^- ions, before and after geometry optimization. Structures marked with * are discussed further regarding NMR calculations. Colour code: N is blue, C is grey, H is white, Li is purple, Cl is green. For ion positions between layers in the optimised structure, refer to Appendix 4

The structure $C_6N_9Li_4Cl$ resulted in the most interesting optimised structure, where the final stacking arrangement was affected. All other arrangements were

layered in a similar manner to the starting atomic arrangement, where the structural layers could be superimposed on one another once optimised. However, with $C_6N_9Li_4Cl$ the final framework resulted in a staggered arrangement to accommodate the presence of the Li^+ and Cl^- ions within the cavity.

All the optimised C_6N_9 rings were larger in volume and appeared visually 'rounded' compared with the initial starting structure; $C_6N_9H_3$ achieved the largest volume upon optimisation. The lack of ions and hence dispersion forces within this structure caused the layers to exfoliate, creating a larger distance between the layers when compared with the other AAA stacked structures.

6.3.2.1.1 Calculated NMR Chemical Shifts

NMR chemical shifts could only be calculated for the four following structures with AAA stacking: $C_6N_9H_2Li_2Cl$, $C_6N_9H_3LiCl$, $C_6N_9H_4Cl$, $C_6N_9H_3$

The calculated ^{13}C NMR chemical shifts for the AAA stacked structures that yielded insulating phases vary as a function of the number of ions within the cavity. The expected NMR chemical shift for a carbon in the triazine ring environment is 161 – 163 ppm. The presence of a Li^+ ion near a carbon in a triazine ring causes a chemical shift at 160 ppm ($C_6N_9H_3LiCl$), this was observed for both carbon atoms that were close to a Li^+ ion. Subsequently the carbon atoms that are furthest away from the Li^+ ion in the same structure give a chemical shift at 163 ppm, whilst the carbon atoms that are in between the nearest and furthest to the Li^+ ion give a shift of 162 ppm (as expected a value in between the two previously mentioned C

environments). The same behaviour is observed for the $C_6N_9H_2Li_2Cl$ structure, where the carbon atoms closest to the Li^+ ions give a slightly lower chemical shift value at 161 ppm, compared with the carbon atoms that are farthest away from the Li^+ ion (162 ppm). For the structures without a Li^+ ion in the central cavity the chemical shifts are similar to those C atoms that are far away from a Li^+ ion, with chemical shift values on average 162/163 ppm. For $C_6N_9H_3$ there are no ions present and all the carbon atoms are in the same environment and this is reflected in the chemical shifts being the same for each atom at 162 ppm. When interpreting experimental results the difference between ^{13}C NMR chemical shift for intercalated and non-intercalated systems is indistinguishable; the position of the Li^+ ions do not introduce a change to the chemical shifts, but may cause broadening of the peaks.

For $C_6N_9H_4Cl$ we observe an interesting shift for the carbon atoms in the protonated triazine ring; for the carbon atoms between a bridging N-H group and the protonated nitrogen in the triazine ring, the chemical shift is lowered dramatically to 150 ppm and 153 ppm. The third carbon atom in the same triazine ring, opposite the protonated nitrogen, and next to a NH bridging group gives a chemical shift at 160 ppm. Experimental NMR spectra that show chemical shifts in these regions could therefore be indicative of protonated triazine rings.

The ^{15}N NMR chemical shifts for AAA stacked structure gave the following predictions. The simplest structure, $C_6N_9H_3$ showed the bridging nitrogen atoms to give a chemical shift at -246 ppm, and the triazine nitrogen atoms -172 ppm.

When an additional proton was added to the layer ($C_6N_9H_4Cl$), this resulted in the imido bridging nitrogen to range between -237 to -245 ppm and the triazine NH to give a chemical shift at -249 ppm, with the other two nitrogen atoms in the ring giving chemical shifts at -159 ppm. The triazine N atoms in the other two rings gave chemical shifts at -170 to -174 ppm, similar to the $C_6N_9H_3$ structure.

When an additional Li^+ ion was added to the cavity ($C_6N_9H_3LiCl$) the ^{15}N NMR chemical shifts were affected in the following way, the normal triazine values (-174 ppm) were shifted to -166 ppm if they were far away from the Li^+ ion. The triazine N atoms that were close to the Li^+ ion gave the chemical shift of -201 ppm. The bridging N-H group chemical shifts appeared to be unaffected by the presence of the Li^+ ion and all gave a value at -241 ppm.

In the structure with two Li^+ ions ($C_6N_9H_2Li_2Cl$), the ^{15}N NMR chemical shifts for the protonated N were -245 and -242 ppm, similar to when the Li^+ ions were not present. The non-protonated bridging N shifted to -178 ppm. The N atoms in the triazine ring near a Li^+ ion shifted between -192 to -197 ppm, two exceptions were the N in the triazine ring near Li^+ ion shifting at -186 ppm and another triazine N far away from a Li^+ ion (and next to a non protonated bridging group) shifted at -147 ppm. The ^{15}N NMR chemical shifts are affected significantly by the presence and position of the Li^+ ions and whether or not the bridging N atom is protonated.

6.3.2.2 AA'A Stacked

Table 25(a) summarises the final enthalpy and equilibrium volume for each optimised AA'A stacked $C_{12}N_{18}H_aLi_bCl_c$ structure, and the images for initial and optimised structures are presented in Table 25(b). The structure to result in the largest volume is $C_{12}N_{18}Li_6$, this is explained by the repulsive forces between the Li^+ ions, which cause the layers to be pushed farther apart when compared to the other structures. The structure with the smallest volume is $C_{12}N_{18}H_2Li_6Cl_2$, which can be explained by the presence of the Cl^- ion in the $C_{12}N_{12}$ cavity surrounded by three Li^+ ions, this balances the repulsive forces between ions with the same charge and allows for the layers to be stacked closer together.

Structural Stoichiometry	Volume (Å^3)	Final Enthalpy (eV)
$C_{12}N_{18}HLi_7Cl_2$	460.74	-9018.32
$C_{12}N_{18}H_2Li_6Cl_2$	455.19	-8841.30
$C_{12}N_{18}H_3Li_5Cl_2$	456.50	-8662.57
$C_{12}N_{18}H_4Li_4Cl_2$	484.37	-8485.59
$C_{12}N_{18}H_5Li_3Cl_2$	487.27	-8307.69
$C_{12}N_{18}H_6Li_2Cl_2$	468.67	-8130.23
$C_{12}N_{18}H_7Li_1Cl_2$	491.26	-7951.74
$C_{12}N_{18}Li_8Cl_2$	474.16	-9195.72
$C_{12}N_{18}H_6$	512.78	-6881.70
$C_{12}N_{18}Li_6$	585.07	-7945.81

Table 25(a): The volume (Å^3) and final enthalpy (eV) for the optimised

$C_{12}N_{18}H_aLi_bCl_c$ AA'A stacked structures

Structural Stoichiometry	Initial Structure	Optimised Structure
$C_{12}N_{18}HLi_7Cl_2$		
$C_{12}N_{18}H_2Li_6Cl_2$		
$C_{12}N_{18}H_3Li_5Cl_2$		
$C_{12}N_{18}H_4Li_4Cl_2$		

Table 25(b) part 1/3: Summary of optimised $C_{12}N_{18}H_aLi_bCl_c$ AA'A stacked structures
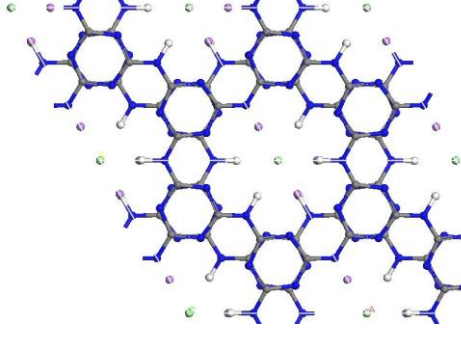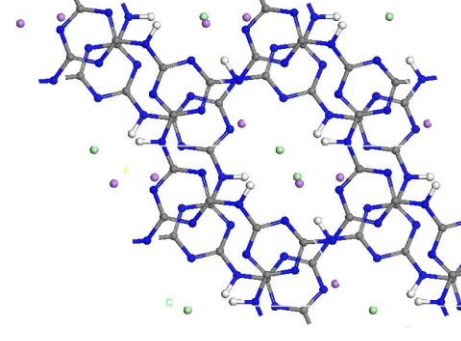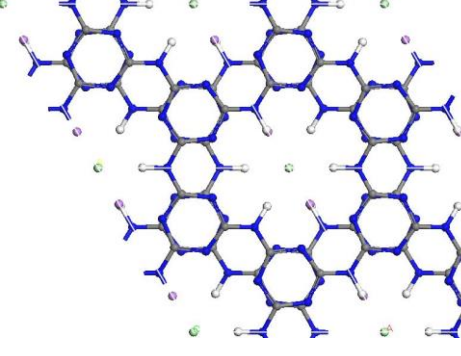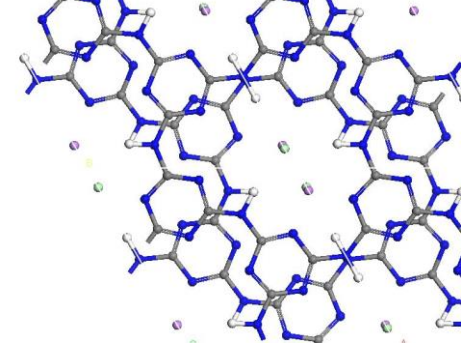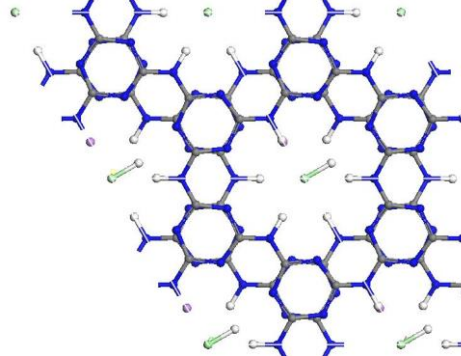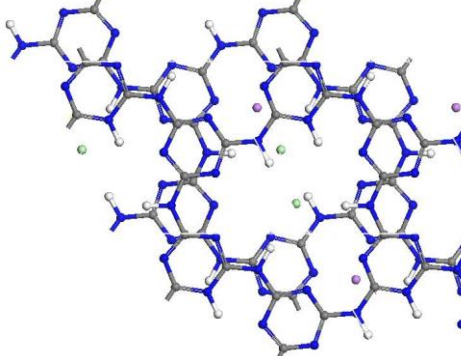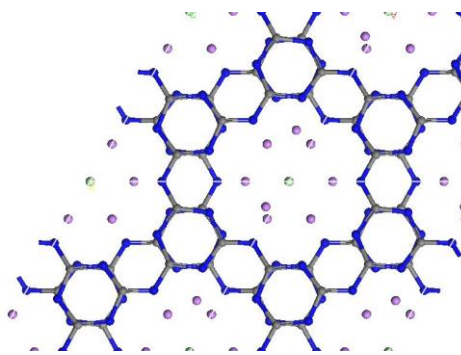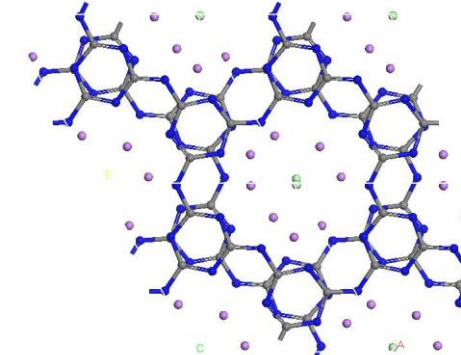
Structural Stoichiometry	Initial Structure	Optimised Structure
$C_{12}N_{18}H_5Li_3Cl_2$		
$C_{12}N_{18}H_6Li_2Cl_2$		
$C_{12}N_{18}H_7LiCl_2$ *		
$C_{12}N_{18}Li_8Cl_2$		

Table 25(b) part 2/3: Summary of optimised $C_{12}N_{18}H_aLi_bCl_c$ AA'A stacked structures
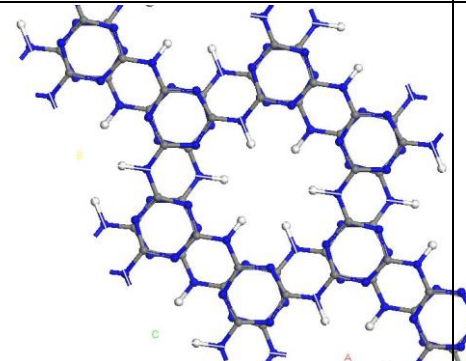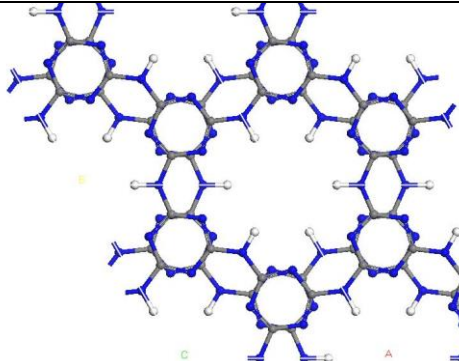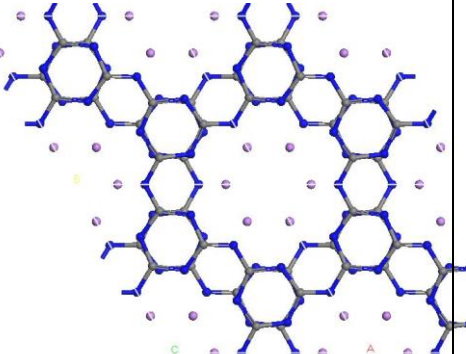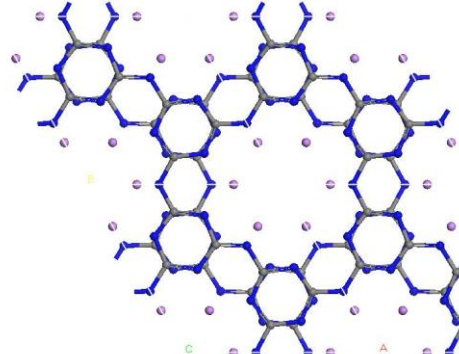
Structural Stoichiometry	Initial Structure	Optimised Structure
$C_{12}N_{18}H_6$ *		
$C_{12}N_{18}Li_6$		

Table 25(b) part 3/3: Summary of the optimised $C_{12}N_{18}H_aLi_bCl_c$ AA'A stacked structures with, before and after geometry optimization. Structures marked with * are discussed further regarding NMR calculations. Colour code: N is blue, C is grey, H is white, Li is purple, Cl is green. For ion positions between layers in the optimised structure, refer to Appendix 4

The AA'A stacked structures gave very interesting optimised structures; upon optimisation many atom arrangements became disordered from the initial starting geometry, which was modelled using the structure proposed by Wirnhier *et al* [48]. While most the $C_{12}N_{12}$ rings held their stacking arrangement, four structures either twisted or resulted in a staggered arrangement; $C_{12}N_{18}H_4Li_4Cl_2$,

$C_{12}N_{18}H_5Li_3Cl_2$, $C_{12}N_{18}H_6Li_2Cl_2$ and $C_{12}N_{18}H_7LiCl_2$, when optimised. In the starting geometry the Cl^- ion was positioned just above the $C_{12}N_{12}$ cavity for all compositions; upon optimisation the Cl^- ion was pulled into the centre of the cavity to be in the plane of the graphitic layer for four structures; $C_{12}N_{18}H_4Li_4Cl_2$, $C_{12}N_{18}H_5Li_3Cl_2$, $C_{12}N_{18}H_6Li_2Cl_2$, $C_{12}N_{18}H_7LiCl_2$. There is a direct correlation with the number of H atoms present in the structure and the final location of the optimised Cl^- ion; a minimum number of four H atoms are necessary to create the attractive forces that pull the negatively charged ion into the plane of the graphitic layer. Although the Li^+ ions are positively charged, they are not bound to the C-N framework, it appears that the presence of these ions in the plane of the structural cavity prevent the Cl^- ion from being drawn into the central cavity.

The $C_{12}N_{18}HLi_7Cl_2$ structure had the top layer consisting of one H attached to N and three Li^+ ions in the central cavity. The bottom layer hosted four Li^+ ions in the central cavity. When optimised, the H was repelled out of the graphitic plane, and the Cl^- ion appears to be drawn into the centre of the cavity, to be more central to the surrounding Li^+ ions.

The $C_{12}N_{18}H_2Li_6Cl_2$ structure had one H and three Li^+ ions in each layer. The optimised structure is flat and all the Li^+ ions are in the plane of the ring with Cl^- ions further away from the layers compared with the starting structure, as a result the distance between the layers is greater too. The length of the C-N bond for the N involved with the N-H bridging group is 1.384 Å, and the N-H bond length is 1.023 Å; the former bond is longer and the latter is shorter when compared with the

optimised $C_{12}N_{18}H_6$ structure that does not host ions for which the bond lengths are 1.381 Å and 1.024 Å respectively.

The $C_{12}N_{18}H_3Li_5Cl_2$ structure consists of the top layer hosting three Li^+ ions and no H ions, the bottom layer hosts three H and two Li^+ ions. This difference between the layers has an effect on whether layers remain flat. The layer with three H and two Li^+ ions is wavy, the Cl^- ion is at the centre of the cavity and the H in this layer points toward the Cl^- ion. The Cl^- ion in the bottom layer is closer to the ring (distance from ring is 1.046 Å) compared to the Cl^- ion in the top layer, which is almost double the distance from the ring in comparison (1.903 Å). A slight twisting of the layers results in the optimised form, and the layer with the three Li^+ ions remains flat, compared to the other layer that can be described as being slightly wavy.

The $C_{12}N_{18}H_4Li_4Cl_2$ structure consists of one layer hosting one H with two Li^+ ions in the cavity. The other layer has three H and two Li^+ ions in the central cavity. The optimised layers are twisted and so do not stack the same way as in the starting configuration, with the Cl^- ions for both layers being closer to the C_6N_9 structure, the overall layers are wavy.

In the $C_{12}N_{18}H_6Li_2Cl_2$ structure, each layer hosts the one Li^+ ion and three H atoms in the cavity. The Cl^- ions started off above the cavity and the Li^+ ions in the plane of the rings. Upon optimisation the Cl^- ions are pulled into the cavity and the Li^+

ions are pushed out on either side of the Cl$^-$ ion, with the final positions showing the ions to be directly above one another.

In the $C_{12}N_{18}H_7LiCl_2$ structure, one layer starts with four H in the cavity, where the additional H is attached to a Cl$^-$ atom (and not to a N in the triazine ring). The other layer hosts a Li$^+$ ion in the central cavity. Upon optimisation the layers shear to give a staggered arrangement. The layer with the extra H is flat, whereas the layer with the Li$^+$ ion is slightly twisted. The ring cavities appear to be arranged such that maximum space is allowed for the arrangement of the ions.

The $C_{12}N_{18}Li_8Cl_2$ structure keeps the original arrangement of the AA'A stacking, although there appears to be slight strain between the layers by the twisting of the triazine rings, as well as some stretching of the bond for the bridging nitrogen group. Prior to optimisation there were three Li$^+$ ions in the ring cavity for each layer, with the fourth Li$^+$ ion just below the layer. Upon optimisation both the layers became wavy and the Cl- ions were hosted in between the layers, indicative that the intercalation by the Li$^+$ ions leaves insufficient space for Cl$^-$ ions within the layers.

Both $C_{12}N_{18}H_6$ and $C_{12}N_{18}Li_6$ structures behave in a similar way to one another. When optimised the ring cavity becomes more rounded and the layers are flat. $C_{12}N_{18}H_6$ keeps the same distance between the layers as the starting geometry, whereas $C_{12}N_{18}Li_6$ has a larger space between the layers, most likely to be explained by the repulsion of the positive charge on the Li$^+$ ions.

6.3.2.2.1 Calculated NMR Chemical Shifts

NMR chemical shifts for the following 2 structures with AA'A stacking were calculated: $C_{12}N_{18}H_7LiCl_2$, $C_{12}N_{18}H_6$

The ^{13}C NMR chemical shifts for the AA'A stacked structures were predicted to be in the same region as the AAA stacked structures. For the $C_{12}N_{18}H_6$ structure all the C atoms were in identical environments and this was reflected in the ^{13}C NMR chemical shifts, predicted to be 162 ppm, the same as $C_6N_9H_3$. This suggests that the layering of the triazine based graphitic sheets does not introduce changes into the ^{13}C NMR chemical shifts. For the $C_{12}N_{18}H_7LiCl_2$ structure the ^{13}C chemical shifts vary depending on the distance of the C from the Li^+ ions, as would be expected. The C atoms in the triazine ring next to two protonated N atoms (one was a bridging nitrogen the other triazine nitrogen hosting a proton), gave chemical shifts of 149 and 152 ppm respectively. The third C atom in this ring opposite the protonated N gave a chemical shift at 160 ppm. These predictions were similar for the AAA stacked $C_6N_9H_4Cl$ structure. The C atoms near Li^+ ions gave chemical shifts at 161/162 ppm and those furthest away gave chemical shifts at 163 ppm (these carbons were in the same layer as the extra proton). When applying this information to interpreting experimental spectra we would expect to see broad peaks with shifts between 149 – 163 ppm, indicative of the different C environments available.

The ^{15}N NMR chemical shifts for the $C_{12}N_{18}H_6$ AA'A stacked structure were the same (with 1 ppm difference for the triazine N) as the AAA stacked $C_6N_9H_3$; the

triazine N shifts were all -173 ppm and the bridging N all were at -245 ppm. This indicates that the chemical shift for both the C and N atoms remained unaffected due to the stacking arrangement of the layers. For $C_{12}N_{18}H_7LiCl_2$ the extra proton in the layer affected the chemical shift of one of the N-H bridges that changed from -245 ppm to -238 ppm. The protonated N of the triazine ring was shifted to -252 ppm (from -173 ppm when non protonated); the other chemical shifts for the N atoms in the protonated triazine ring were -172 and -167 ppm. There were anomalous chemical shifts at $\sim$ -155 ppm for which an obvious explanation is not apparent in the protonated layer.

In the Li^+ layer the N atoms in the triazine ring shifted to -192 ppm when close to a Li^+ atom, the remaining chemical shifts were in the region of -166 to -173 ppm, for the triazine rings, consistent with the $C_6N_9H_3$ structure when there are no ions present. The imido bridging N-H groups all gave a consistent chemical shift at -242 ppm, in the same region as for other structures.

6.3.2.3 Structure Comparison for $C_6N_9H_aLi_bCl_c$; AAA and AA'A Stacked

The volume and final enthalpy values for the AAA and AA'A structures were tabulated in Table 26, for direct comparison between the two different types of stacking. The AA'A stacking arrangement is more stable in all cases, with the exception of $C_6N_9Li_3$ where the final enthalpy of the optimised structure is identical for both AAA and AA'A stacking arrangements.

Structural Stoichiometry	AAA stacked $C_6N_9H_aLi_bCl_c$		AA'A stacked $C_{12}N_{18}H_aLi_bCl_c$	
	Volume ($Å^3$)	Final Enthalpy (eV)	Volume ($Å^3$)	Final Enthalpy (eV)
$C_6N_9H_{0.5}Li_{3.5}Cl$	n.a	n.a	230.24	-4509.16
$C_6N_9HLi_3Cl$	415.15	-4420.41	227.60	-4420.65
$C_6N_9H_{1.5}Li_{2.5}Cl$	n.a	n.a	228.25	-4331.28
$C_6N_9H_2Li_2Cl$	423.71	-4242.18	242.18	-4242.80
$C_6N_9H_{2.5}Li_{1.5}Cl$	n.a	n.a	243.64	-4153.85
$C_6N_9H_3LiCl$	412.74	-4064.59	234.34	-4065.11
$C_6N_9H_{3.5}Li_{0.5}Cl$	n.a	n.a	245.63	-3975.87
$C_6N_9H_4Cl$	232.43	-3886.83	*	*
$C_6N_9Li_4Cl$	353.18	-4597.11	237.08	-4597.86
$C_6N_9Li_3$	421.17	-3972.90	292.54	-3972.90
$C_6N_9H_3$	435.40	-3440.79	256.39	-3440.85

Table 26: Volume ($Å^3$) and final enthalpy (eV) for the optimized $C_6N_9H_aLi_bCl_c$ triazine based AAA and AA'A stacked structures. The optimized primitive unit cell volume and final enthalpy for the AA'A $C_{12}N_{18}H_aLi_bCl_c$ cell have been halved (values in Table 25(a)) for direct comparison with the AAA cell of $C_6N_9H_aLi_bCl_c$ composition. Structures marked * failed to optimise during geometry optimisation.

The stability ranges from an energy difference of 0.748 eV for $C_6N_9Li_4Cl$ to 0.004 eV for $C_6N_9Li_3$. A clear trend between the two structural arrangements shows the AA'A stacking to be energetically favourable compared to AAA stacking for all atomic arrangements considered. The calculated final enthalpy value for the $C_{12}N_{18}H_6$ ABA layered structure was -3440.86 eV, with the final volume at 486.30 $Å^3$, this structure was 0.01 eV more stable when compared to the AA'A polymorph. Although the ABA structure is the most stable, the small energy difference means it

should be possible produce an AA'A stacked material, with similar stability. The volume for each structure shows the AA'A stacking to be more compact when compared with the AAA alternative. The $C_6N_9H_3$ structure calculated the same enthalpy value for both structural arrangements, with a large difference in the volume; the AA'A structure was ~130 Å^3 smaller in cell size. The polarity of the C-N bonds affects the overall volume and stability of the structure. The approximate doubling in volume size can be explained by electron repulsion caused by the arrangement of triazine rings in neighbouring planes, represented pictorially in Figure 41. A higher energy structure results when the triazine rings are situated above and below C and N atoms with the same orientation (as in AAA stacking). Electron repulsion is reduced when the triazine rings are rotated so that the C in one triazine ring is situated above and below a N of another triazine ring in adjacent layers, hence allowing for more compact structural arrangements.

Whilst the graphitic C-N structure with AAA stacking is not the energetically favourable arrangement when the final enthalpy values are compared, the calculated NMR chemical shifts are still of interest to understand the effect of the presence of ions and interlayer interactions on the C and N atoms. In section 6.3.2 an important finding based on the investigation of both AAA and AA'A stacked structures was the sensitivity to the Li$^+$ ions; ^{13}C NMR chemical shifts did not show as much sensitivity to Li$^+$ ions, compared to ^{15}N atoms; when N-H was replaced by N.Li$^+$ the chemical shift was affected.

6.4 Experimental NMR Chemical Shift Results

6.4.1 ^{13}C NMR Chemical Shifts

The ^{13}C NMR chemical shift spectra produced by the ionothermal and thermal synthetic methods is represented in Figure 46. All the samples prepared by the thermal method produced similar ^{13}C NMR chemical shift spectra with regard to the peak positions (differing only in intensities), the Mel sample gave the most intense peaks and is represented in the figure.
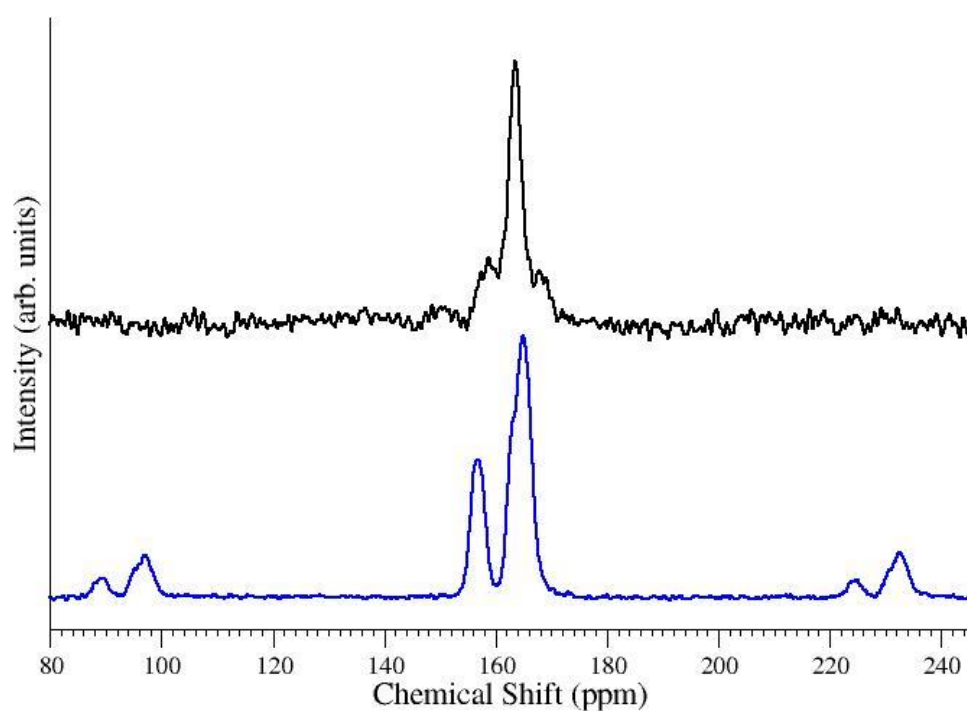
Figure 46: Experimental ^{13}C CP-MAS NMR Chemical Shift Spectra for I.P and Mel carbon nitride samples. Black = ionothermal sample (I.P), Blue = thermal sample (Mel). To view spectra for all samples refer to Appendix 2

The spectra obtained for the thermal sample (Mel) showed two ^{13}C NMR chemical shifts, observed at 165 ppm and 157 ppm, suggesting the C atoms present in the carbon nitride system are in two distinct environments. These resonances are in line with a heptazine based structure and the theoretical predictions for two C environments at ~ 155 and ~ 163 ppm. The chemical shift at 165 ppm appears to be asymmetric, suggesting the possibility that there is another signal present within this resonance, which is masked/hidden by the intensity of the peak at 165 ppm. The shoulder appears to be at ~ 162 ppm, and a heptazine based structure would explain this, as there are two predicted C chemical shifts that are very similar, only differing by 2 ppm and these shifts are dependent on the neighbouring NH_2/NH group. The shoulder, although present in all samples prepared using the thermal method, is more pronounced in two thermally prepared samples (D.M.C and especially in Mel). It is possible that this material also has triazine units present, as suggested by the chemical shift at 162 ppm; the shoulder that appears in the spectra may be due to the presence of traizine units.

The I.P sample showed a completely different NMR spectra when compared to the thermal sample; the C was predominantly present in one environment, at 163 ppm, with a further two resonances at 158 and 169 ppm. The resonance at 163 ppm is in line with a triazine-based structure. When comparing this to the reported ^{13}C NMR spectra in the literature [48], which showed the C atom to exist in three environments, the difference in resonance intensity is attributed to the contact time used; 1 ms, as opposed to 10 ms as reported in the literature. The 158 and 169 ppm chemical shifts are proposed to be due to the presence of Li$^+$ and

Cl⁻ in the material. The calculated theoretical predictions for these structures showed that the presence of the ions resulted in a range of ^{13}C NMR chemical shifts between 150 – 163 ppm. Theoretical predictions for this structure with intercalated ions have not previously been reported and these predictions can be used to support the structural model previously proposed for this material.

Interrupted decoupling experiments for the C atom showed no signal suppression for either of the six samples, clearly indicating that the C atoms present are not directly attached to H atoms.

These peak positions match well with experimental ^{13}C NMR shifts predicted for triazine based carbon nitrides in particular; for melamine (168 ppm) and its derivative heptazine (165, 156 ppm).

6.4.2 ^{15}N NMR Chemical Shift Results

Five main chemical shifts were observed for the samples prepared using the thermal experimental method; these were -179, -190, -225, -245, -264 ppm, suggesting the N atoms present in the system are in five distinct environments. The chemical shift at -225 ppm was best seen for the D.M.C sample. As for the ^{13}C NMR, the sample prepared by ionothermal synthesis (I.P), showed different ^{15}N NMR chemical shifts compared to the thermal samples. Three main resonances were observed at -177, -190 and -249 ppm. The NMR spectra are displayed in Figure 47.
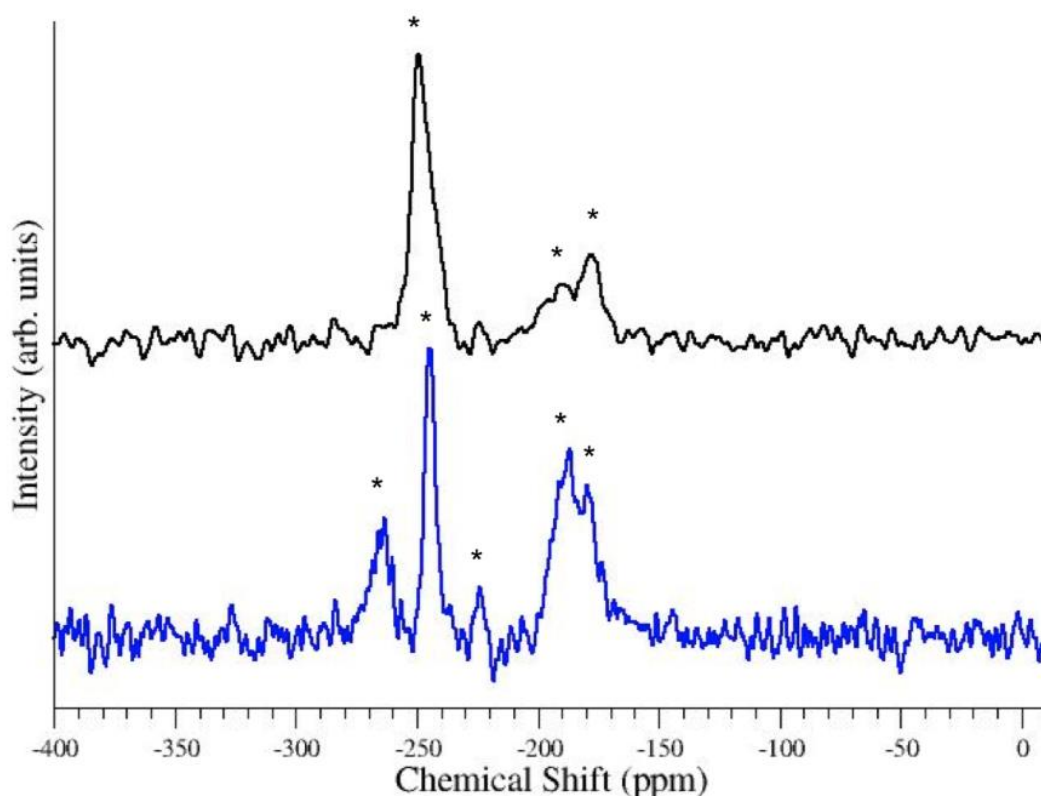
Figure 47: Experimental ^{15}N CP-MAS NMR Chemical Shift Spectra for carbon nitride materials. Black = ionothermal sample (I.P), Blue = thermal sample (Mel), * = chemical shifts of interest. To view spectra for all samples refer to Appendix 3

An interrupted decoupling experiment was carried out to determine which signal could be assigned to the N atoms attached to, or in very close vicinity to, a proton. This experiment allows for the determination of atom connectivity and the most likely topology present in the structure. The effects of interrupted decoupling are seen in Figure 48, where the solid line is the interrupted signal and the dashed line is the continuous signal (from Figure 47).
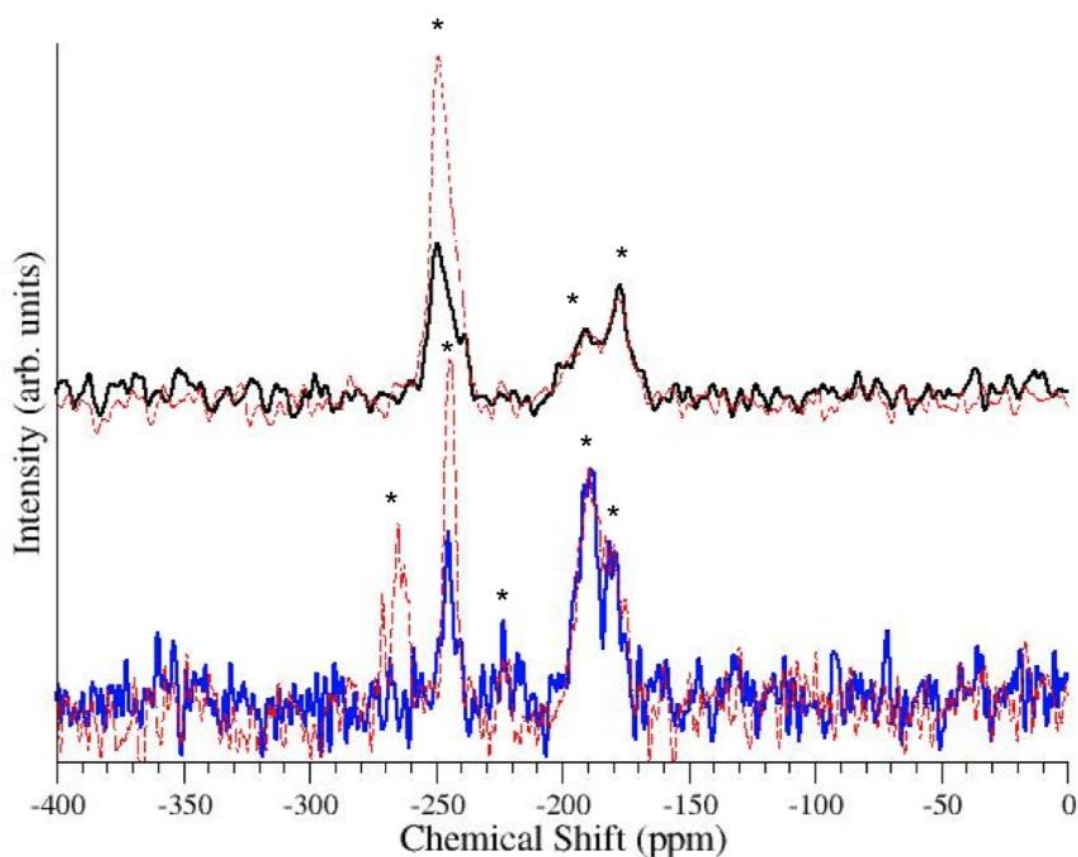
Figure 48: Experimental ¹⁵N CP-MAS NMR chemical shift spectra for carbon nitride materials prepared by ionothermal and thermal method. Continuous spectra (dashed line) are presented with the interrupted decoupling (solid line) spectra. Black = ionothermal sample, Blue = thermal sample, * = chemical shift region of interest

For the I.P sample, the interrupted decoupling showed the chemical shift at -178 and -190 ppm not to be affected, suggesting these N atoms are not directly bonded to H, the chemical shift at -249 ppm decreased by almost half, suggesting that this N atom is attached to a H atom that is not freely rotating, hence there is still some signal that is recorded in this region. For a purely triazine based system we would expect two chemical shifts at -172 and -246 ppm. The -249 ppm resonance can be explained to be due to the N-H bridging group, as predicted by the theoretical

results, which is in line with the interrupted decoupling experimental results. There is a broad region between -170 – -200 ppm, where the most intense resonance is -178 ppm, which again is in line with the triazine-based model. However, the broad signals in this region can be explained by an intercalated system; Li^+ and Cl^- ion intercalation was discussed earlier in this chapter and the experimental findings are in line with the theoretical predictions. The predicted chemical shifts range from $\sim$ -166 – -200 ppm, with most N atoms predicted to give a resonance at $\sim$ -180 ppm. The absence of a resonance at -224 ppm suggests that this structure is not based on heptazine units.

For the Mel sample (which showed the same spectra for the other samples prepared by the thermal method), the chemical shift at -180 and -190 ppm were not affected by interrupted decoupling, whereas the chemical shift at -265 ppm completely disappeared suggesting the presence of a freely rotating NH_2 group, and the chemical shift at -245 ppm was almost halved again suggesting the presence of a N bonded to a H that is not freely rotating. There was also a chemical shift at -225 ppm, this signal was not affected by the decoupling experiment, this resonance is attributed to N bonded to three C atoms in a heptazine based structure. This would also explain the low intensity of the signal as the excitation of a N in such an environment would take longer to appear than the 5 ms contact time used. A longer contact time, we would expect to seen more intense peaks. A heptazine-based structure best fits the experimental data, with the predicted chemical shifts to be -170, -185, -224, -240 and -297 ppm.

6.4.3 ¹H NMR Chemical Shift Results

The ¹H NMR chemical shifts for the ionothermal and thermal material are represented in Figure 49. The thermal sample gives a chemical shift at 9 ppm, with spinning side bands, suggesting that the H giving this signal is part of the extended structure. The ¹H NMR chemical shift for the I.P sample gives rise to two signals at 9 and 11 ppm. The other signals present in both spectra, at ~ 4 to 5 ppm are expected to be due to water, and chemical shifts at 0 to 1 ppm are due to contamination from grease used to load the sample into the probe. We are able to confirm from the experimental NMR spectra that the ¹H signals are due to protons attached to the extended framework of the C-N material.
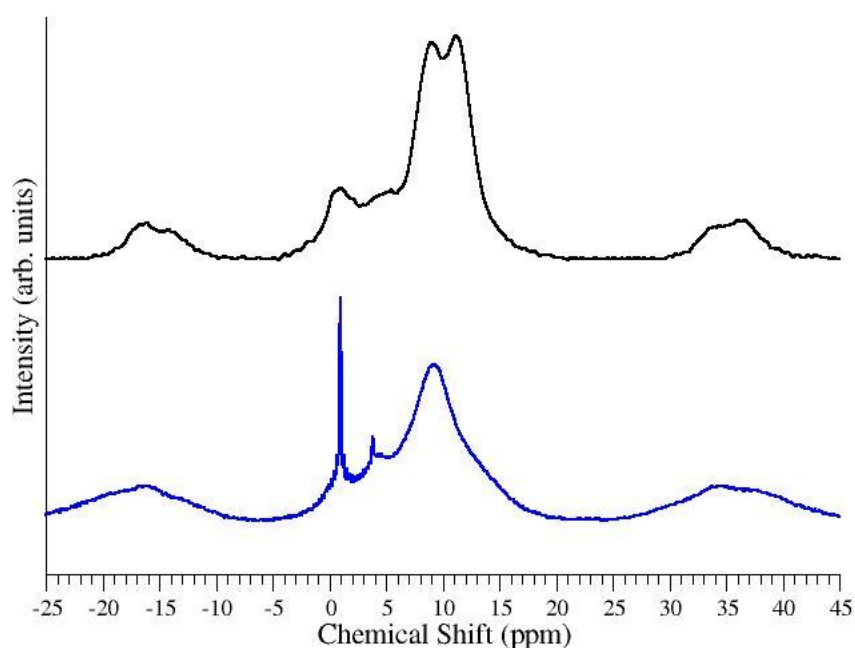
Figure 49: ¹H NMR for carbon nitride materials. Black = ionothermal sample (I.P), Blue = thermal sample (Mel)

6.4.4 Summary of the Experimental NMR Chemical Shifts

Experimentally obtained NMR chemical shifts are tabulated for ^{1}H, ^{13}C and ^{15}N atoms in Table 27. The full data set for the thermal synthesis and the range of C-N materials have been included.

Sample	Experimentally Measured NMR Chemical Shift Values (ppm)		
	[1]H	[13]C	[15]N
I.P	*1, 5,* 9, 11	158, 163, 169	-178, -190, -249*
Mel	*0, 4,* 9	157, 162, 165	-180, -190, -225, -244*, -265*
M.C	*1, 5,* 8	157, 165	-178, -189, -225, -245*, -265*
D.M.C	*1, 4,* 9	157, 162, 165	-178, -189, -227, -244*, -264*
D.M	*1, 4.6,* 9.0	157, 165	-178, -187, -225, -245*, -263*
DCDA	*0, 5,* 9	157, 165	-178, -189, -225, -244*, -264*
'Italic' chemical shifts are not attributed to the sample for ^{1}H NMR *NMR chemical shifts intensity is suppressed upon interrupted decoupling experiments; these atoms are attached to protons			

Table 27: Summary of the experimental CP-MAS ^{1}H, ^{13}C, ^{15}N NMR chemical shifts for carbon nitrides materials prepared using ionothermal and thermal methods

6.5 Conclusion

For the products obtained by the two experimental routes; ionothermal and thermal, it is concluded that the different pathways give rise to two different products. For the former method, the recovered material is mainly based on triazine rings, while the latter method produces material based on heptazine units, either as agglomerates or extended sheets. The experimental results are supported by the theoretical predictions that enable an assignment of the local atomic environments using NMR.

The ionothermal method was reported recently to form a triazine based graphitic structure, intercalated with Li^+ and Cl^- ions [48]. This proposed triazine based model is contrary to the structure originally proposed, based on extended heptazine units [47]. For the ionothermal condensation synthetic attempts, where DCDA was the starting material and a eutectic salt mixture was used as solvent, a well ordered crystalline triazine system is confirmed, as confirmed by the XRD pattern. The material is not completely condensed, as indicated by the presence of the N-H bands in both the IR spectra and the ^{15}N NMR chemical shift at -250 ppm. The experimental results suggest that the presence of ions affect the ^{13}C NMR signal between 158 – 169 ppm. The theoretical predictions presented in this chapter, for NMR chemical shifts calculated for triazine-based systems, intercalated with Li^+ and Cl^- ions are in line with the experimentally obtained results.

The experimental ^{13}C and ^{15}N NMR results presented in this chapter agree with the triazine-based model and are further supported by the theoretical predictions to include the Li^+ and Cl^- ions. The NMR spectra and results for the yellow powder that was separated as the final product, have been presented. It should be noted that there was formation of a darker material, which was not further analysed. Repeating the synthesis to determine the structural arrangement for the darker material would confirm whether the general focus on the yellow C-N compounds is fully justified.

Heptazine is the most plausible building block for the carbon nitride material made by thermal methods. The experimental and theoretical results are in agreement with the known ^{13}C NMR as well as with the ^{15}N NMR. The indication from the above findings is the condensation of heptazine units has begun under the synthetic attempt. However, the removal of the H from the N imido bridges has not been fully completed during the condensation, as shown by the ^{15}N NMR chemical shifts in the regions of $\sim$ -270 and -245 ppm. The presence of N-H bonds is also confirmed by the IR spectra. The proposed structure is the beginnings of a graphitic sheet, however these exist as small heptazine agglomerates due to the significant intensity of the NH_2 chemical shift, at -270 ppm.

Chapter 7

NMR Calculations for Planetary Tholins; Another form of Carbon Nitride Species

7.1 Introduction

C-N materials are an area of interest for planetary geology, especially for Titan's tholins. Titan, the largest moon of Saturn shrouded by a haze, is the only natural satellite to have a dense atmosphere and has for a long time been predicted to have oceans or lakes due to the stability of liquid methane at the surface [110, 111]. In our solar system Titan is the only other known entity that provides clear evidence of stable surface liquids [112]. There was strong evidence after the interpretation of the results collected by the Cassini Radar flyby of Titan in July 2006 that condensable liquid hydrological cycles is active, where the lakes are filled by rainfall of some description. Titan's tholins are N-rich organic solids that are formed on icy surfaces, produced by the reactions between C_2H_6/CH_4 and N_2 upon radiation of ultraviolet light, and these organic solids are thought to be responsible for the characteristic reddish haze of tholins. The word tholin is derived from the Greek term for 'muddy', and has been named as such due to the appearance and description of the hazy mixture of organic compounds [113]. The atmosphere of Titan is thought to be mainly N_2 and only a few percent CH_4, with trace amounts of

other gases. A schematic of the chemical reaction that takes place is represented in Figure 50.

Titan is thought to be one of the planetary bodies in our solar system that could potentially support life; as a result the atmospheric chemistry has received considerable attention, especially following the Cassini-Huygens missions that returned new spectroscopic data about the environment.
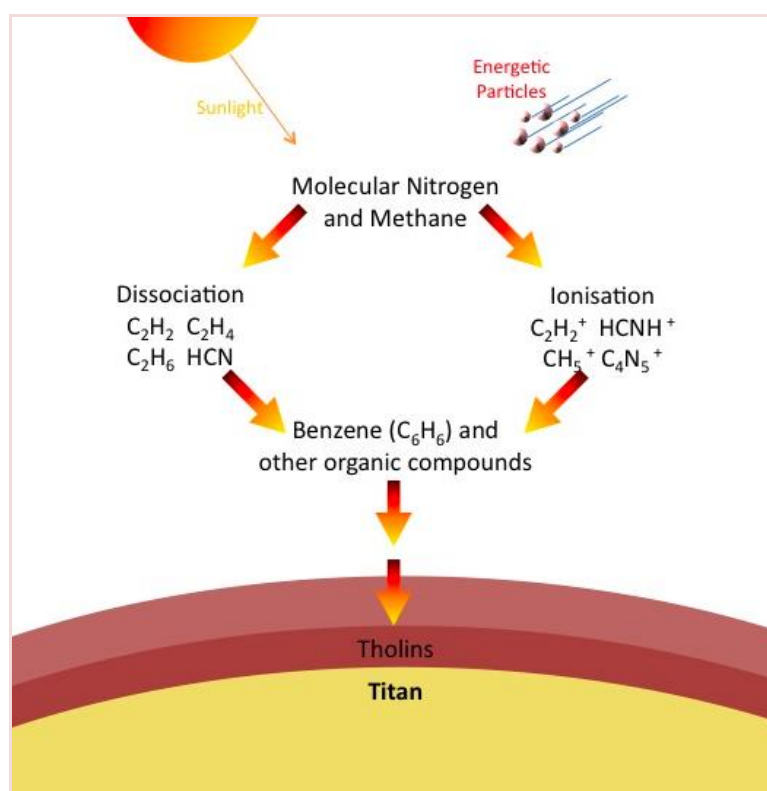
Figure 50: Chemical reactions taking place in the atmosphere of Titan [114]

The pressure at which tholin species form affect the positioning of the N atom in the compound, where high pressures are more likely to result in terminal N positions. Experiments attempting to simulate Titan's atmosphere have been

conducted in several laboratories, aiming to predict the aerosol analogues. Irradiation of a gaseous mixture is the basis of the experimental set up [115, 116].

During this PhD thesis and study of C-N materials, we entered into a collaborative project with Dr Sylvie Derenne from the Biogeochemistry and Ecology Of Continental Environments, France. Dr Derenne was responsible for leading a study to synthesise Tholin species in the laboratory, which were then characterised using NMR techniques. We were able to contribute heavily to this experimental study with our theoretical predictions for the ^{13}C and ^{15}N NMR chemical shifts, allowing for a clearer interpretation of the experimental results [117].

This area of research focused on the assignment of carbon nitride environments expected to be present in Tholin species. The theoretical predictions on carbon nitride materials supported the assignment of experimental NMR chemical shifts. The analysis of these results guided the understanding, by providing new information on the connectivity of the C, N and H nuclei within the structure for the reported $C_xN_yH_z$ materials. These findings have been published in Icarus [117].

7.2 Investigating Tholin Species Using NMR

Tholin species are organic compounds that are produced in the laboratory and are considered to provide materials analogous to those responsible for the haze observed in Titan's atmosphere. In the upper atmosphere, methane and nitrogen molecules undergo dissociation under the influence of solar UV radiation and

electron impacts, followed by recombination reactions leasing to a large variety of organic molecules [118]. Astrobiological interest exists due to the ability of tholin species to release amino acids upon hydrolysis [119, 120] and nucleobase after X-ray irradiation [121]. Tholin's chemical structure have been investigated using a number of techniques, these range from bulk elemental analysis [122-124], pyrolysis [125-127] and laser desorption mass spectrometry experiments [128] to infrared absorption, visible UV and near-IR Raman and luminescence spectroscopy [122, 129, 130], XRD and high resolution transmission electron microscopy [122]. However, to date no detailed NMR studies has been performed on these materials despite the potential for this technique to investigate the local environment of a given nuclei. In 1993 a preliminary solid-state ^{13}C NMR study of tholins was reported [131]. In the study for this PhD thesis both ^{13}C and ^{15}N solid-state NMR spectroscopy was applied experimentally to obtain new insights into the chemical structure of tholin species.

To gain insight into the chemical composition and structural nature of these complex organic compounds, analogous materials are produced in the laboratory using plasma discharge methods, in gaseous N_2 – CH_4 mixtures that are designed to simulate Titan's atmosphere [115, 116, 132].

The theoretical predictions were used to guide the understanding of the experimentally obtained data, as it was compared to a number of carbon nitride structures, to explain the species present. Experimentally Tholin species were

produced through plasma discharge in gaseous N_2–CH_4 mixtures, which were designed to simulate the atmosphere of Titan.

7.2.1 Theoretical Method for Modeling Tholins

To model NMR shifts for certain species, individual molecules or molecular fragment, a large unit cell was constructed using Materials Study. The unit cell contained a single molecular fragment that was sufficiently distant from any neighbours to eliminate possible interaction effects. As for the scaling of NMR shifts, all calculations used the PBE exchange correlation functional with ultrasoft pseudopotentials for the atoms involved. Prior to the calculation of NMR shielding parameters, full geometry optimizations were carried out, with all atoms and unit cell parameters allowed to relax. Molecular systems simulated using periodic boundary conditions were fully optimised within a fixed unit cell of sufficient size to ensure that interactions between the periodic images of the molecule were negligible. For this study a number of cut off energies and k-point spacing were tried, k-point spacing of 0.04 $Å^{-1}$ and cut-off energy of 600 eV provided suitable convergence for the various C-N-H structures considered, including pyridine, pyrimidine and substituted triazines. The calculations were repeated at higher cut off energy (700 eV), but the improvement in chemical shifts was very small, at ~0.4 ppm. A summary of structures is represented below in Table 28, where the chemical shifts have been grouped in terms of the functional group.

Functional group	Experimental Chemical Shifts (ppm) ^{13}C	^{15}N	Occurrence in tholin sample	Structures simulated theoretically	Theoretical Chemical Shifts (ppm) ^{13}C	^{15}N
Nitriles -CN	121	-134	**Present**	H-CN	120	-144
				H$_3$C-CN	124	-131
				H$_2$N-CN	118	-184
				Benzene-CN *	114	-111
				Triazine-CN *	124	-108
Amines -C-N	44	-300 to -330	**Present**, most likely linked to sp^2-bonded C, possibly in heterocyclic structures	Melamine	165	-219, -329
				Heptazine	154, 162	-238, -313
				3-Heptazine	156, 161 to 163	-160, -182, -222, -246 -304
				H$_3$C-NH$_2$	30	-388
Methyl -CH$_3$	26	-	**Present**	H$_3$C-NH$_2$	30	-
				H$_3$C-CN	2	-
				H$_3$C-NC≡N-CH$_3$	34	-
				H$_3$C-NC-H	42	-
				Hexamethylbenzene	18	-
sp^2 carbons, imines C=C and/or C=N	140 to 180	-185 to -285	**Present**	H$_2$C=CH$_2$	124	-
				Benzene	128	-
				H-N=C=N-H	145	-324
				H$_3$C-N=C=N-CH$_3$	130	-319
Isocyano -NC	160	-200	*Possible* but *minor*	H-NC	175	-240
				H$_3$C-NC-H	206	-94
				H-NC-H	226	-84
				Melamine-NC **	161	-188
				Triazine-NC ***	180	-193
*H substitution with CN, **NH$_2$ substitution with NC, ***H substitution with NC						

Table 28 part 1/2: Summary of the occurrence of the structural units of the tholin sample with the experimental and theoretical range

Functional group	Experimental Chemical Shifts (ppm) 13C	15N	Occurrence in tholin sample	Structures simulated theoretically	Theoretical Chemical Shifts (ppm) 13C	15N
Heterocyclic amine	-	-356	*Possible*	Triazine based	61	-334
				Pyridine based	29 to 51	-336
				Pyrimidine based	35 to 67	-327
				Cyclohexane	10	-
C=C-CN			Possible	$H_2C^a=C^bH-C^cN$	140[a] 111[b] 126[c]	-102
				$H_2C^a=C^b-C^cN$	96[a] 190[b] 129[c]	32
Heptazine (see structure **IV**)	ca.160	-185 and -240	Possible	H_2N-C 3NC (outer N) 3CN (central N)	162 154 154	-313 -198 -238
Aromatic Hydrocarbons	100 to 140	-	Possible but minor and mostly non-protonated	Benzene	128	-
				Hexamethylbenzene	131	-
				Cyclohexane	10	-
*H substitution with CN, **NH2 substitution with NC, ***H substitution with NC						

Table 28 part 2/2: Summary of the occurrence of the structural units of the tholin sample with the experimental and theoretical range

7.2.2 Interpreting 13C NMR Chemical Shifts

A dominant peak at 140-180 ppm was observed for the tholin species. This chemical shift region could be explained by the substantial contributions from heterocyclic aromatic species containing triazine (C_3N_3) rings and heptazine (C_6N_7) units, as well as 13C resonances affected by the presence of N-H bonding. The theoretical predictions confirmed the assignments, as listed in Table 28, where a

broad signal was recorded to extend between 5-100 ppm due to aliphatic carbons, and a well-resolved peak at 121 ppm was assigned to the presence of a nitrile species (-C≡N). The experimentally obtained ^{13}C NMR chemical shift spectra is represented in Figure 51.

Figure 51: (a) ^{13}C Magic Angle Spinning NMR Chemical Shift Spectra of the Tholin sample (b) ^{13}C Cross Polarisation Magic Angle Spinning NMR Chemical Shift Spectra of the tholin sample, with varying contact times, from 0.5 – 5 ms. (* spinning sidebands)

Within the range of the 140-200 ppm signal, there were two peaks that were clearly present at 160 and 168 ppm. Contact time experiments showed the carbon

atoms responsible for the 168 ppm peak were more protonated than those responsible for the 160 ppm signal. Carbon atoms adjacent to nitrogen in six-membered heterocycles including triazine and its derivatives have chemical shifts ranging between 140-170 ppm and the resonances become more deshielded when the C atoms are substituted by aliphatic or amino groups [133]. For example, C atoms adjacent to N in pyridine and pyrimidine exhibit chemical shifts of 151 and 158 ppm, respectively, theoretically calculated to be 150 and 157 ppm respectively. These resonances shift to 160 and 167 when the heterocycle is substituted by a methyl or an amino group. C in triazine and in its triamino derivative (i.e., melamine) is characterized by a chemical shift of 167 ppm, theoretically calculated to be 168 and 165 ppm respectively. It has previously been reported [134] that the central carbon atom in dicyandiamide ($C_2N_4H_4$: NH_2-C(=NH)-NH-C≡N) exhibits a ^{13}C chemical shift at 163 ppm. Our theoretical results combined with experimental observations indicate that it is not possible to discriminate between imine carbons occurring in straight chains vs heterocyclic environments using ^{13}C NMR spectroscopy alone.

Our theoretical calculations support these assignments for various species that are possibly or probably present within the tholin sample. For melamine, the isotropic ^{13}C NMR shift occurs at 165 ppm in the molecular solid, and in an extended graphitic melamine framework modeled in this study the chemical shift is calculated to occur at 162 ppm. Another potential assignment for the 160 ppm peak results from the possible presence of isocyano groups (-N≡C). The broad background signal between 100-140 ppm likely indicates a small contribution

from other aromatic carbon species present in the sample. Their behaviour in the variable contact time experiment is similar to that of the nitrile peak, suggesting that these C sites are mainly non-protonated.

The DFT calculation results indicate values for ^{13}C shifts for the central carbon in CH$_3$C≡N and H-C≡N species to be between 119-124 ppm; for N=CH$_2$ species, the ^{13}C chemical shift occurs at 146 ppm. The effect of substitution of H by other functional groups in R-C≡N systems associated with an aromatic carbon system, such as benzene, was also investigated in our theoretical studies and a chemical shift value near 114 ppm was predicted for the central carbon in these species. The effects of substituting the H substituents within melamine and s-triazine derivatives was investigated, where the ^{13}C NMR chemical shift for the attached carbons were predicted to occur at 126 ppm and 124 ppm respectively. The effect of adding an amine function attached to the nitrile group (N≡C-NH$_2$) was studied: here the expected chemical shift would lie at approximately 118 ppm (Table 30).

7.2.3 Interpreting ^{15}N NMR Chemical Shifts

The experimentally obtained ^{15}N NMR chemical shift spectra are represented in Figure 52. The experimental results show a main broad peak between -230 to -340 ppm with maxima at -272 ppm and -304 ppm, along with two shoulders at -330 and -256 ppm. An additional broad signal between -180 to -260 ppm range with maxima near -185 ppm and -170 ppm, as well as an additional broad feature at ~-134 ppm. There is also a sharp peak at -356 ppm. This falls within an unusual range for ^{15}N chemical shifts. Heterocyclic amines might account for this

observation, but ammonium or hydrazinium ions located close to polynitrogen chains such as azides have also been reported to exhibit such anomalously negative chemical shift values [135, 136].
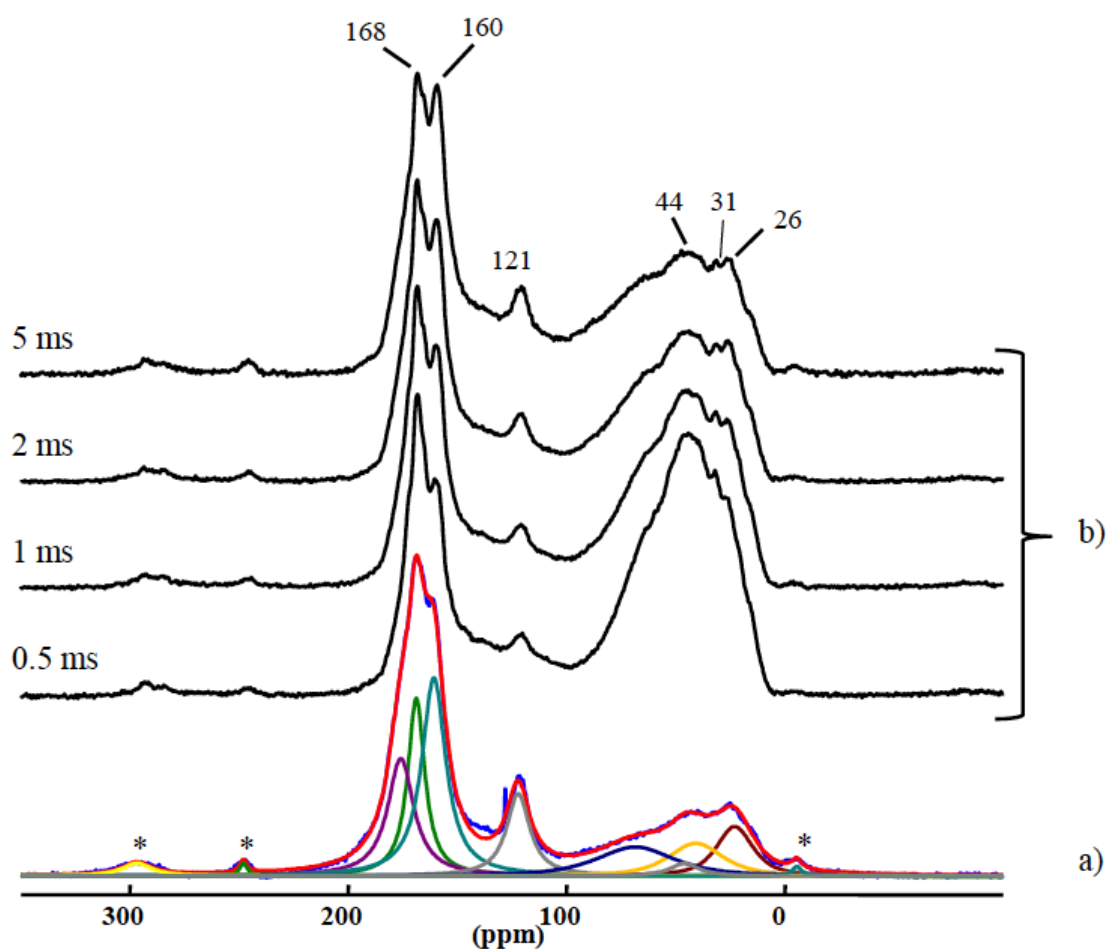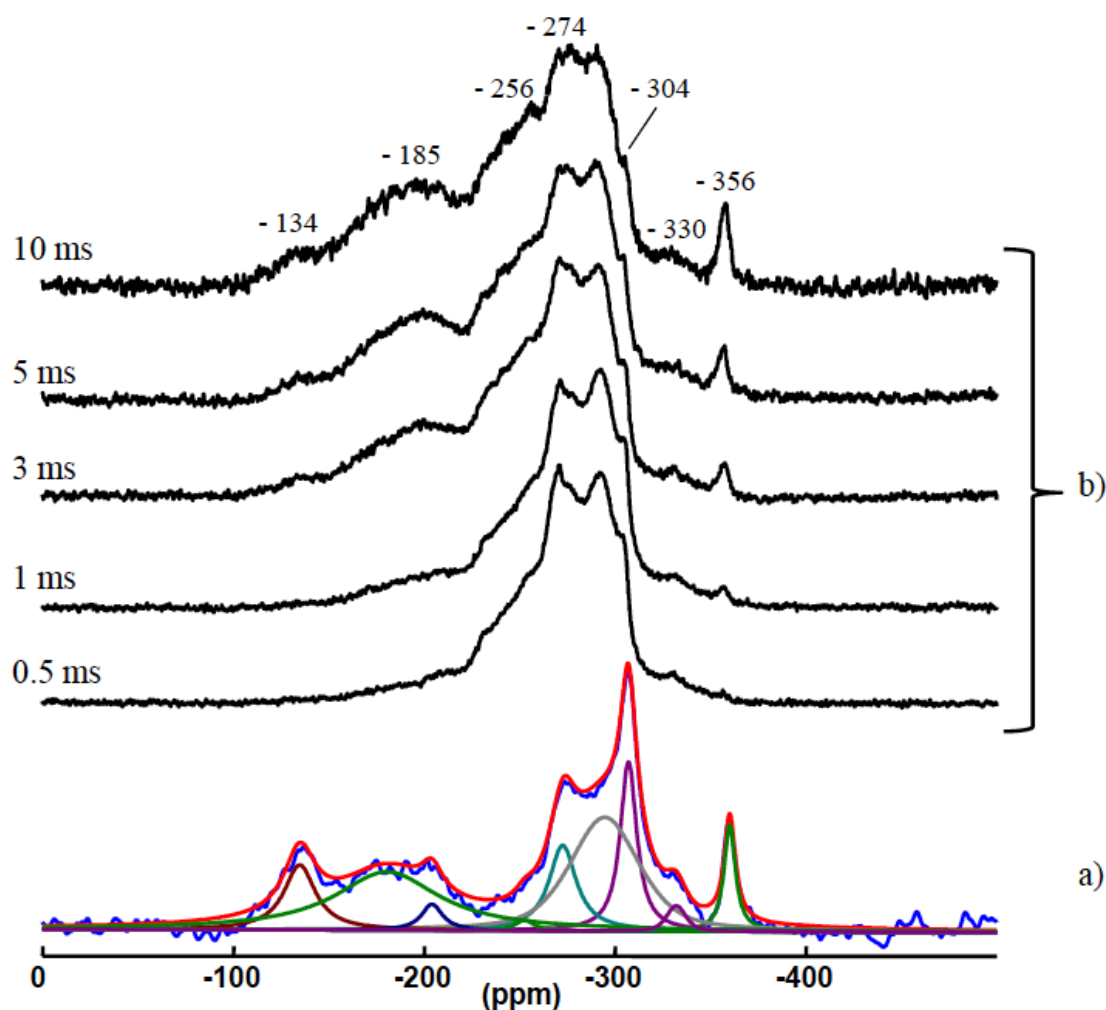

Figure 52: (a) ^{15}N Magic Angle Spinning NMR Chemical Shift Spectra of the Tholin sample, in ppm (b) ^{13}N Cross Polarisation Magic Angle Spinning NMR Chemical Shift Spectra of the tholin sample, in ppm. Varying contact times recorded for the sample, from 0.5 – 10 ms.

The low efficiency of CP dynamics for the peak at -356 ppm observed in this study may be explained by the presence of NH_4^+ groups in the sample combined with

their expected rotational motion. That assignment is supported by the theoretical results that predict a ^{15}N shift for ammonium species at -350 ppm (Table 28). The main peaks are centered around -274 ppm corresponds to positions usually assigned to nitrile species, whereas -330 ppm is a typical chemical shift for amines. Both of these species were indicated to be present in the tholin sample from ^{13}C NMR spectroscopy results discussed above, supported by the theoretical results.

Based on ^{13}C chemical shift data, contributions from six-membered heterocycles were considered to be present. This might initially seem to disagree with the observed ^{15}N chemical shifts, as values of -63 ppm, -85 ppm and -103 ppm have been reported for pyridine, pyrimidine and triazine, respectively. However, it has also been observed that substitution by amino groups induces a strong shift towards more negative values (-190 and -207 ppm for 2,4,6 triamino-pyrimidine and -triazine, respectively) and that the chemical shift for the amino group in such compounds occurs at around -300 ppm [137]. Our DFT calculations indicate that the $-NH_2$ groups in melamine give rise to a chemical shift at - 329 ppm, whereas the aromatic N species incorporated in the triazine rings leads to a signal at -219 ppm. Similar shifts were reported for 2-exo-cyanomethylene substituted quinazolines and their cyanoimino analogues where values of -274 and -285 ppm were recorded for the N atoms [138]. Interestingly, the carbon atom located between the two N atoms in the heterocycle exhibited ^{13}C shifts of 156-158 ppm, similar to the values observed for the tholin sample.

15N chemical shifts at around -280 ppm have also been reported to occur for N atoms contained within carbodiimide structures (-N=C=N-) that become shifted to -297 ppm when an additional amino group is present on the side chain [137]. However, in such structures the corresponding chemical shift of the central C atom occurs at ~140 ppm, that is absent from the 13C CP MAS spectra of the tholin sample. This result indicates that such species are absent from our material.

13C chemical shifts recorded for melem containing triazine and heptazine units were similar to those observed for the tholin sample [21] and so the corresponding 15N shifts for molecular units associated with these species were examined. Previously reported chemical shifts suggest N atoms located at the periphery of the condensed rings give rise to an intense signal at -200 ppm, whereas the central N is observed to resonate at -238 ppm (Table 28). In our work the simulated 15N chemical shifts for the heptazine (molecular unit for melem) yielded three values, with the amine group occurring at -313 ppm, the central N at -238 ppm and outer N atoms in the traizine ring at -198 ppm. These results are consistent with the theory that heptazine units are present within the tholin sample. Amino groups from local groups such as those exisiting in melem are also detected at -267 and -281 ppm [21].

The experimental results indicate the most efficient CP dynamics for 15N resonances occurring in the -270 to -295 ppm range, compared with the resonances in the -134 to -198 ppm range that showed a rather slow polarization transfer. The minor -134 ppm peak can be assigned to nitrile groups observed

above by ^{13}C NMR. Chemical shifts around -200 ppm are observed for N in isocyano groups, which may correspond to the weak ^{13}C signal observed near 160 ppm.

7.3 Conclusion of Tholin Study

To summarize, these ^{13}C NMR experiments combined with the DFT predictions reveal the presence of mainly protonated aliphatic carbons, present within the tholin sample. Some of the aliphatic carbons are linked to N incorporated within amine functional groups and others are clearly involved in methyl species. The occurrence of nitrile groups within the tholin sample is also evident. The dominant ^{13}C NMR signal can be assigned to sp^2 carbons linked to N within heterocyclic units although a contribution from isocyano groups cannot be excluded. A minor contribution of non-protonated aromatic carbons could also be present.

These ^{15}N NMR experiments confirm the presence of nitrile and amine groups in the tholin sample. The occurrence of isocyano groups is consistent with the ^{13}C NMR data, along with a low contribution of carbodiimide entities to the NMR spectra. The occurrence of amino-substituted six-membered heterocycles is supported by resonances both in the range of the amino substituents and of the imino functions from the rings, although other types of substituents (such as some bearing cyano groups) might also be present in variable quantities.

This comprehensive NMR study where both experiment and theory have been utilized has allowed the elucidation and confirmation of structural units and

functional groups. Theoretical NMR predictions have played an important role in guiding the understanding of the connectivity that may be present in Tholin samples.

Chapter 8

Conclusion

The work presented in this thesis was performed during my PhD. The initial focus was on understanding the nature and properties of dense and graphitic carbon nitride materials, using computational methods. Over the course of the PhD, a number of synthetic and analytic experiments have been performed, either in collaboration or independently. In chapters three to seven the experimental data have been better understood and supported by the corresponding DFT calculations.

In chapter one we discussed the background to carbon nitride materials and considered the reasons for renewed interest in these materials in the past 20 years. We talked about the initial discovery, nature of the material, synthetic methods, as well as the uses and applications. We explored the differences between the graphitic and dense carbon nitrides and the general properties of these materials. This introduction was concluded by summarising the reasons as to why further research into carbon nitrides materials is still of great scientific importance and interest.

In chapter two we presented the methods used to conduct the research in this thesis. We talked about the background upon which the theory was based as well as the two different DFT based computational codes used; CASTEP and CRYSTAL, and we explained our choices for using these codes for the investigations set out in this thesis. In this chapter we explained the use of a structure searching method (AIRSS), to find new plausible C-N-H structures, for which we carried out further theoretical investigations such as generating the XRD patterns. We also explained the necessity for theoretically generated NMR chemical shifts, to aid the interpretation of the experimental NMR for C-Ns.

In chapter three we investigated the proton ordering for a dense nanocrystalline carbon nitride material with a defective wurtzite structure and C_2N_3H stoichiometry. Such information could not be obtained from the experimental data available; XRD patterns and Raman spectra. Our theoretical investigations identified the preferred orientation of the H, and the effect on the over all stability of the structure. We found that C-N defective wurtzite structure was extremely stable, although there was a preferred H orientation; there was very little difference in energy between the polymorphs.

In chapter four we discussed the results obtained, from using the relatively new structure searching method, for the C_2N_3H stoichiometry. We had employed the AIRSS method to identify a polymorph that was thought to exist at high pressures during the synthesis of the C_2N_3H defective wurtzite material, discussed in the previous chapter. Our primary source of comparison was the experimental XRD

pattern, for which we hoped to fit XRD data with a new predicted structure. We tried a number of different search techniques using the AIRSS method, and from the search where we found the structure known to exist (C_2N_3H defective wurtzite) we then investigated the other low energy structures found in the same energy landscape. We were able to identify the most plausible polymorph that existed at high pressures, and was consistent with the XRD pattern obtained from the experimental data. The structure made chemical sense as it was based on the same motif as found in defective wurtzite and the issue of stability could be explained by stacking arrangements, where we identified that AAA stacking was less stable than ABA (the latter was the recovered defective wurtzite material).

In chapter five we began by presenting calculated NMR chemical shifts for a number of C-N compounds and derived scaling equations for ^{13}C and ^{15}N chemical shifts to optimise the agreement between calculated and experimental results. We modeled both molecular and extended crystalline structures, and determined the scaling factors for ^{13}C and ^{15}N NMR chemical shifts. The NMR chemical shifts were predicted and the scaling formula applied to C-N starting materials and structures along the DCDA condensation pathway. These predicted chemical shifts are useful reference values for C-N solid-state materials, which have been used to understand the synthesised material in the chapter six.

In chapter six we used theoretical NMR predictions on extended carbon nitride materials prepared by ionothermal and thermal synthetic methods. The experimental data, elemental analysis, XRD patterns and IR could not provide

precise answers as to the structural connectivity, or the type of triazine rings that had formed i.e. melamine verses heptazine. The experimental NMR, although extremely useful at determining the local atom environment, without the aid of theoretical predictions could not be used to specifically determine the corresponding chemical shifts and the type of triazine structure present. We demonstrated the importance of theoretical NMR chemical shifts to guide the characterisation of these particular carbon nitride materials. During this part of the C-N investigations in this PhD thesis we were able to determine important information; the results support the suggestion that the thermal method gave rise to heptazine-based materials and the ionothermal method gave rise to predominantly triazine-based materials, with the indication that a heptazine based material may also form during the synthesis.

In chapter seven, we presented the results of a collaborative effort into the investigation of Titan's Tholin. In this chapter we described how our theoretical NMR predictions helped our understanding and allowed for better interpretation of experimental NMR chemical shifts for synthesised Tholins and C-N-H fragments.

Using the latest available techniques in computational methods, we have been able to contribute to solid-state carbon nitride chemistry. Work carried out in this thesis has enabled us to better understand the synthetic pathways. The ability to model a structure that is expected to have formed, allows the researcher to predict theoretically generated data that can be directly compared with the experimentally obtained data. Our theoretical predictions have guided our understanding and

allowed for better interpretation of the experimental results, in our C-N investigations.

Chapter 9

Further Work

Carbon nitride chemistry will no doubt continue to be of great scientific interest for many years to come. The potential for finding a low compressible binary carbon nitride material would hold huge potential for numerous industrial applications. Although the equivalent to β-Si_3N_4 has not yet been unambiguously synthesised, the general attempt to try and take the graphitic carbon nitride materials and compress them into a dense crystalline form (similar to the graphite to diamond phase transition) is still a plausible method that requires further investigations, both experimentally and theoretically.

The recent discovery of the photocatalytic activity of C-N materials is of significant importance. Our work in this thesis has been able to understand the structural information surrounding the carbon nitride materials that were found to be photocatalytically active [109]; the heptazine based structures were found to be active. This important property of the versatile C-N material requires further investigation as to the mode of action in which the photocatalysis takes place, which at present is not fully understood.

A particularly useful set of further investigations is the modeling of graphitic structures that comprise of heptazine and melamine units. Thus far the focus has been on heptazine based sheets or melamine based sheets, but not the two together, therefore an investigation that would combine both the building blocks into one model would be a new avenue to pursue in understanding the C-N materials even further. There are a number of triazine-heptazine combinations that could arise, by varying the amount of each ring in the structure, and understanding the effects on the predicted NMR chemical shifts and the IR spectra could prove to offer new useful information.

The AIRSS method provided a number of potentially new carbon nitride structures for which further investigations would be useful to obtain predicted experimental spectra on these materials. Prediction of the Raman spectra is an extremely expensive calculation to run, however for each of the low energy structures from the individual searches, this would be useful new data to obtain for which a number of computational codes now offer this capability.

Appendix 1

Ionothermal and Thermal Experimental Method for Carbon Nitride Synthesis

A1.1 Preparation of Graphitic Carbon Nitrides

For a full and detailed investigation of graphitic C-N it became important to synthesise new samples for the NMR experiments and theoretical predictions. The preparation of the ionothermal sample was in collaboration with Dr Ana Belen in the McMillan group at UCL. The thermal samples were prepared independently.

Graphitic C-N materials were prepared by two main methods. First was using an **ionothermal preparation** as described by Bojdys *et al* [47], where the starting material was placed in a sealed steel capsule (Figure A1.1) with a mix of salts e.g. Li/KCl or Li/KBr and heated until all three components formed a molten mixture (400 °C), after cooling the yellow product was heated to higher temperatures (600 °C) in a sealed quartz tube (Figure A1.2) where the NH_3 (g) evolved, which was confirmed by a popping sound upon opening of the sealed vessel and the distinct smell of NH_3 (g). When the samples were recovered from the ionothermal preparation the material had formed a porous yellow solid. The recovered material was washed with distilled water at ambient conditions, to dissolve the

salts present. The resulting solution was centrifuged, the salt water was decanted and the remaining solid was dried for 24 hours under vacuum at 250 °C.
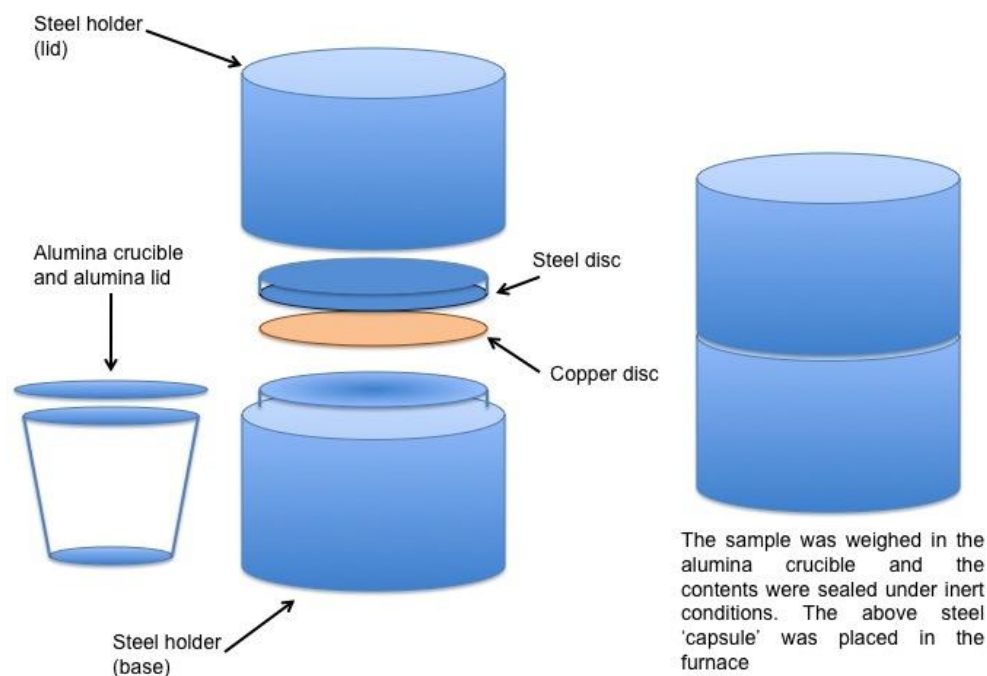

Figure A1.1: Steel capsule used to heat the samples

Figure A1.2: Sealed quartz tube containing yellow sample

A method similar to the Wang *et al* synthesis, reported in Nature [14], was used to prepare a number of new samples and is described as **thermal preparation**.

Equal ratios of starting materials (DCDA, melamine, cyanuric chloride) were weighed in an alumina crucible and sealed under inert conditions in a sealed steel vessel, which was then heated to high temperatures (400 – 600 °C) for 16-hours. Each recovered mixture resulted in a yellow powder.   The sample was recovered from the alumina crucible in the steel holder; the material formed varying sized agglomerates of yellow solid material (Figure A1.3 and A1.4).

Figure A1.3: Alumina crucible containing the recovered sample after heating

Figure A1.4: Recovered yellow sample from the alumina crucible

The SEM images obtained for all the samples prepared using this method confirmed the materials had formed coarse layered sheets of varying sizes (Figure

A1.5 and A1.6); supporting the understanding that we already had material with a graphitic arrangement. We have represented the SEM images for the sample that used a mixture of the starting materials DCDA and melamine, synthesised by this method, all other preparations gave similar SEM images.
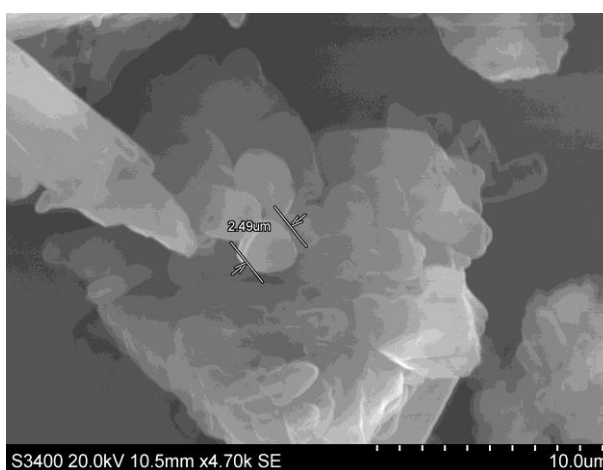

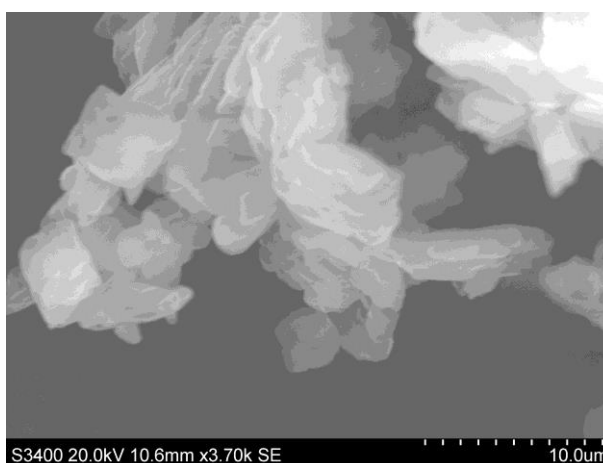**Figure A1.5: SEM image of recovered sample**

Figure A1.6: SEM image showing layering of recovered sample

Table A1.1 summarises the different experimental conditions for all synthesised products and the starting materials used

Sample Name	Reactants	Conditions	Temperature (°C)	Time (hours)
M.C (1:1)±	Melamine, Cyanuric Chloride	Sealed steel vessel under inert conditions	400 – 600	16
D.M.C (1:1:1)±	DCDA, Melamine, Cyanuric Chloride	Sealed steel vessel under inert conditions	400 – 600	16
D.M (1:1)±	DCDA, Melamine	Sealed steel vessel under inert conditions	400 – 600	16
DCDA	DCDA	Sealed steel vessel under inert conditions	400 – 600	16
Mel	Melamine	Sealed steel vessel under inert conditions	400 – 600	16
I.P*	LiCl, KCl, DCDA	Sealed steel vessel under inert conditions and then sealed in quartz tube under vacuum for second heating	400 and then 600	6 and then 12
M = melamine, C = cyanuric chloride, DCDA = dicyandiaminde, Mel=melamine ±= ratio used for starting materials *I.P = only sample prepared by the ionothermal preparation				

Table A1.1: Summary of the synthetic techniques detailing the experimental conditions

A1.2 Complimentary Experimental Results

A1.2.1 Bulk Composition Analysis and XRD pattern

The composition of the materials were analysed using elemental analysis at UCL, for which the results have been summarized in Table A1.2. The weight percentage does not equal 100 % for the C, N and H atoms, which implies there is another element present in the material. This may be explained by the presence of ions from salts used in the synthesis, or ions present in the starting materials.

Sample Name	C, N, H Weight %	Proposed Stoichiometry
M.C	26.0, 46.5, 3.8	$C_{0.7}N_1H_{1.2}$
D.M.C	35.0, 61.3, 1.5	$C_{0.7}N_1H_{0.3}$
I.P	29.6, 45.8, 1.3	$C_{0.8}N_1H_{0.4}$
D.M	33.8, 59.9, 1.6	$C_{0.7}N_1H_{0.4}$
DCDA	33.9, 59.9, 1.6	$C_{0.7}N_1H_{0.4}$
Mel	34.2, 58.5, 1.5	$C_{0.7}N_1H_{0.4}$

Table A1.2: Elemental analysis of the different graphitic C-N materials

An initial characterization of the material structure was made, by obtaining the XRD pattern for each material, as represented in Figure A1.7 and A1.8. The samples M.C, D.M.C, D.M, DCDA and Mel all gave similar XRD patterns and showed that all the materials were graphitic in arrangement. The Mel sample has been represented in Figure A1.7 as this sample gave the sharpest peaks. The XRD pattern was analogous to that reported in the literature by Wang *et al*. These materials are characterised by diffraction peaks at 2θ values of 13° and 27° and hence supported the theory that the materials made by these methods were graphitic in nature. The I.P material gave rise to a more crystalline XRD pattern, presented in Figure A1.8 with 2θ values at 11.5°, 21.5°, 25°, 27°, 29°, 32.5°, 43°, 44°, 52.5° and 55.5°, suggesting a more ordered crystalline material had been synthesised.

The poor crystalline nature of these samples prevented a complete structural solution from the XRD patterns alone. Further structure elucidation was necessary, to determine the exact structural arrangement.
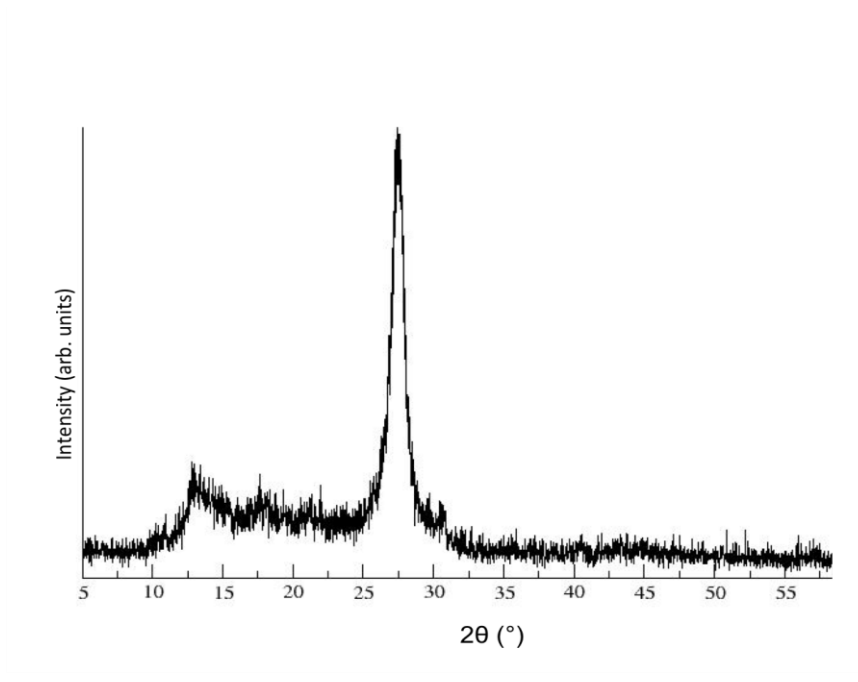
Figure A1.7: XRD pattern for Mel graphitic C-N material obtained by thermal preparation
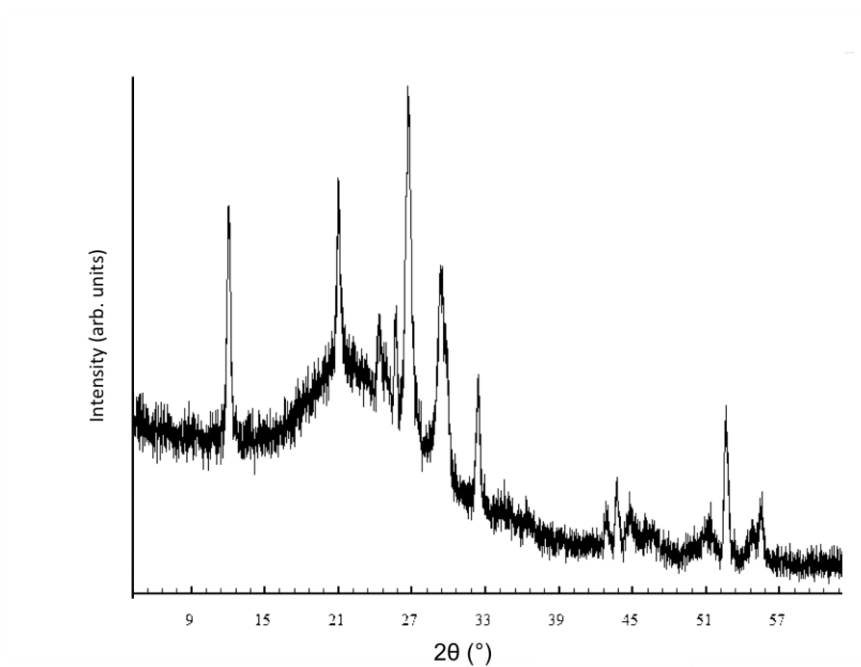

Figure A1.8: XRD pattern for I.P crystalline C-N material (I.P) obtained by ionothermal preparation

A1.2.2 Bond Characterisation by Infrared Spectroscopy

The infrared spectra (IR), as represented in Figure A1.9 was similar for all the samples prepared by the thermal method, and so only one spectra (Mel) for these materials is represented. The IR spectra provided the first indication of the presence of the carbon nitride bonds in all samples synthesised, the spectra confirmed that water was absent in all the materials and highlighted the presence of N-H species with the characteristic wavenumber present at $3100 - 3300$ cm^{-1} in all materials synthesised. The N-H stretch highlighted that H had not been fully eliminated during either of the reaction pathways.

IR signals at $1200 - 1600$ cm^{-1} indicate the presence of a s-triazine ring, these shifts were present in all the C-N materials synthesised. A vibration signal observed at 690 cm^{-1} confirms the presence of a triazine ring, as this region is the confirmation of the presence of the breathing mode of the triazine ring [47]. The IR spectra, although specific to a particular structure and useful at indicating the bond types present were not able to determine detailed structural information, i.e. which particular types of condensed C-N rings were present as the 'building block', melamine or heptazine.

As some of the sample preparations contained chlorine, as either the starting material (cyanuric chloride) or as a salt (LiCl/KCl), it was possible that there was chlorine present in the final product. The presence of chlorine atoms in these systems would affect the IR frequency values, since the interaction with hydrogen would cause hydrogen bonding, thus resulting in lowering the frequency of N-H

stretching mode. As the IR spectra were found to be similar for the samples prepared using the thermal synthetic method, only differing by the starting materials used, of which not all contain chlorine, we do not expect chlorine to be present (in large enough quantities) in the final product for the materials. For the I.P sample, however, it is possible that 'washing out' the chlorine atoms in the final step, when recovering the sample may not have been completely effective, as the N-H stretch is broad, when compared with the thermal sample. This may also be explained by better elimination of protons from the I.P material, hence fewer N-H bonds.
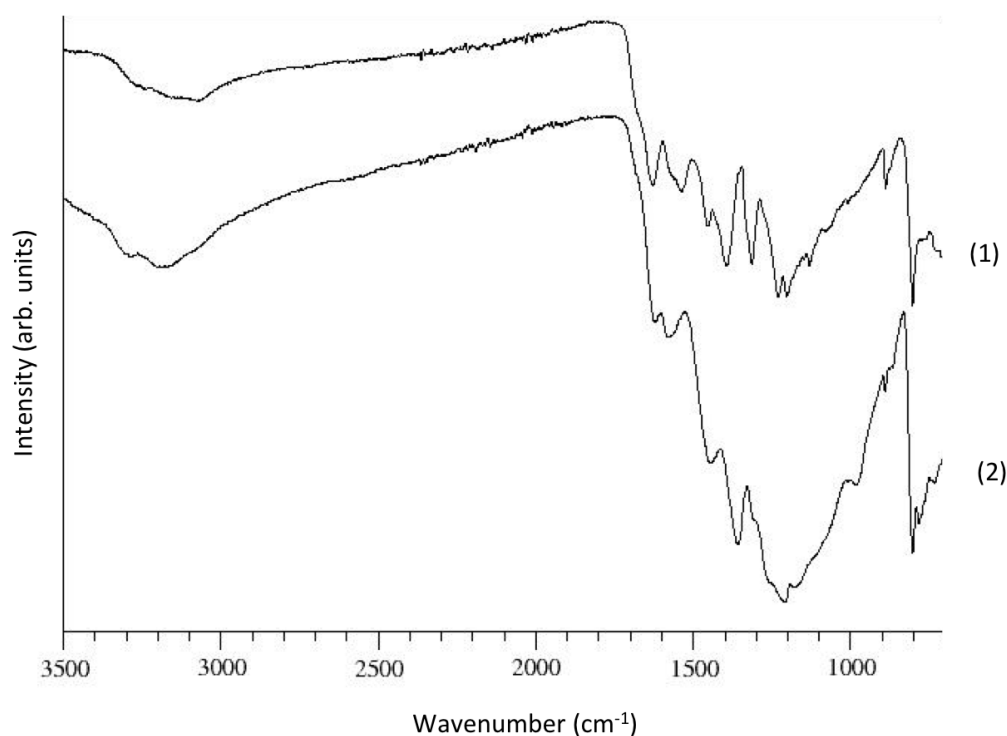

Figure A1.9: IR Spectra for synthesised C-N materials, the spectra correspond to (1) ionothermal preparation (I.P sample) and (2) thermal preparation (Mel sample)

Appendix 2

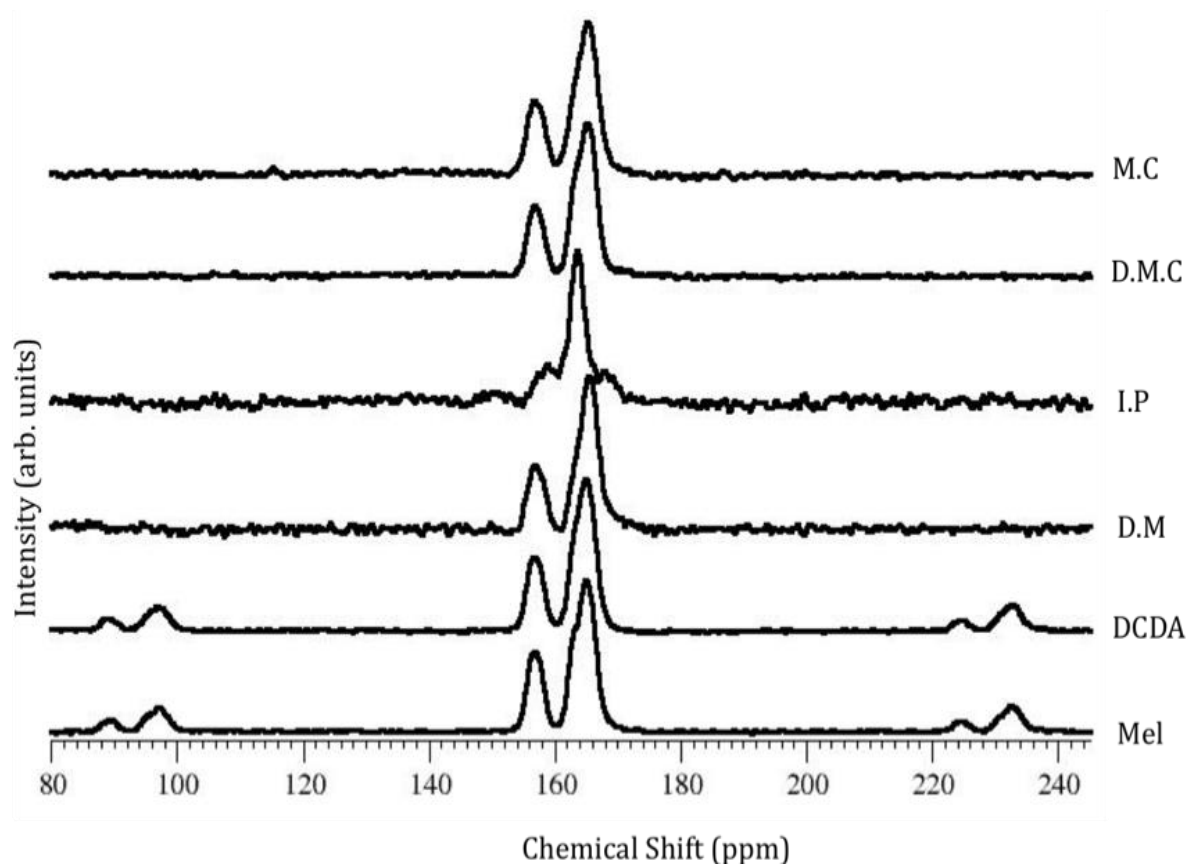# ^{13}C CP-MAS NMR Chemical Shift Spectra for All Samples

Figure A2.1: Experimental ^{13}C CP-MAS NMR Chemical Shift Spectra for all carbon nitride samples; prepared by thermal (M.C, D.M.C, D.M, DCDA and Mel) and ionothermal (I.P) synthesis techniques

Appendix 3

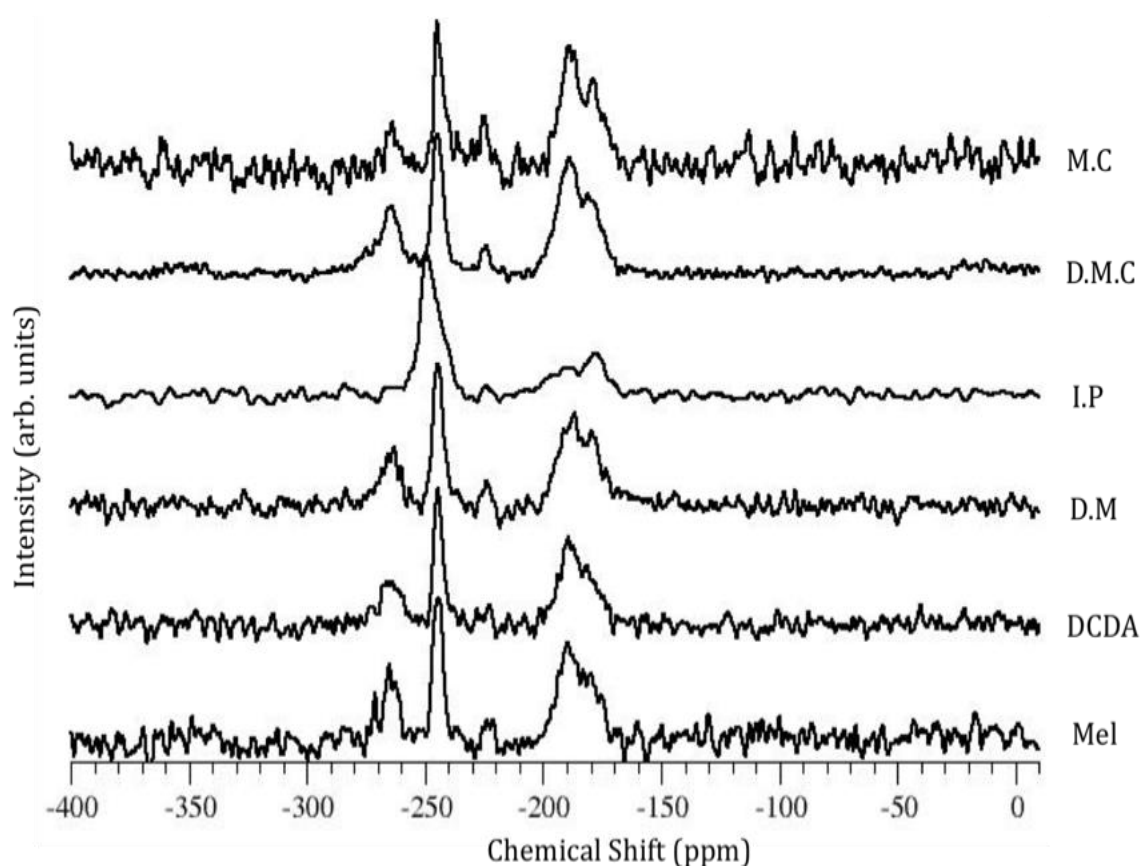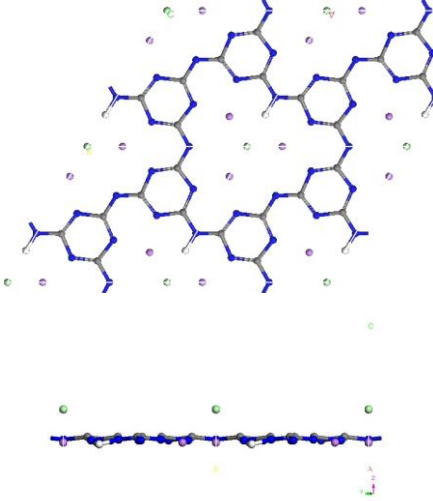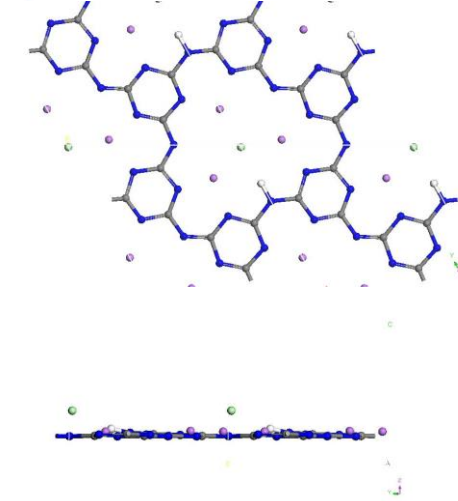# ¹⁵N CP-MAS NMR Chemical Shift Spectra for All Samples
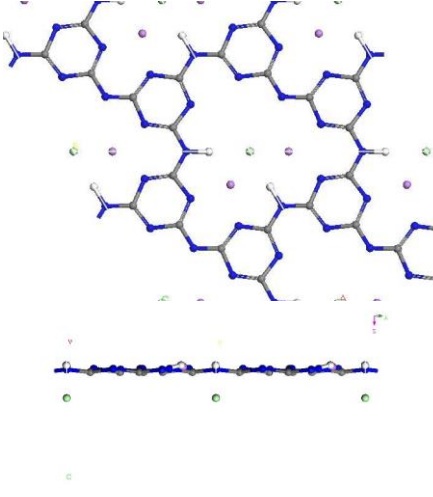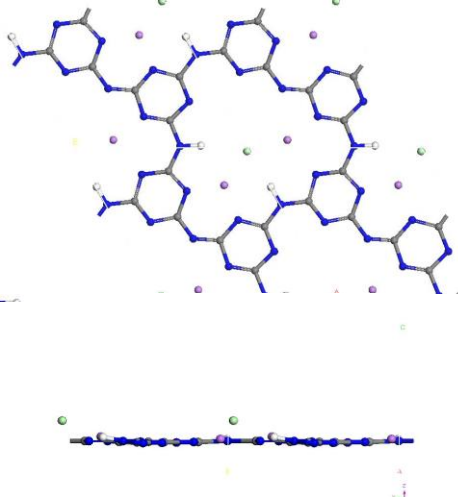
Figure A3.1: Experimental ¹⁵N CP-MAS NMR Chemical Shift Spectra for all carbon nitride samples; prepared by thermal (M.C, D.M.C, D.M, DCDA and Mel) and ionothermal (I.P) synthesis techniques

Appendix 4

AAA and AA'A Stacked Structures with C_6N_9 and $C_{12}N_{18}$ Composition with Varying amounts of H, Li, Cl Ions

Structural Stoichiometry	Initial Structure	Optimised Structure
$C_6N_9HLi_3Cl$		
$C_6N_9H_2Li_2Cl$		

C₆N₉H₃LiCl		
C₆N₉H₄Cl		
C₆N₉Li₄Cl		

$C_6N_9H_3LiCl$

$C_6N_9H_4Cl$

$C_6N_9Li_4Cl$
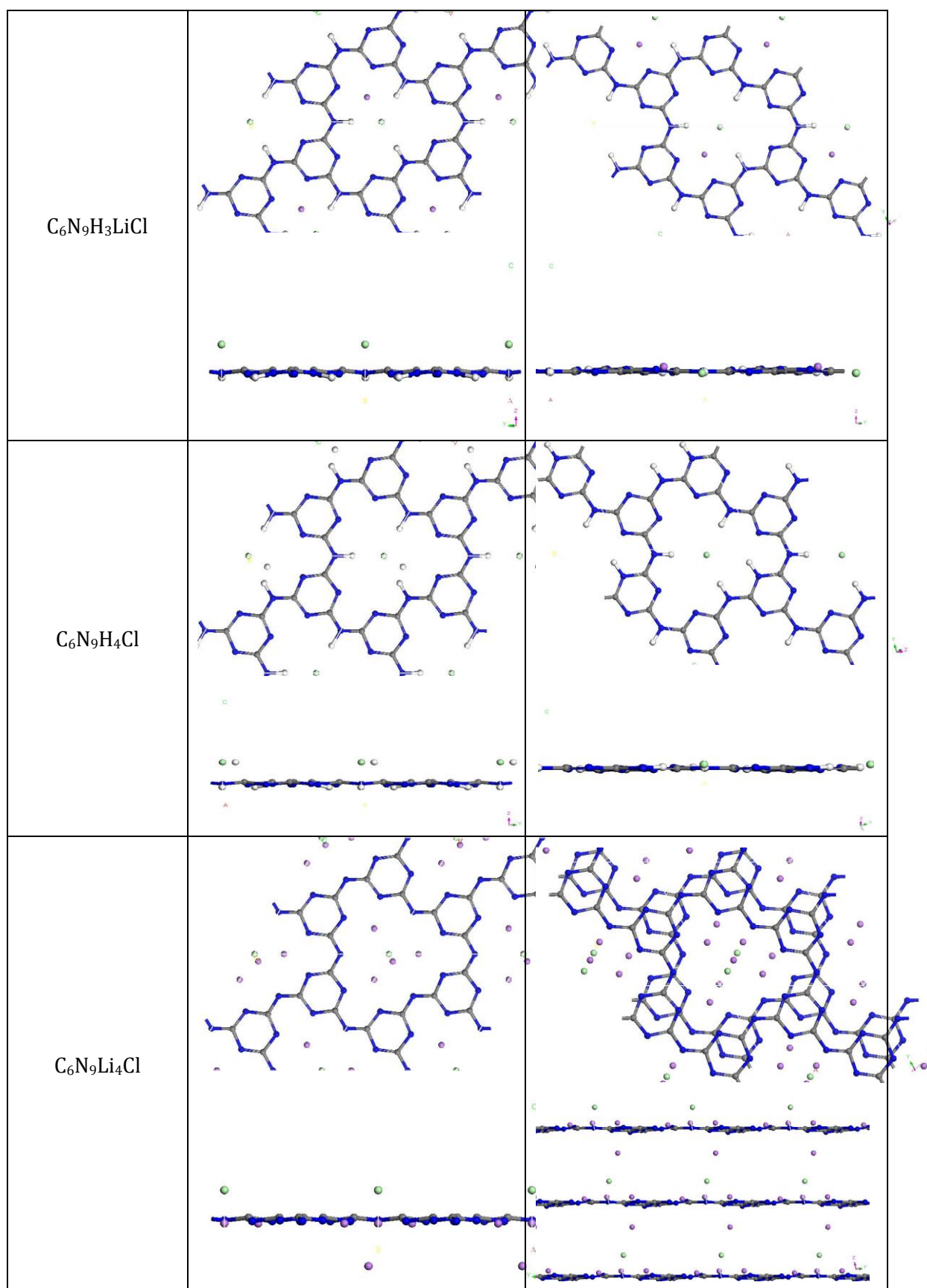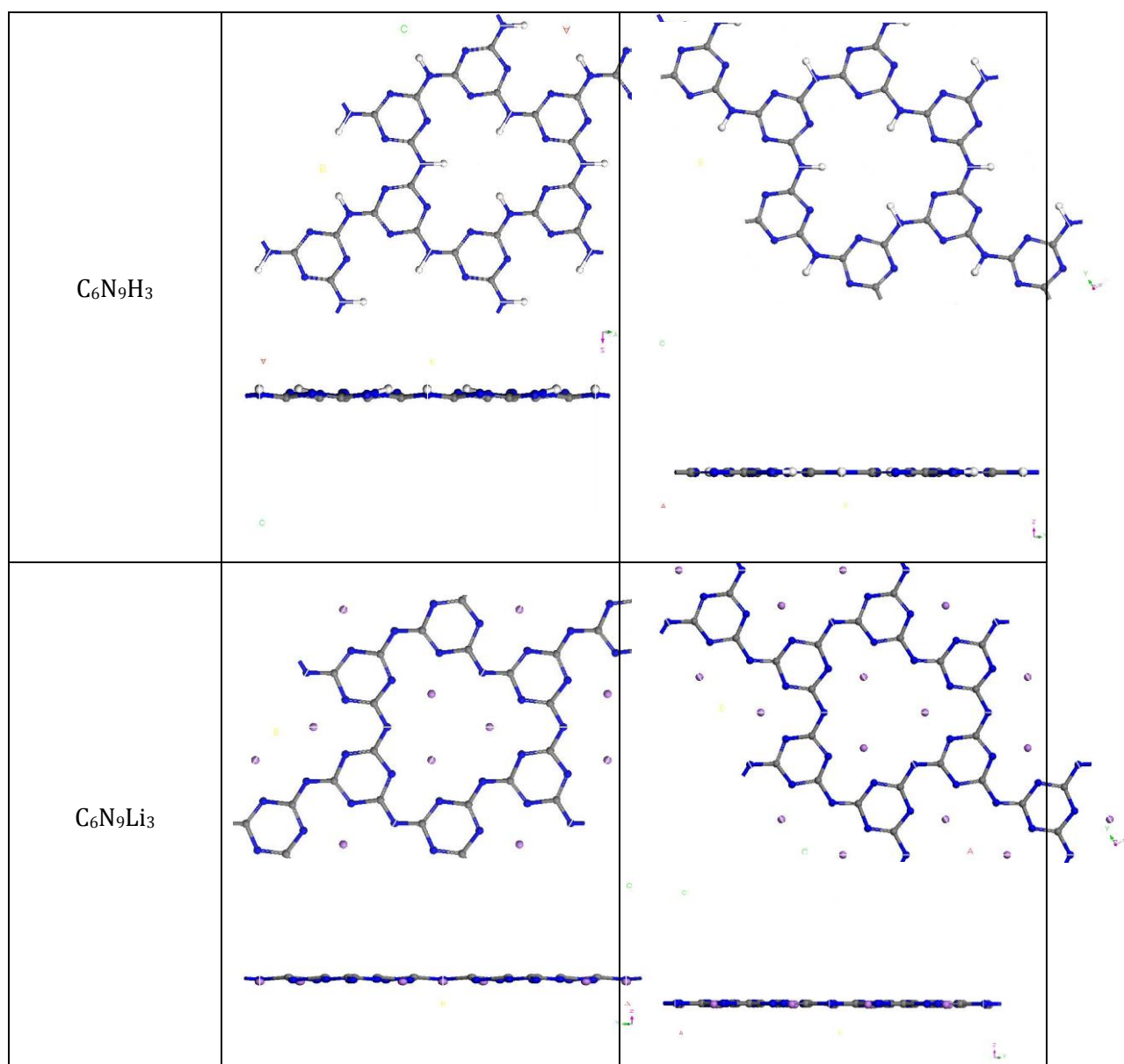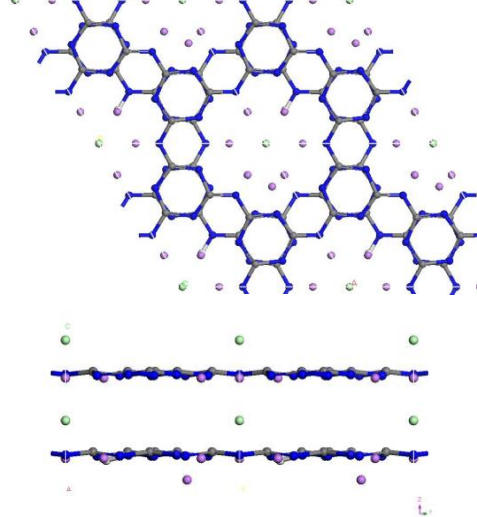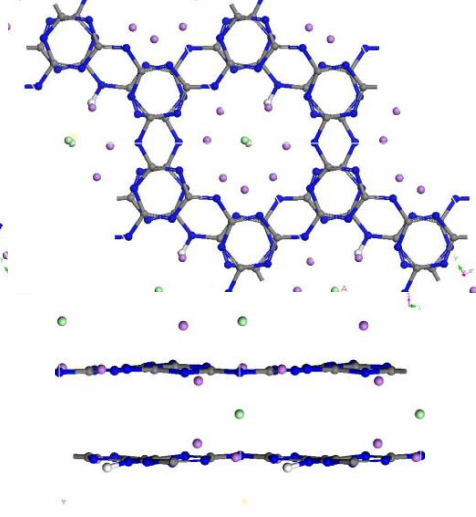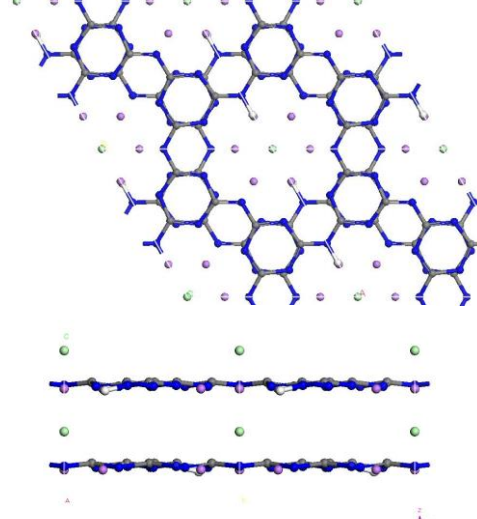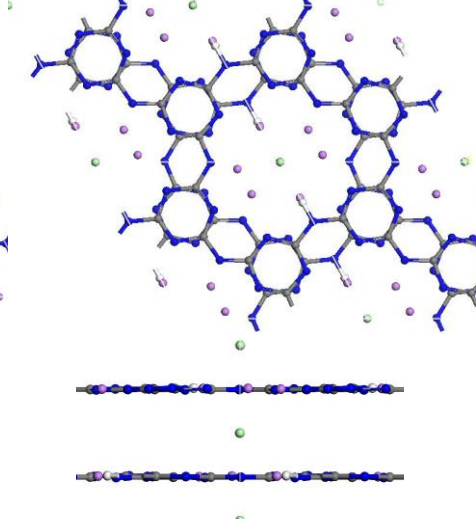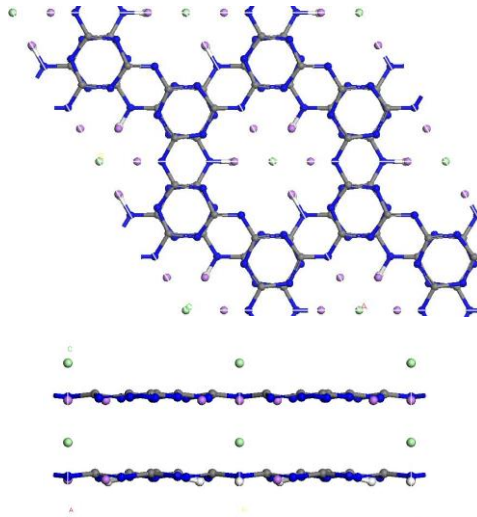
$C_6N_9H_3$		
$C_6N_9Li_3$		

Table A4.1 (pages 216-218): Summary of the optimised $C_6N_9H_aLi_bCl_c$ AAA stacked structures with varying H^+/Li^+ and Cl^- ions, before and after geometry optimization. Colour code: N is blue, C is grey, H is white, Li is purple, Cl is green

Structural Stoichiometry	Initial Structure	Optimised Structure
$C_{12}N_{18}HLi_7Cl_2$		
$C_{12}N_{18}H_2Li_6Cl_2$		
$C_{12}N_{18}H_3Li_5Cl_2$		

$C_{12}N_{18}H_4Li_4Cl_2$		
$C_{12}N_{18}H_5Li_3Cl_2$		
$C_{12}N_{18}H_6Li_2Cl_2$		

$C_{12}N_{18}H_7Li_1Cl_2$		
$C_{12}N_{18}Li_8Cl_2$		
$C_{12}N_{18}H_6$		

$C_{12}N_{18}Li_6$		

Table A4.2 (pages 219-222): Summary of the optimised $C_{12}N_{18}H_aLi_bCl_c$ AA'A stacked structures with varying H^+/Li^+ and Cl^- ions, before and after geometry optimization. Colour code: N is blue, C is grey, H is white, Li is purple, Cl is green

List of References

1.   Liebig, J., Ann Pharm, 1834. **10**: p. 10.
2.   Gmelin, L., Ann. Pharm., 1935. **15**.
3.   Franklin, E.C., J. Am. Chem. Soc., 1922. **44**: p. 486.
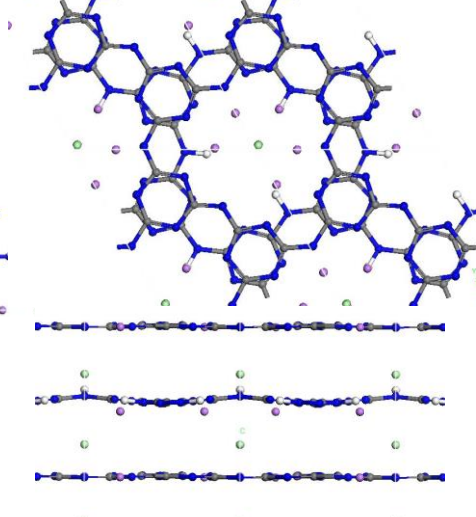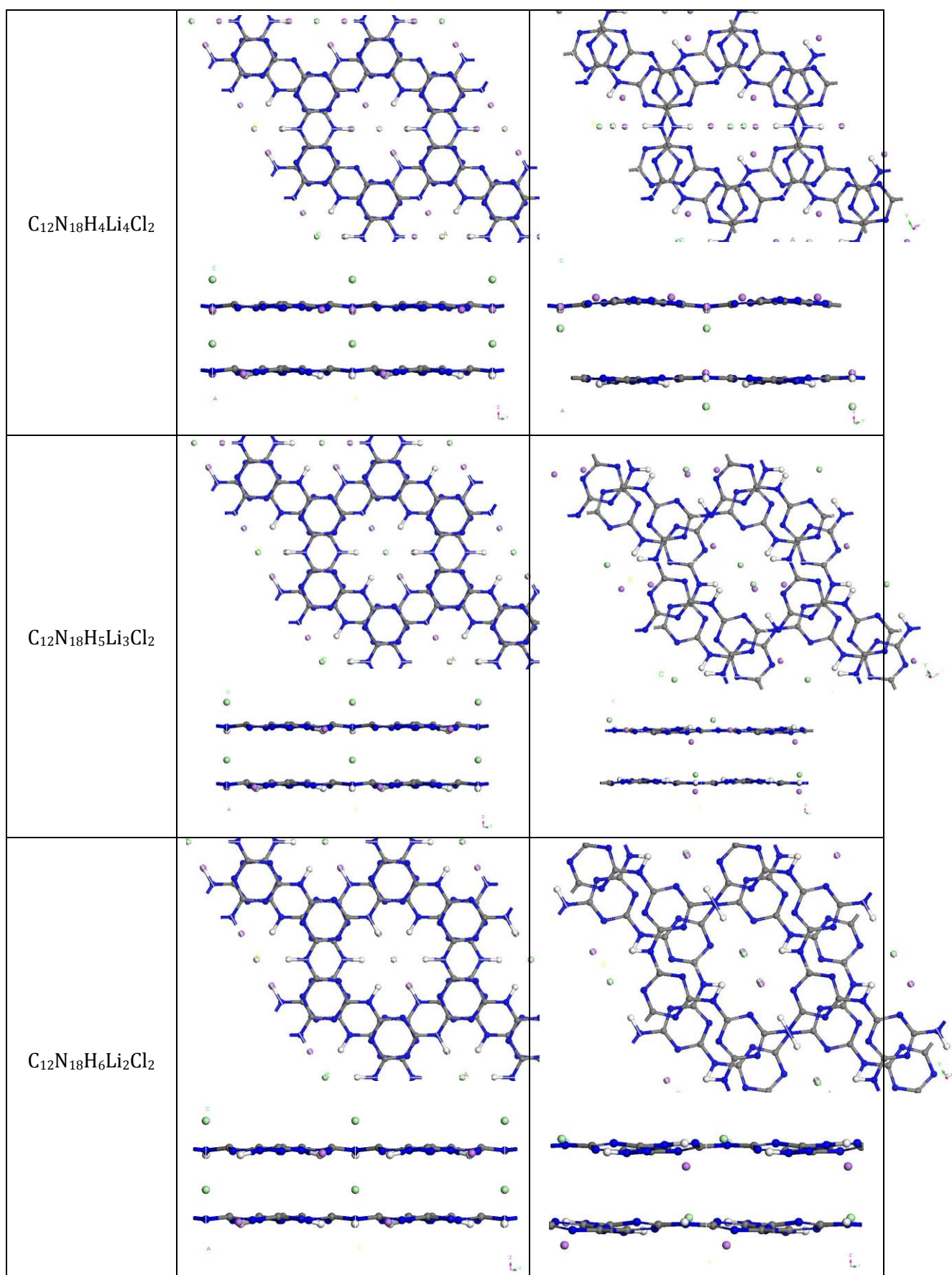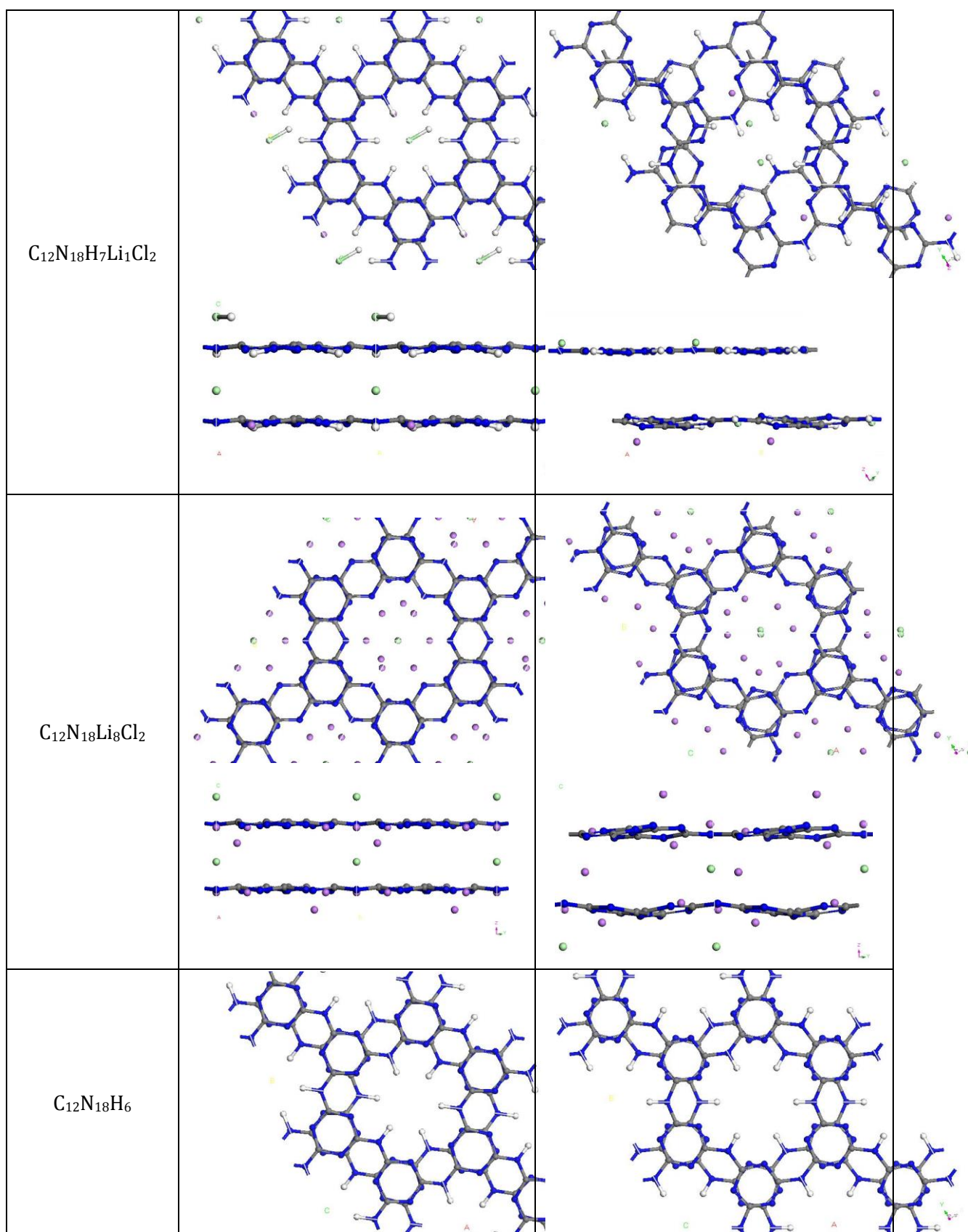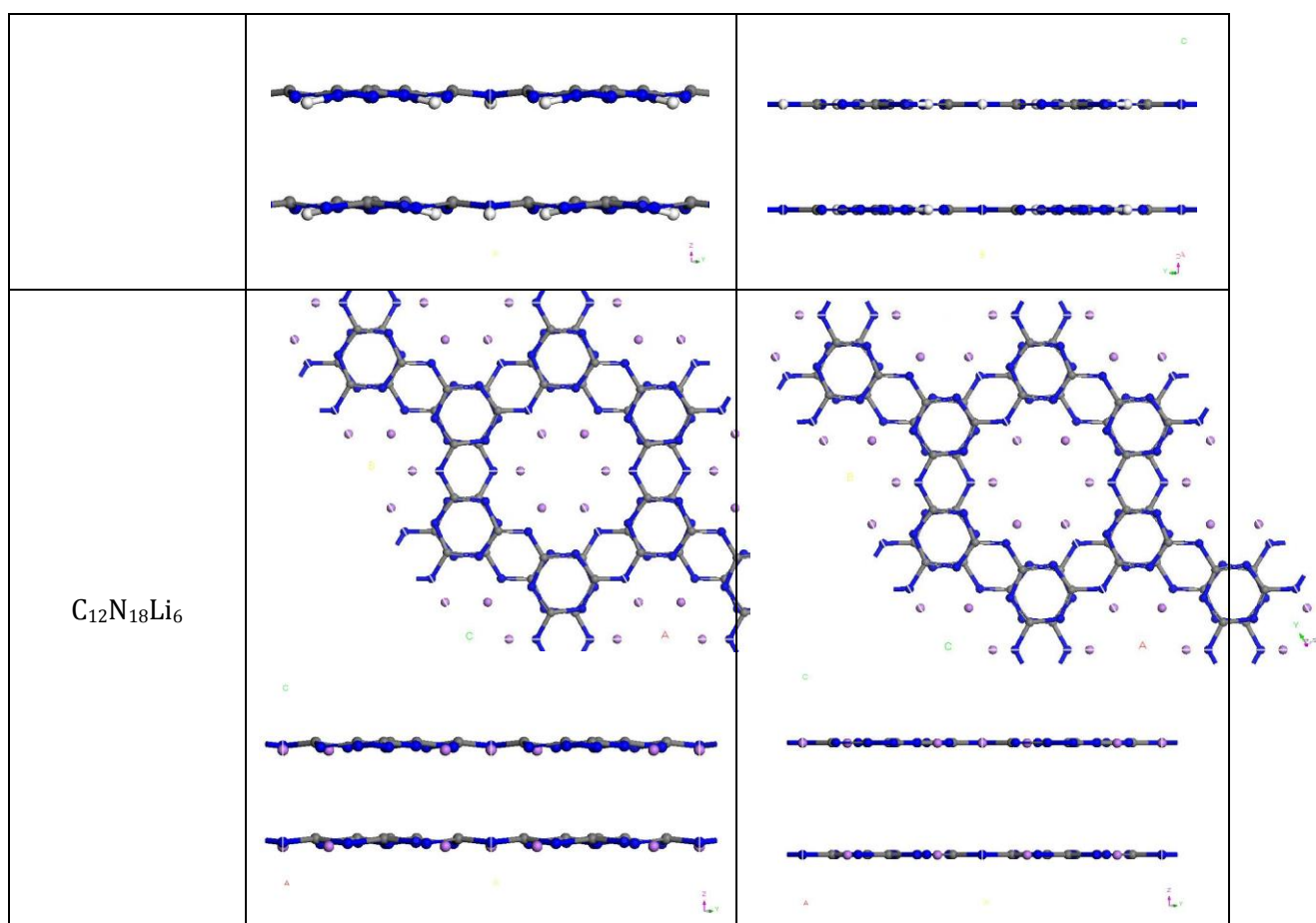4.   Pauling, L. and J.H. Sturdivant, Proc. Natl. Acad. Sci. USA, 1937. **23**(12).
5.   Cohen, M.L., Nature, 1989. **338**: p. 291.
6.   Kuryla, W.C. and A.J. Papa, *Flame Retardancy of Polymeric Materials*. 1973 - 1979, New York: Dekker.
7.   Miller, D.R., D.C. Swenson, and E.G. Gillan, J. Am. Chem. Soc., 2004. **126**(17): p. 5372.
8.   Meyer, R., *Explosives 3rd Ed*. 1987, New York: VCH Publishers.
9.   Guo, Q., Q. Yang, and L. Zhu, Solid State Comminication, 2004. **132**: p. 369.
10.   Zhang, Y., T. Mori, and J. Ye, Sci. Adv. Mater., 2012. **4**: p. 282.
11.   Cho, S., et al., Adv. Mater., 2010. **22**(11): p. 1253.
12.   Thomas, A., et al., J. Mater. Chem., 2008. **18**: p. 4893.
13.   Xiang, Q., J. Yu, and M. Jaroniec, J. Phys. Chem. C, 2011. **115**: p. 7355.
14.   Wang, X., et al., Nature Materials, 2009. **8**: p. 76.
15.   Zhang, Y., et al., Scientific Reports, 2013. **3**.
16.   Cohen, M.L., Physical Review B, 1985. **32**(12): p. 7988.
17.   Liu, A.Y. and M.L. Cohen, Science, 1989. **245**(4920): p. 841.
18.   Teter, D.M. and R.J. Hemley, Science, 1996. **271**(5245): p. 53.
19.   Badding, J. and D. Nesting, Chemistry of Materials, 1996. **8**(2): p. 535.
20.   Lotsch, B.V., et al., J. Chem. Eur., 2007. **13**: p. 4969.
21.   Jurgens, B., E. Irran, and J. Senker, J. Am. Chem. Soc., 2003. **125**: p. 10288.
22.   Lowther, J.E., Phys. Rev. B, 1999. **59**: p. 11683.
23.   Komatsu, T., J. Mater. Chem., 2001. **11**: p. 802.
24.   Kroll, P. and R. Hoffmann, J. Am. Chem. Soc., 1999. **121**: p. 4696.
25.   Wang, X., et al., Nature Materials 'Supplementary Information', 2009. **8**: p. 76.
26.   Kouvetakis, J., et al., Chem. Mater., 1994. **6**: p. 811.
27.   Kroke, E., et al., New. J. Chem., 2002. **26**: p. 508.
28.   Chen, L., et al., Diamond and Related Materials, 1996. **5**: p. 514.
29.   Viehland, J., et al., Solid State Comminication, 1991. **80**: p. 597.
30.   Song, H.W., et al., Journal Physics: Condensed Matter, 1994. **6**: p. 6125.
31.   Sekine, T., et al., Journal of Material Science Letters, 1990. **9**: p. 1376.
32.   Gu, Y., et al., Carbon, 2003. **41**: p. 2653.
33.   Komatsu, T., Physical Chemistry Chemical Physics, 2004. **6**: p. 878.
34.   Liu, J., T. Sekine, and T. Kobayashi, Solid State Comminication, 2006. **137**: p. 21.
35.   Nguyen, J.H. and R. Jeanloz, Materials Science and Engineering A, 1996. **209**: p. 23.
36.   Nesting, D. and J. Badding, Chemistry of Materials, 1996. **8**: p. 1535.
37.   Kroke, E. and M. Schwarz, Coordination Chemistry, 2004. **248**: p. 493.

38. Badding, J.V., Annual Review Materials Science, 1998. **28**: p. 631.
39. Badding, J.V., Advanced Materials, 1997. **9**: p. 877.
40. Matsumoto, S., E. Xie, and F. Izumi, Diamond and Related Materials, 1999. **8**: p. 1175.
41. Horvath-Bordon, E., et al., Angew. Chem. Int. Ed., 2007. **46**: p. 1476.
42. Salamat, A., et al., Physical Review B, 2009. **80**: p. 104106.
43. Demazeau, G., H. Montigaud, and B. Tanguy, Rev. High Press. Sci. Tech., 1998. **7**: p. 1345.
44. Zhang, Z.H., et al., J. Am. Chem. Soc., 2001. **123**: p. 7788.
45. Wolf, G.H., et al., *Frontiers of High Pressure Research II; Application of High Pressure to Low Dimensional Novel Electronic Materials, NATO Adv. Res Workshop.* Kluwer Academic Press Boston, 2001.
46. Deifallah, M.K., PhD Thesis (UCL), 2008.
47. Bojdys, M.J., et al., Chem. Eur. J., 2008. **14**: p. 8177.
48. Wirnhier, E., et al., Chem. Eur. J., 2011. **17**: p. 3213.
49. Lyth, S.M., et al., J. Phys. Chem. C, 2009. **113**: p. 20148.
50. Wang, Y., et al., Angew. Chem. Int. Ed., 2010. **49**: p. 3356.
51. Su, F.Z., et al., J. Am. Chem. Soc., 2010. **132**: p. 16299.
52. Khol, S.W., et al., Science, 2009. **374**: p. 74.
53. Martin, R.M., *Electronic Structure Basic Theory and Practical Methods*. 2010: Cambridge University Press.
54. Born, M. and J.R. Oppenheimer, Ann. Physik, 1927. **84**: p. 457.
55. C. Pisani, R.D., C. Roetti, *Quantum Mechanical Calculations of the Properties of Crystalline Materials*. Vol. 67. 1996: Springer.
56. Jensen, F., *Introduction to Computational Chemistry* 1999, Denmark: John Wiley and Sons.
57. Hohenberg, P. and W. Kohn, Phys. Rev., 1964. **136**: p. B864.
58. Kohn, W. and L.J. Sham, Phys. Rev., 1965. **1133**: p. A140.
59. Leach, A.R., *Molecular Modelling Principles and Applications*. 2001: Pearson Education Limited.
60. Parr, R.G. and W. Yang, *Density Functional Theory of Atoms and Molecules*. 1989, New York: Oxford University Press.
61. Weinert, M., E. Wimmer, and A.J. Freeman, Phys. Rev., 1982. **B26**: p. 4571.
62. Catlow, C.R.A. and A. Cheetham, *New Trends in Materials Chemistry*. Series C: Mathematical and Physical Sciences, ed. N.A. Series. 1995: Kluwer Academic Publishers.
63. Becke, A.D., Phys. Rev. A, 1988. **38**: p. 3098.
64. Lee, C., W. Yang, and R.G. Parr, Phys. Rev., 1988. **B37**: p. 785.
65. Perdew, J.P. and Y. Wang, Phys. Rev., 1986. **B33**: p. 8800.
66. Perdew, J.P. and Y. Wang, Phys. Rev., 1992. **B45**: p. 13244.
67. Perdew, J.P., K. Burke, and M. Ernzerhof, Phys. Rev., 1996. **77**: p. 3865.
68. Perdew, J.P., Phys. Rev., 1986. **B33**: p. 8822.
69. Tschinke, V. and T. Zieglar, Can. J. Chem., 1989. **67**: p. 460.
70. Neumann, R. and N.C. Handy, Chem. Phys. Lett., 1997. **16**: p. 266.
71. Perdew, J.P., et al., Phys. Rev. Lett., 1999. **82**: p. 2544.
72. Dovesi, R. and e. al, *CRYSTAL User's Manual (University of Torino, Torino, Italy, 2006)*. 2006.
73. Clark, S.J., et al., Z. Kristallogr, 2005. **220**: p. 267.

74.   Gill, P.M.W., Advances in Quantum Chemistry, 1994. **25**: p. 141.
75.   Boys, S.F., Proceedings of the Royal Soc. of London. Series A, Math. and Phys.
       Sci., 1950. **200**(1063).
76.   Singh, D.J. and L. Nordstrom, *Planewaves, Pseudopotentials, and the LAPW
       Method 2nd Edition*. 2nd ed. 2006: Springer US. 23.
77.   Kittel, C., *Introduction to Solid State Physics 8th Edition*. 2005: John Wiley &
       Sons.
78.   Catlow, C.R.A., *Modelling the Structure and Reactivity in Zeolites*. 1992,
       London: Academic Press.
79.   Allinger, N.L., J. Am. Chem. Soc., 1977. **99**: p. 8127.
80.   Resnick, R. and R. Eisberg, *Quantum Physics of Atoms, Molecules, Solids,
       Nuclei and Particles* 2nd Edition. 1985: John Wiley & Sons.
81.   Pickard, C.J. and R.J. Needs, J. Phys. Condens. Matter, 2011. **23**: p. 1.
82.   Catlow, R. and S.M. Woodley, Phys. Chem. Chem. Phys., 2010. **12**: p. 8436.
83.   Hofmann, D.W.M., *Data Mining in Crystallography*. Vol. 134. 2010, Berlin:
       Springer-Verlag. 89.
84.   Kirkpatrick, S., C.D.G. Jr, and M.P. Vecchi, Science, 1983. **220**: p. 671.
85.   Czerny, V., J. Optim. Theory Appl., 1985. **45**: p. 41.
86.   Woodley, S.M., Phys. Chem. Chem. Phys., 2007. **9**: p. 1070.
87.   Walsh, A. and S.M. Woodley, Phys. Chem. Chem. Phys., 2010. **12**: p. 8446.
88.   Moellmann, J. and S. Grimme, Phys. Chem. Chem. Phys., 2010. **12**: p. 8500.
89.   Asmadi, A., J. Kendrick, and F.J.J. Leusen, Phys. Chem. Chem. Phys., 2010. **12**:
       p. 8571.
90.   Bloch, F., W.W. Hansen, and M. Packard, Phys. Rev., 1946. **69**: p. 127.
91.   Purcell, E.M., H.C. Torrey, and R.V. Pound, Phys. Rev. , 1946. **69**: p. 37.
92.   Knight, W.D., Phys. Rev., 1949. **76**: p. 1259.
93.   Proctor, W.G. and F.C. Yu, Phys. Rev., 1950. **77**: p. 717.
94.   Dickinson, W.C., Phys. Rev., 1950. **77**: p. 736.
95.   Abraham, R.J., J. Fisher, and P. Loftus, *Introduction to NMR Spectroscopy*.
       1995: John Wiley & Sons Ltd.
96.   Pickard, C.J. and F. Mauri, Phys. Rev. B., 2001. **63**.
97.   Yates, J.R., C.J. Pickard, and F. Mauri, Phys. Rev. B., 2007. **76**.
98.   Bonhomme, C., et al., Chem. Rev. , 2012. **112**: p. 5733.
99.   Birch, F., Phys. Rev. , 1947. **71**.
100.   Kraus, W. and G. Nolze, J. Appl. Crystallogr., 1996. **29**: p. 301.
101.   Reidel, R., *Handbook of Ceramic Hard Materials*. Vol. Vol. 1. 2008, New York:
       Wiley.
102.   Aliev, A.E., D. Courtier-Murias, and S. Zhou, J. Mol. Struct.: THEOCHEM, 2009.
       893: p. 1.
103.   Berger, S., S. Braun, and H.-O. Kalinowski, *NMR Spectroscopy of the Non-
       Metallic Elements*. 1997: Wiley.
104.   Sattler, A., *Investigations into s-Heptazine Based Carbon Nitride Precursors*,
       in *Faculty of Chemistry and Pharmacy*. 2010, Ludwig-Maximilians
       University: Munich.
105.   Accelrys, *Materials Studio 5.3*.
106.   Perdew, J.P., K. Burke, and M. Enzernhof, Phys. Rev. Lett., 1999. **77**: p. 3865.
107.   Vanderbilt, D., Phys. Rev. B, 1990. **41**.
108.   Aliev, A.E., et al., J. Phys. Chem. A, 2011. **115**: p. 12201.

109. Jorge, A.B., et al., J. Phys. Chem. C, 2013. **117**: p. 7178.
110. Lunine, J.I., D.J. Stevenson, and Y.L. Yung, Science, 1983. **222**: p. 1229.
111. Lorenz, R.D., et al., Eos, 2003. **84**: p. 125.
112. Stofan, E.R., et al., Nature, 2007. **445**(1): p. 61.
113. Sagan, C. and B.N. Khare, Nature, 1979. **277**: p. 102.
114. *Adapted from Wikipedia "Tholins"*. 2012; Available from: http://en.wikipedia.org/wiki/Tholin.
115. Coll, P., et al., Planet. Space Sci., 1999. **47**: p. 1433.
116. Imanaka, H., et al., Icarus, 2004. **168**: p. 344.
117. Derenne, S., et al., Icarus, 2012. **221 (2)**: p. 844.
118. Waite, J.H., et al., Science, 2007. **316**: p. 870.
119. Thompson, W.R. and C. Sagan, Origins Life, 1989. **19**: p. 503.
120. Neish, C.D., et al., Icarus, 2009. **201**: p. 412.
121. Pilling, S., et al., J. Phys. Chem. A, 2009. **113**: p. 11161.
122. Quirico, E., et al., Icarus, 2008. **198**: p. 218.
123. Sarker, N., et al., Astrobiology, 2003. **3**(719).
124. McDonald, G.D., et al., Icarus, 1994. **108**(137).
125. McGuigan, M., et al., J. Chrom. A, 2006. **1132**: p. 280.
126. Khare, B.N., et al., Icarus, 1984a. **60**: p. 127.
127. Ehrenfreund, P., et al., Adv. Space Res., 1995. **15**: p. 335.
128. Somogyi, A., et al., J. Am. Chem. Soc. Mass Spec., 2005. **16**: p. 850.
129. Carrasco, N., et al., J. Phys. Chem. A, 2009. **113**: p. 11195.
130. Bernard, J.M., et al., Icarus, 2006. **185**: p. 301.
131. Sagan, C., et al., J. Astrophys., 1993. **414**: p. 399.
132. Szopa, C., et al., Planet. Space Sci., 2006. **54**: p. 394.
133. Stothers, J.B., *Carbon-13 NMR Spectroscopy*. 1972, New York, USA: Academic Press.
134. Cardamone, J.M., et al., Textile Research Journal, 2006. **76**: p. 99.
135. Klapotke, T.M. and J. Stierstorfer, J. Am. Chem. Soc., 2009. **131**: p. 1122.
136. Klapotke, T.M., N.K. Minar, and J. Stierstorfer, Polyhedron, 2009. **28**: p. 13.
137. Martin, G.J., M.L. Martin, and J.-P. Gouesnard, *15N-NMR Spectroscopy*. 1981, Berlin, Germany: Springer-Verlag.
138. Benassi, R., et al., J. Mol. Struct., 2000. **520**: p. 273.